Alma Mater Studiorum · Università di Bologna

Dipartimento di Fisica e Astronomia

DOTTORATO DI RICERCA IN FISICA

CICLO XXXV

Settore Concorsuale: 02/A1 - Fisica Sperimentale delle Interazioni Fondamentali
Settore Scientifico Disciplinare: FIS/01 - Fisica Sperimentale

Study of the tracking performance of a liquid Argon detector based on a novel optical imaging concept

Supervisore:
Prof. Tiziano Rovelli

Presentata da:
Valentina Cicero

Co-supervisori:
Dr. Alessandro Montanari
Dr. Nicolò Tosi

Esame finale anno 2023

Abstract

The Deep Underground Neutrino Experiment (DUNE) is a long-baseline accelerator experiment designed to make a significant contribution to the study of neutrino oscillations with unprecedented sensitivity. The main goal of DUNE is the determination of the neutrino mass ordering and the leptonic CP violation phase, key parameters of the three-neutrino flavor mixing that have yet to be determined. An important component of the DUNE Near Detector complex is the System for on-Axis Neutrino Detection (SAND) apparatus, which will include GRAIN (GRanular Argon for Interactions of Neutrinos), a novel liquid Argon detector aimed at imaging neutrino interactions using only scintillation light. For this purpose, an innovative optical readout system based on Coded Aperture Masks is investigated. This dissertation aims to demonstrate the feasibility of reconstructing particle tracks and the topology of CCQE (Charged Current Quasi Elastic) neutrino events in GRAIN with such a technique. To this end, the development and implementation of a reconstruction algorithm based on Maximum Likelihood Expectation Maximization was carried out to directly obtain a three-dimensional distribution proportional to the energy deposited by charged particles crossing the LAr volume. This study includes the evaluation of the design of several camera configurations and the simulation of a multi-camera optical system in GRAIN.

Sommario

Il Deep Underground Neutrino Experiment (DUNE) è un esperimento con acceleratore a lunga baseline progettato per dare un contributo significativo allo studio delle oscillazioni dei neutrini con una sensibilità senza precedenti. L'obiettivo principale di DUNE è la determinazione dell'ordine di massa dei neutrini e della fase di violazione leptonica di CP, parametri chiave della mixing a tre sapori dei neutrini che non sono ancora stati determinati. Un componente importante del complesso del Near Detector di DUNE è costituito dal System for on-Axis Neutrino Detection (SAND), che includerà GRAIN (GRanular Argon for Interactions of Neutrinos), un nuovo rivelatore ad Argon liquido che ha lo scopo di eseguire imaging delle interazioni dei neutrini utilizzando la luce di scintillazione. A questo scopo, verrà studiato un innovativo sistema di lettura ottica basato su maschere ad Apertura Codificata. Questa tesi si propone di dimostrare la praticabilità della ricostruzione delle tracce di particelle e della topologia degli eventi di neutrini CCQE (Charged Current Quasi Elastic) in GRAIN con tale tecnica, ed è dedicata allo sviluppo e all'implementazione di un algoritmo di ricostruzione basato sulla Maximum Likelihood Expectation-Maximization per ottenere direttamente una mappa tridimensionale proporzionale all'energia depositata dalle particelle cariche che attraversano il volume. Questo studio comprende la valutazione della progettazione di diverse configurazioni di camere e la simulazione dell'implementazione di un sistema ottico multi-camera in GRAIN.

Contents

Introduction

Experimental studies of neutrino oscillations have made it possible to characterize many of the parameters related to neutrino masses through the complementary use of several experimental channels and sources. Some parameters remain to be determined, in particular the unitarity of the neutrino mixing matrix, its possible CP-violating phase, and the neutrino mass ordering, which would have a profound impact on the entire lepton sector of particle physics. The next generation of neutrino oscillation experiments aims to answer these remaining open questions.

The Deep Underground Neutrino Experiment (DUNE) is a long-baseline accelerator experiment designed to contribute significantly to the study of neutrino oscillations with unprecedented sensitivity. It envisages to study neutrinos from a high intensity wide-band neutrino beam with a Near Detector (ND) system at the Fermi National Accelerator Laboratory and a Far Detector (FD) at $\sim$ 1300 km from the beam source at the Sanford Laboratory, in South Dakota in the United States.

For the oscillation parameters to be determined by the data of the multi-kiloton FD Liquid Argon Time Projection Chambers (LArTPCs), the neutrino beam must be characterized before the onset of oscillations at the ND complex, which will be able to provide complementary information on the neutrino beam and to refine the interaction models that will be necessary to analyze the FD data. The ND will also be capable of conducting searches for New Physics, providing high granularity and resolution.

The System for On-Axis Neutrino Detection (SAND) will monitor the neutrino beam flux at the near site. It is based on the 0.6 T superconducting magnet and electromagnetic calorimeter previously used in the KLOE experiment. The inner magnetized volume hosts GRAIN, a 1 ton liquid Argon active target and a low density target/tracker system. SAND will provide a fine-grained reconstruction of neutrino interaction topologies in LAr, and will offer a control sample for neutrino events in the ND LArTPC.

This dissertation is part of an R&D program aiming to develop a novel tracking and calorimetry system entirely based on the imaging of LAr scintillation light. One of the two solutions being developed for such an optical readout system is based on the Coded Aperture Mask technique. The present work aims to demonstrate the feasibility of recon-

structing the topology of neutrino events in GRAIN using such a technique. This study is dedicated to the development and implementation of a reconstruction algorithm based on Maximum Likelihood Expectation Maximization to obtain directly a three-dimensional distribution proportional to the energy deposited by charged particles in the LAr volume. The implemented algorithm was used to evaluate reconstructions of point sources and tracks of minimum ionizing particles with different camera configurations, such as sizes and patterns of the Coded Aperture mask. The best-performing type was selected, and a multi-camera optical system design was proposed to be implemented in the GRAIN geometry. An assessment was then made of the ability of GRAIN to reconstruct tracks of a CCQE neutrino interaction producing a muon and proton. The imaging system in GRAIN and the direction of the muon, known from the SAND tracking system, was used to determine the direction of the proton and to estimate the vertex reconstruction resolution.

The dissertation is organized as follows:

- Chapter 1 presents an overview of the current status of neutrino physics, outlining the theoretical description of massive neutrinos and introducing the phenomenology of neutrino oscillations and the experimental results on the mixing parameters;
- Chapter 2 describes the physics objectives, structure and detectors of the future DUNE experiment;
- Chapter 3 describes the physics objectives and structure of the SAND detector and GRAIN, its active Liquid Argon target;
- Chapter 4 will outline the principles and features of Coded Aperture imaging and subsequently present the rationale and specifics of the GRAIN optical detection system and of its track reconstruction algorithm.
- Chapter 5 shows the optimization of the camera geometry for the reconstruction in GRAIN;
- Chapter 6 presents the analysis of GRAIN's optical system performance with the selected cameras for muon tracks and neutrino event reconstruction.

Chapter 1

Neutrino Physics

1.1 Neutrinos in the Standard Model

The SM of particle physics is a gauge theory that describes strong, electromagnetic, and weak interactions in the universe, as well as elementary particles [1]. It is based on the symmetry group $SU(3)_C \times SU(2)_L \times U(1)_Y$, where SU(3) describes the strong interaction, SU(2) the weak isospin and U(1) the hypercharge group.

In the SM, neutrinos are fermions, basic constituents of matter. In particular, they are neutral massless leptons that only interact with matter via weak interactions. Like other leptons, neutrinos and antineutrinos exist in at least three generations, that is, electron (ν_e), muon (ν_μ), and tau neutrinos (ν_τ), and are associated with the three charged leptons as:

$$\begin{pmatrix} e \\ \nu_e \end{pmatrix} \begin{pmatrix} \mu \\ \nu_\mu \end{pmatrix} \begin{pmatrix} \tau \\ \nu_\tau \end{pmatrix}, \tag{1.1}$$

Under CPT (charge, parity and time reversal) symmetry conservation, a neutrino is a left-handed particle and an antineutrino is a right-handed antiparticleIn the SM, neutrinos can only interact via charged-current (CC) weak interaction with exchange of a $W^{\pm}$ boson and neutral-current (NC) weak interaction with exchange of a Z^0 boson as described by the following interaction lagrangian terms [2]:

$$-\mathcal{L}_{CC} = \frac{g}{\sqrt{2}} \sum_l \bar{\nu}_{Ll} \gamma^\mu l_L^- W_\mu^+ + \text{h.c.} \tag{1.2}$$

$$-\mathcal{L}_{NC} = \frac{g}{2\cos\theta_W} \sum_l \bar{\nu}_{Ll} \gamma^\mu \nu_{Ll} Z_\mu^0, \tag{1.3}$$

where $l = e, \mu, \tau$, g is the coupling constant associated with $SU(2)$, and θ_W is the Weinberg angle. Also, as massless particles, the neutrino flavor is conserved during propagation. However, several experiments have now demonstrated neutrino mixing, indicating that neutrinos do have mass, since flavor mixing and thus oscillations require neutrino mass therms that feature the flavor fields or a combination of them. This is one of the first hints of physics beyond the Standard Model.

As mentioned earlier, neutrinos come in three families. A fourth active neutrino is not allowed by the invisible width of the Z boson to which it would contribute as much as one active neutrino, $Z \to \nu_\alpha \bar{\nu}_\alpha$. The invisible width has been measured with great accuracy at LEP and leads to the following constraint on the number of active light neutrinos [1]:

$$N_\nu = \frac{\Gamma_{inv}}{\Gamma_{\bar{\nu}\nu}} = 2.984 \pm 0.008. \tag{1.4}$$

1.2 Neutrino masses beyond the Standard Model

Although the SM has shown great success in delivering experimental predictions, some phenomena remain unexplained. Among these, experimental evidence for neutrino oscillation demonstrated that neutrinos have mass. The existence of this phenomenon requires a theory beyond the Standard Model (BSM) in order to introduce a corresponding mass term for these particles. In fact, the discovery of neutrino oscillations implies that the differences of the neutrino mass squared are not null and also that the states of flavor neutrino are superpositions of definite mass states. However, measurements of neutrino oscillations do not constrain the overall mass scale, and their determination is a challenging problem, which is still not solved. Furthermore, the reason why neutrinos are many orders of magnitude lighter than other SM particles is not known and the mechanism that gives them mass remains uncertain [3].

1.2.1 Dirac masses

The simplest extension that can be made to the SM involves adding a set of three right-handed neutrino states that couple to matter just through neutrino masses.
Starting from the lagrangian of a free Dirac particle field:

$$\mathcal{L}_D(x) = \bar{\nu}(x)(i\partial\!\!\!/ - m)\nu(x) \tag{1.5}$$

Fermion fields can be written in their chiral components as $\nu_L \equiv P_L\nu$ and $\nu_R \equiv P_R\nu$, such that $\nu = \nu_L + \nu_R$. Thus, the Lagrangian can be rewritten as

$$\mathcal{L}_D = \bar{\nu}_L i\partial\!\!\!/ \nu_L + \bar{\nu}_R i\partial\!\!\!/ \nu_R - m\left(\bar{\nu}_L \nu_R + \bar{\nu}_R \nu_L\right) \tag{1.6}$$

In the SM neutrinos fields have only the left-handed component, unlike other massive fermions fields with have both a left-handed and right-handed component. To introduce the neutrino mass therefore it is necessary to consider also the right-handed component ν_R. In this way, three fields are obtained:

$$L'_{\alpha L} \equiv \begin{pmatrix} \nu'_{\alpha L} \\ l'_{\alpha L} \end{pmatrix}, \quad l'_{\alpha R}, \quad \nu'_{\alpha R}, \quad (\alpha = e, \mu, \tau) \tag{1.7}$$

which enter in the Lepton-Higgs Yukawa Lagrangian, which becomes, after spontaneous symmetry breaking:

$$\mathcal{L}_{H,L} = -\left(\frac{v+H}{\sqrt{2}}\right)\left[\bar{l}'_L Y' l'_R + \bar{\nu}'_L Y'^{\nu} \nu'_R\right] + h.c., \tag{1.8}$$

The Yukawa coupling and the resulting Dirac mass conserve lepton number. In this case, neutrinos and antineutrinos have the same mass and differ by the conserved total lepton number which takes the values $L(\nu) = +1$ and $L(\bar{\nu}) = -1$. The right-handed fields are called *sterile*, since they do not enter into the standard charged and neutral currents; while the left-handed flavor fields are called *active* since they participate in weak interactions.
Since there are no constraints on the Yukawa couplings, the theory cannot predict the values of neutrino masses (and, in general, of all SM particles). However, to account for the experimental upper limits determined for the neutrino masses, the Yukawa couplings must be very small. The neutrino mass limits are at most at the eV-scale[4], this means that the coupling is $\lesssim 10^{-12}$. In this model there is no explanation for the very strong hierarchy of masses between the charged leptons and the neutrinos. Moreover, one would naively expect a similar hierarchy between the neutrino masses and a similar mixing structure to the quark sector, contradicting the observations. For these reasons, other explanations for neutrino masses have also been considered.

1.2.2 Majorana masses

Another possible option is for neutrinos to be Majorana particles. For Majorana neutrinos, the chiral components ν_L and ν_R are not independent and are instead related by the *Majorana condition*:

$$\nu_R = \nu_L^C \equiv \mathcal{C}\bar{\nu}_L^T, \tag{1.9}$$

where $\mathcal{C} \equiv i\gamma^2\gamma^0$ is the charge conjugation operator. Substituting the previous definition in the decomposition of the neutrino field allows us to rewrite the Majorana condition as:

$$\nu = \nu_L + \nu_L^C = \nu^C. \tag{1.10}$$

Majorana particles are thus equal to their antiparticles, so that only neutral fermions like neutrinos can be described by a Majorana field.

The Majorana mass lagrangian for a single neutrino type can be generated using only the left-handed chiral field ν_L as its charge conjugate ν_L^C can be substituted in place of ν_R thanks to the Majorana condition. The Majorana mass term is thus given by:

$$\mathcal{L}_{\text{mass}}^M = -\frac{1}{2} m \bar{\nu}_L^C \nu_L + \text{ h.c. }, \tag{1.11}$$

with the complete Majorana lagrangian consisting of the kinetic terms for ν_L and ν_L^C in addition to the mass term.

The introduction of three generations of massive Majorana neutrinos requires the Majorana mass term to be diagonalized, expressing the left-handed flavor fields ν_L' as linear combinations of massive neutrino fields ν_L :

$$\boldsymbol{\nu}_L' = V_L^\nu \boldsymbol{n}_L \quad \text{with} \quad \boldsymbol{n}_L = \begin{pmatrix} \nu_{1L} \\ \nu_{2L} \\ \nu_{3L} \end{pmatrix} \tag{1.12}$$

so that the three-generation Majorana mass lagrangian can be written as:

$$\mathcal{L}_{\text{mass}}^M = -\frac{1}{2} \bar{\boldsymbol{n}}_L^C M \boldsymbol{n}_L + \text{ h.c. } = \frac{1}{2} \sum_{k=1}^{3} m_k \bar{\nu}_{kL}^C \nu_{kL} + \text{ h.c.} \tag{1.13}$$

with M being the diagonalized mass matrix. It can be seen now that this mass term is not invariant under the global $U(1)$ gauge transformations:

$$\nu_{kL} \to e^{i\varphi} \nu_{kL} \quad (k = 1, 2, 3), \tag{1.14}$$

with the same phase φ for all massive neutrinos: this implies a violation of the total lepton number conservation, leading to beyond the Standard Model phenomena, such as the neutrino-less double-β decay, which represents the best handle to probe the potential Majorana nature of neutrinos.

1.2.3 Experimental mass searches

Beta-Decay experiments

Electron neutrino mass can be measured using the tritium β-decay $^3\mathrm{H} \rightarrow {}^3\mathrm{He} + e^- + \bar{\nu}_e$. The Fermi golden rule gives the transition probability for this decay, and its derivative w.r.t. the kinetic energy T is equal to

$$\frac{d\Gamma}{dT} = \frac{(\cos\theta_C G_F)^2}{2\pi^3}|M|^2 F(E) p E K^2(T), \tag{1.15}$$

where $K(T)$ is the Kurie function and it can be written as:

$$K(T) = \left[(Q-T)\sqrt{(Q-T)^2 - m_{\nu_e}^2}\right]^{1/2}, \tag{1.16}$$

with $Q = M(^3\mathrm{H}) - M(^3\mathrm{He}) - m_e = 18.57$ keV. If neutrinos have zero mass, the graph of K(T) = (Q-T) would depend linearly on T, but if $m_{\nu_e} \neq 0$, a deviation is present, which can be used to measure the value of m_{ν_e}. This deviation can be observed in Fig. 1.1

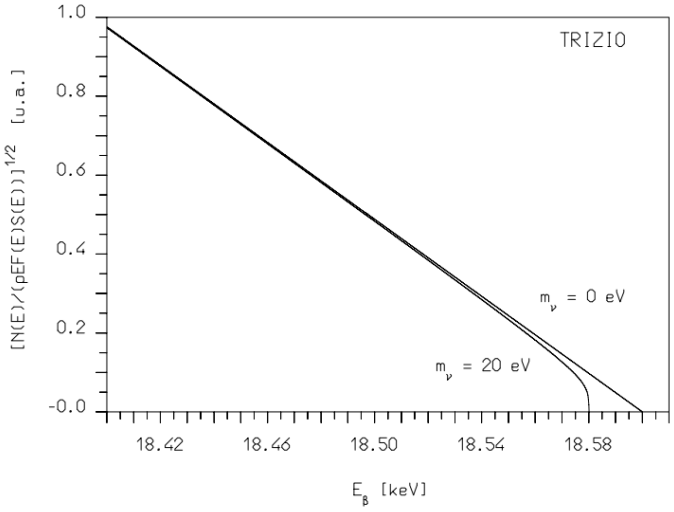

Figure 1.1: Tritium Kurie plot close to the end-point, computed for neutrino masses equal to 0 and 20 eV [5].

However, due to the extraordinary challenge of such a precise measurement, currently, it is only possible to provide an upper limit to the $\bar{\nu}_e$ mass. The strongest constraint

on neutrino mass using this approach has been provided by the KArlsruhe TRItium Neutrino (KATRIN) spectrometer, providing an upper limit to neutrino mass of 1.1 eV at 90% confidence level [4].

Neutrino-less double-beta decay experiments

The hypothesis that neutrinos are Majorana particles, which means that the neutrino and antineutrino are identical, is a key question that concerns the nature of the neutrino mass.
The most promising way to distinguish between Dirac and Majorana neutrinos is the neutrino-less double beta decay. Double beta decay is the process:

$$(Z, A) \rightarrow (Z + 2, A) + 2e^- + 2\bar{\nu}_e \tag{1.17}$$

where (Z,A) is a nucleus with atomic number Z and mass number A, that can occur when single beta decay is kinematically forbidden. Double beta decay is a second-order process in perturbation theory and the measured half-lives are of the order of 10^{24} years. Neutrino-less double beta decay is a similar process, but neutrinos are not present in the final state since they annihilate with each other, as shown in the Feynmann diagrams in Fig. 1.2.

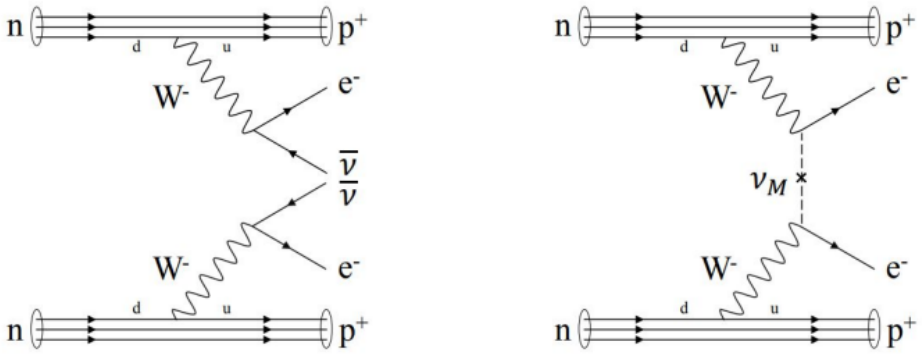

Figure 1.2: Feynman diagrams of the ordinary double beta decay on the left and the neutrino-less double beta decay on the right [6].

In order for this decay to be possible, some requirements have to be satisfied: neutrinos must have mass, neutrinos must be Majorana particles, and the lepton number conservation must be violated. The first requirement is satisfied since it is known from oscillations that neutrinos have mass, while the other two are not proven yet, but they

are necessary to have an interaction between two neutrinos. In fact, the interaction is possible only if one neutrino has a left-handed chiral state and the other has a right-handed chiral state, but both neutrinos have a left-handed helical state. One can see that observations of neutrino-less double beta decay would be a proof that neutrinos are Majorana particles.

The half-life time of the decay ($T^{0\nu}_{1/2}$) is given by:

$$T^{0V}_{1/2} = \left(G|\mathcal{M}|\left\langle m_{\beta\beta}\right\rangle^2\right)^{-1} \simeq 10^{27-28}\left(\frac{0.01\text{eV}}{\left\langle m_{\beta\beta}\right\rangle}\right)^2 y, \tag{1.18}$$

where G is the phase space factor, $\mathcal{M}$ is the nuclear matrix element and $\langle m_{\beta\beta}\rangle$ is the effective Majorana mass.

Experiments aim to measure the characteristic discrete spectrum, as shown in Fig. 1.3. The goal is to estimate the value of the half life of the $0\nu\beta\beta$ decay, which is proportional to $T^{0V}_{1/2} \propto \sqrt{\frac{M_t}{B\Delta E}}$. Therefore, a detector must have a large mass (M_t), a good energy resolution (ΔE), and an extremely low background rate (B). Additionally, not all beta-decay isotopes are good candidates for performing neutrino-less double beta decay searches. For practical purposes, isotopes with forbidden or strongly suppressed beta decay are chosen. Only 36 possible double-beta decay emitters are known. The full list can be found in [7].

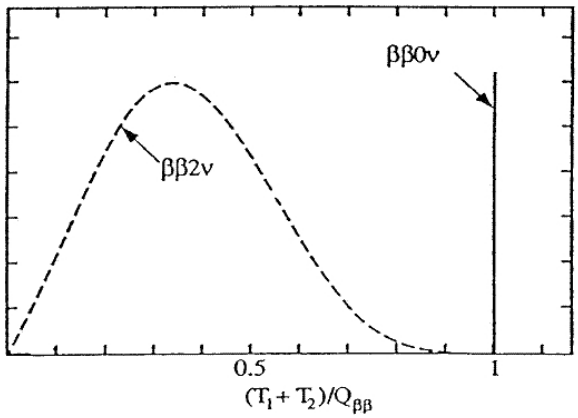

Figure 1.3: Distribution of the sum of the two electron energies for $2\nu\beta\beta$ and $0\nu\beta\beta$.

There are two types of experiment: experiments in which the source is inserted as a thin foil inside a tracking detector and those in which the detector also constitutes the source. NEMO-3 [8] is an example of the first type of experiment, using a source of ^{100}Mo that is known to be a $2\nu\beta\beta$ source. The problem of this kind of experiments is that

the source material is limited and they have a limited energy resolution.
Other experiments, which instead used the second technique, are the CUORE [9] bolometry experiment, HdM [10], GERDA [11].
The strongest constraints up to date are set by KamLAND-Zen collaboration, using Xenon: $T_{1/2,0\nu} > 1.1 \times 10^{26}$ years and $m_{\beta\beta} < (0.06 - 0.16)$ eV [12], the uncertainty on the upper limit for the effective mass is due to nuclear structure effects which cause variations in the nuclear matrix elements.

Cosmological constraints to the neutrino mass

The most stringent limits on the neutrino masses can be obtained from cosmology. The standard model of cosmology predicts the existence of a thermal relic-neutrino background originated in the Big Bang. Furthermore, precision measurements of the Cosmic Microwave Background (CMB) [13] are consistent with the existence of this background. Massive neutrinos are needed in present cosmological models, but since their masses are unknown, they are treated as a free parameter.

The energy density in neutrinos can be estimated as [14]:

$$\Omega_\nu = \frac{\rho_\nu}{\rho_c} = \frac{1}{h^2}\frac{\sum_j m_j}{93\text{eV}} \tag{1.19}$$

where ρ_c is the critical density that makes the universe flat, and $h \simeq 0.65$ is the Hubble constant in units of 100 Km/s/Mpc. The measured flatness of the universe gives a limit $\Omega_{tot}h^3 < 0.4$ that results in:

$$\sum_j m_j < 37\text{eV}. \tag{1.20}$$

A more stringent (but model-dependent) limit can be obtained from studies of large-scale structures. At the time of the formation of the cosmological structure, the neutrinos behaved as hot dark matter, suppressing their growth at small scales. These structures formed from initial seeds, i.e. perturbations in the dark matter density, under the gravitational pull. Cold dark matter falls into gravitational wells which are created by overdensities, making them grow further and leading to the formation of galaxies and clusters. Neutrinos were too fast to be trapped in the wells and free-streamed out of them, suppressing the growth of structures at sufficiently small scales.
These structures are constrained by the CMB measurements performed by Planck mission. A recent analysis by WMAP provides a limit of $\sum_j m_j < 0.11$ eV [15].

In the near future, the next generation of experiments (such as CMB-S4 [16]) will be sensitive to $\sum_j m_j < 2 \times 10^{-2}$ eV, being able to determine whether $\sum_j m_j$ is non-zero at

three-sigma level. This measurement will be a strong confirmation of the neutrino mass measurements performed using neutrino oscillations.

1.3 Neutrino mixing and oscillations

The mixing of neutrino flavors is a natural outcome of considering massive neutrinos, since the neutrino flavor and mass eigenstates are not the same [17]. This phenomenon was first proposed by Pontecorvo in 1957 [18], and is called neutrino oscillations.

Neutrino flavour eigenstates (ν_α, with $\alpha = e, \mu, \tau$) can be expressed as a linear combination of the neutrino mass eigenstates (ν_i, with $i = 1, 2, 3$) :

$$|\nu_\alpha\rangle = \sum_i U^*_{\alpha i} |\nu_i\rangle , \tag{1.21}$$

where U is the Pontecorvo-Maki-Nakagawa-Sakata (PMNS) matrix, and it is expressed as a 3×3 rotation matrix of angles θ_{ij} :

$$U = \begin{pmatrix} 1 & 0 & 0 \\ 0 & c_{23} & s_{23} \\ 0 & -s_{23} & c_{23} \end{pmatrix} \begin{pmatrix} c_{13} & 0 & s_{13}e^{-i\delta_{CP}} \\ 0 & 1 & 0 \\ -s_{13}e^{-i\delta_{CP}} & 0 & c_{13} \end{pmatrix} \begin{pmatrix} c_{12} & s_{12} & 0 \\ -s_{12} & c_{12} & 0 \\ 0 & 0 & 1 \end{pmatrix} \begin{pmatrix} e^{i\eta_1} & 0 & 0 \\ 0 & e^{i\eta_2} & 0 \\ 0 & 0 & 1 \end{pmatrix}, \tag{1.22}$$

with $c_{ij} = \cos\theta_{ij}$ and $s_{ij} = \sin\theta_{ij}$.η_1 and η_2 are the Majorana phases. The case of three Dirac neutrinos would lead to a unitary PMNS matrix. δ_{CP} is a phase factor that is non-zero only if CP-symmetry is violated in neutrino oscillations.

The propagation of the mass eigenstates can be described by plane wave solutions:

$$|\nu_i(x,t)\rangle = e^{-i(E_i t - \vec{p}\cdot\vec{x})} |\nu_i(0,0)\rangle , \tag{1.23}$$

that are approximated at the ultra-relativistic limit to:

$$\nu_i(t)\rangle = e^{-i\frac{m_i^2 L}{2E_i}} |\nu_i(0)\rangle , \tag{1.24}$$

where $L = x = ct$ is the propagation distance and m_i and E_i the mass and energy of the i-th mass eigenstate.

Although neutrinos are generated in the flavor eigenstate (ν_α), during propagation they can be expressed as a linear combination of the mass eigenstates. Therefore, the probability of observing a β-flavor neutrino that was generated in the flavor α is:

$$P\left(\nu_\alpha \to \nu_\beta\right) = \left|\langle \nu_\beta \mid \nu_\alpha(t)\rangle\right|^2 = \sum_{i,j} e^{-i\frac{\Delta m^2_{ij} L}{2E}} U^*_{\beta i} U_{\alpha i} U_{\beta j} U^*_{\alpha j} \tag{1.25}$$

where $\Delta m^2_{ij} = m^2_i - m^2_j$ and the term $\Delta m^2_{ij} L/2E$ determines the sensitivity of the experiment to the different parameters. The oscillation probability for antineutrinos can be obtained by assuming that the neutrino interaction respects CPT. By separating the real and imaginary parts of the mixing matrix, for neutrino (ν_α) and antineutrino ($\bar{\nu_\alpha}$) oscillations, equation 1.25 can be written as:

$$\begin{aligned} P(^{(}\bar{\nu}^{)\prime}_\alpha \to {}^{(}\bar{\nu}^{)\prime}_\beta) =& \delta_{\alpha\beta} - 4\sum_{j>i} \mathrm{Re}\left[U_{\alpha i} U_{\alpha j} U_{\beta i} U_{\beta j} \sin^2\left(\frac{\Delta m^2_{ij} L}{4E}\right)\right] \\ & \pm 2\sum_{j>i} \mathrm{Im}\left[U_{\alpha i} U^*_{\alpha j} U^*_{\beta i} U_{\beta j} \sin\left(2\frac{\Delta m^2_{ij} L}{4E}\right)\right]. \end{aligned} \tag{1.26}$$

From Eq. 1.26 it is clear that if the mixing matrix U is complex, $P\left(\nu_\alpha \to \nu_\beta\right)$ and $P\left(\bar{\nu}_\alpha \to \bar{\nu}_\beta\right)$ would not be identical. As they are CP conjugated processes, measuring a different oscillation probability for neutrinos and antineutrinos would be the evidence of CP violation.

Regarding the difference in the squares of the neutrino masses in Eq. 1.25, Δm^2_{21} is called the "solar mass splitting" whereas Δm^2_{31} is the "atmospheric mass splitting", which is $\Delta m^2_{31} = \Delta m^2_{32} + \Delta m^2_{21}$. Two possible mass orderings (or hierarchies) are possible: *normal ordering* (NO) with $m_1 < m_2 < m_3$, which matches the mass ordering of the charged leptons in the SM, and *inverted ordering* (IO) implying $m_3 < m_1 < m_2$ instead. The two hierarchy scenarios are shown in Fig. 1.4.

Historically, the results of the neutrino oscillation experiments were interpreted by assuming only two neutrino states and no CP violation. This is a valid approximation at the precision level of the measurements due to the large difference between Δm^2_{21} and Δm^2_{31}. Taking this into account, Eq. 1.25 can be simplified to the form:

$$P\left(\nu_\alpha \to \nu_\beta\right) = \delta_{\alpha\beta} - (2\delta_{\alpha\beta} - 1)\sin^2 2\theta \sin^2 \frac{\Delta m^2 L}{4E}. \tag{1.27}$$

Neutrino oscillations are perfect for measuring tiny differences of neutrino masses, since even if Δm^2 is small, the oscillation probability can be amplified by a long baseline L, thus oscillations are observable at macroscopic distances. Note that in the previous equation, the sinus squared masks the sign of Δm^2. This is why neutrino oscillation experiments, in principle, are not sensitive to the sign of Δm and can only provide the absolute value.

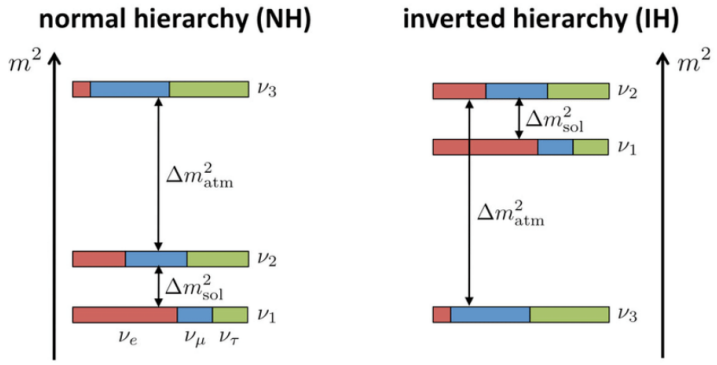

Figure 1.4: A visual representation of the two possible neutrino mass orderings/hierarchies. On the left, the normal ordering, where $m_1 < m_2 < m_3$, and the atmospheric mass-squared splitting is positive. On the right, the inverted ordering, where $m_3 < m_1 < m_2$ and the atmospheric mass-squared splitting is negative. The relative proportion of red (ν_e), blue (ν_μ), and green (ν_τ) in the box corresponding to the mass eigenstates quantifies the relative probability of finding the α flavour eigenstate in the corresponding mass eigenstate. Image by JUNO collaboration.

At large L or, alternatively, at small E, the oscillation probability tends to the constant value of $\left\langle P_{\nu_\alpha \to \nu_\beta} \right\rangle = \frac{1}{2}\sin^2 2\theta$, due to the effect of finite energy resolution, as shown in Fig. 1.5 In fact, the uncertainty relation $1 \sim \Delta E \Delta t \simeq \frac{\Delta m^2}{2E} L$ is valid.

In addition, the plane-wave treatment of neutrino oscillations is just an approximation. Indeed, since a plane wave has a definite momentum p, it would be impossible to know where the neutrino was produced due to the Heisenberg principle, and then the distance L would be unknown. It is then necessary to describe each mass eigenstate using a wave packet, which can have a different mass. During time propagation, the wave packets will separate, and, as a consequence, there will be no more oscillations. In summary, different mass eigenstates produced at the same instant arrive at different times, depending on their individual speeds. For example, supernova neutrinos no longer oscillate when they reach Earth: since separation occurs approximately in 10^3 km, they would arrive with a time difference in the order of 10^{-4} s.

1.3.1 Matter effects in neutrino oscillations

Oscillations come from differences in phase between mass states. Therefore, while in vacuum the free Hamiltonian has to be considered, in a material there are also interaction potentials. When neutrinos travel through dense medium (eg, the Sun or the

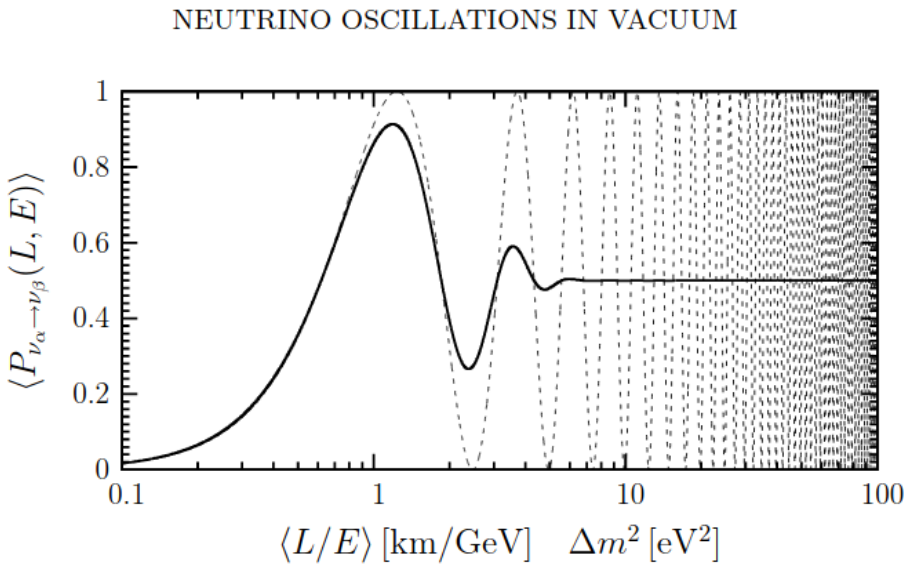

Figure 1.5: Probability of $\nu_\alpha \to \nu_\beta$ transitions for $\sin^2 2\theta = 1$ as a function of $\Delta m^2 \langle L/E \rangle$. The solid line represents the transition probability averaged over a Gaussian L/E distribution with $\sigma_{L/E} = 0.2\langle L/E \rangle$. The dashed line is the unaveraged transition probability [2]

Earth), the coherent forward scattering from the particles they encounter along the way can significantly alter their propagation. As a result, the oscillation probability can be somewhat different than it is in a vacuum. The flavor-changing mechanism in matter was named after Mikhaev, Smirnov, and Wolfenstein (MSW), who first pointed out [19] that there is an interplay between flavor-nonchanging neutrino-matter interactions and neutrino mass and mixing. The MSW effect stems from the fact that electron neutrinos (and antineutrinos) have different interactions with matter compared to other neutrino flavors. In particular, ν_e can have both charged current and neutral current elastic scattering with electrons, while ν_μ and ν_τ have only neutral current interactions with electrons. This fact gives rise to an extra potential $V_W = \pm\sqrt{2}G_F N_e$, where N_e is the electron density in matter, G_F is the Fermi constant, and the positive (negative) sign applies to electron-neutrinos(antineutrinos) scattering.

The oscillation probability becomes:

$$P_{\nu_e \to \nu_e} = 1 - \sin^2 2\theta_M \sin^2\left(\frac{\Delta_M^2 L}{4E}\right), \tag{1.28}$$

with a squared mass difference due to matter effects equal to

$$\Delta m^2_M = \Delta m^2_V \sqrt{\sin^2 2\theta + (\cos 2\theta - \zeta)^2} \tag{1.29}$$

and a relation for the matter effect mixing angle such as

$$\sin^2 2\theta_M = \frac{\sin^2 2\theta}{\sin^2 2\theta + (\cos 2\theta - \zeta)^2} \tag{1.30}$$

where Δm^2_V and θ are the values referred to oscillations in vacuum, while ζ is related to the matter electron density and it is given by

$$\zeta = \frac{2\sqrt{2} G_F N_e E}{\Delta m^2_V}. \tag{1.31}$$

From these formulas, it is possible to understand the following important consequences of the MSW effect:

1. long baselines or high matter densities are required to observe significant matter effects (in the limit $\Delta m^2_M L/(4E) \ll 1$ the vacuum probabilities can be retrieved;

2. under the resonant condition $\cos 2\theta = \zeta$, oscillations can be significantly enhanced, regardless of the value of θ, therefore, even if the vacuum oscillation probability is very small. Since $\zeta = L_V/L_e$, where $L_V = 4\pi E/\Delta m^2$ is the vacuum oscillation length and $L_e = 4\pi/(2\sqrt{2}) G_F N_e)$ is the electron-neutrino interaction length, the resonance condition is:
$$L_V = L_e \cos 2\theta. \tag{1.32}$$

3. oscillation probabilities for neutrino and antineutrinos can be different due to matter effects (because of the sign of ζ, even if neutrino interactions with matter do not violate CP, even if the mixing matrix is real;

4. the resonant condition occurs if $\zeta > 0$, which in turn depends on the sign of Δm^2. This dependence on the sign of Δm^2 can be used to determine the neutrino mass hierarchy. The effect is expected to be seen in long baseline accelerator experiments (see Sect. 1.4.3), and future high-statistics atmospheric neutrino studies (Sect. 1.4.2) and will play an important role in establishing the type of neutrino mass hierarchy.

1.4 Measurement of the neutrino oscillation parameters

Neutrinos come from different sources: the Sun, cosmic ray interactions with the atmosphere, nuclear reactors, and accelerators. Each of these sources produces neutrinos with different parameters L and E, and thus with different accessible Δm^2. Therefore, various experiments were designed to exploit these neutrino sources and probe different neutrino sectors. Two possible modes are available for the measure of neutrino oscillations:

- **Appearance experiments**, which measure transitions between different neutrino flavors, according to Eq. 1.25. As the final flavor can be either absent or present as contamination in the initial beam, the background for this measurement can be very small. Thus, appearance experiments can be sensitive to rather small mixing angles.

- **Disappearance experiments**, which measure the survival probability of a neutrino flavor

$$P_{\nu_\alpha \to \nu_\alpha}(L, E) = 1 - 4 \sum_{k>j} |U_{\alpha k}|^2 \, |U_{\alpha j}|^2 \sin^2 \left(\frac{\Delta m^2_{kj} L}{2E} \right), \tag{1.33}$$

  by comparing its initial and final interaction rates. As the interaction rates have statistical fluctuations, apart from oscillations, small disappearances are difficult to reveal, so that disappearance experiments are not suited for measuring small missing angles.

In both cases, a neutrino source is used. Then, some experiments use a small near-detector to measure the neutrino flux near the source, to ensure the composition of the initial flux, while a large far detector measures the neutrino flux after a distance L. The appearance experiments start with a neutrino flavor ν_α at the source and the far detector looks for a different neutrino flavor ν_β at distance L from the source, measuring the appearance probability $P_{\nu_\alpha \to \nu_\beta}$; while the disappearance experiments look for the same neutrino flavor ν_α at distance L from the source, measuring the disappearance probability $P_{\nu_\alpha \to \nu_\alpha}$

1.4.1 Solar neutrino experiments

Solar neutrino experiments are sensitive to Δm^2_{21} and $\sin^2\theta_{12}$. Solar neutrino experiments observe neutrinos produced by nuclear fusion reactions in the Sun core. According to the

Standard Solar Model (SSM), a multicomponent flux of electron neutrinos is generated by various reactions, ranging from 0.1 to 20 MeV [20]. The flux spectrum of the different reactions is shown in Fig. 1.6.

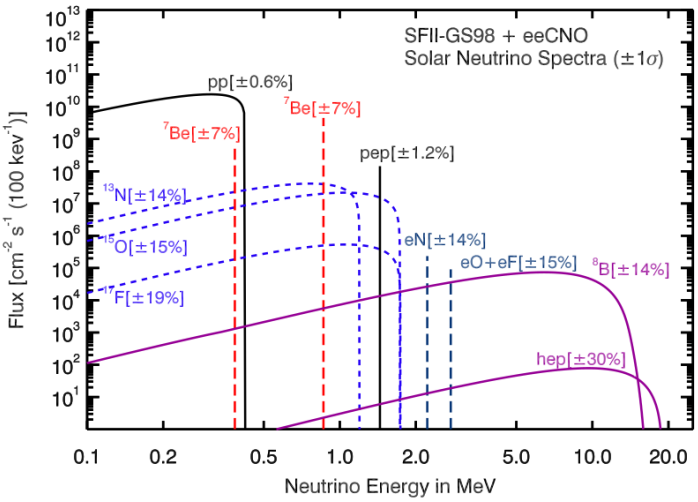

Figure 1.6: Spectrum of solar neutrino fluxes as predicted by SSM.[21]

Different experiments tried to measure the neutrino fluxes for different energies. The first was the Homestake experiment, in which the reaction $\nu_e + {}^{37}\mathrm{Cl} \rightarrow {}^{37}\mathrm{Ar} + e^-$ was used to detect the ν_e flux, with an energy threshold above 800 keV. Therefore, it was sensitive just to ^{8}B and ^{7}Be electron neutrinos. The Homestake experiment, running from 1970 to 1994, observed only one third of the expected flux of solar neutrinos predicted by the SSM model. This was the origin of the so-called *solar neutrino problem.*
The possible explanations were three: an imprecision in the solar model, the experiment was not calibrated properly, or there was some physical phenomenon that occurs to neutrinos as they travel from the Sun to Earth.
In later years, a new generation of experiments using the $\nu_e + {}^{71}\mathrm{Ga} \rightarrow {}^{71}\mathrm{Ge} + e^-$ reaction as the detection technique, lowered the energy threshold to 233 keV, which made them sensitive to the dominant *pp* reaction. GALLEX (and its successor GNO) and SAGE confirmed a deficit of about 1/2 w.r.t. the flux predicted by the SSM [22, 23, 24].

Kamiokande, a 3,000 t water Cherenkov detector placed in the Kamioka mine (Japan), achieved an energy threshold of 6.5MeV, sufficiently low to detect ^{8} B solar neutrinos undergoing elastic scattering ($\nu_x + e^- \rightarrow \nu_x + e^-$). The advantage of this technology is the sensitivity to the three neutrino flavors, and also the directionality of the Cherenkov radiation, which allows for the separation of background events. Again a deficit of $\sim 1/2$ was measured by Kamiokande [25] and its successor Super-Kamiokande [26].

The reason could have been that ν_e oscillates into ν_μ or ν_τ, but the detectors were only sensitive to charge current interactions and then they were not able to observe the other neutrino flavors and they measured only a reduced ν_e flux. Therefore, it was necessary to measure the neutral current interaction rate, which had to be equal to the solar model neutrino flux.

The SNO (Sudbury Neutrino Observatory) [27] was built in 1998 in Canada for that purpose. It was a liquid scintillator, with 1,000 ton of heavy water (D_2O) and 10,000 PMTs. The main reactions that were used are: the charged current interaction $\nu_e + d \rightarrow p + p + e^-$, which is sensitive just to the ν_e flux; the neutral current interaction $\nu_l + d \rightarrow p + n + \nu_l$, which is sensitive to all neutrino flavor fluxes equally; the elastic scattering $\nu_l e^- \rightarrow \nu_l e^-$, which is sensitive to all neutrino flavors, but six times more sensitive to the ν_e flux. The resulting measured fluxes where compatible with the Solar Standar model. Therefore, the solar neutrino puzzle could be explained with neutrino oscillations. The results from SNO measurements are illustrated in Fig. 1.7.

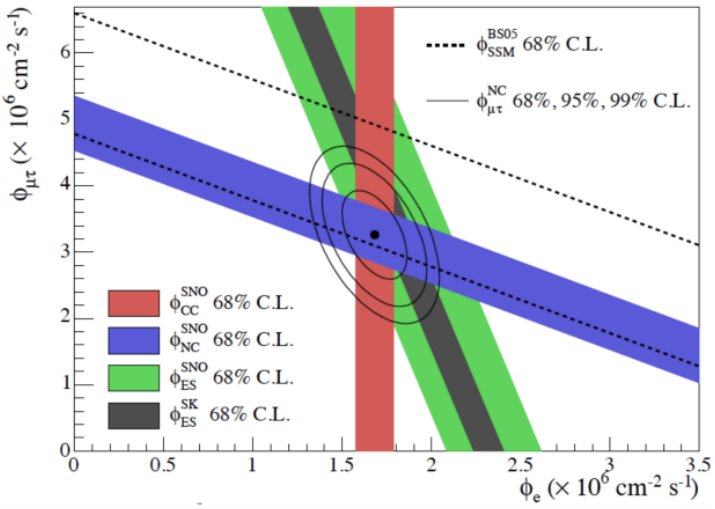

Figure 1.7: Measurement of the SNO experiment of muon and tau neutrino flux from the Sun as a fuction of the electron neutrino flux, showing that the total flux is consistent with solar models. [27]

1.4.2 Atmospheric neutrino experiments

The large underground Cherenkov experiments that came online in the second half of the 1980s, Kamiokande [25] and IMB [28], performed the first observations of atmospheric

neutrinos. Atmospheric neutrinos are produced as a consequence of cosmic rays interacting with the atmosphere: pions are produced, which can decay into a muon and a muon antineutrino. Low-energy muons can then decay again in an electron, an electron neutrino and a muon neutrino. However, experiments measured a deficit of ν_μ interactions with respect to predictions based on the cosmic ray spectrum. The breakthrough for the solution of this so-called atmospheric neutrino anomaly came from the data of Super-Kamiokande (SK), the follow-up experiment to Kamiokande, which revealed an up-down asymmetry in muon neutrino events, a clear effect of atmospheric neutrino oscillations [29]. The SK experiment has provided, so far, high-statistics data on the atmospheric neutrino flux, allowing to model the oscillations as from muon to tau neutrinos and to infer the values of the oscillation parameters with significant accuracy. The SK results have also been corroborated by other atmospheric neutrino experiments, such as Soudan 2 [30] and MACRO [31], as well as Long-baseline accelerator experiments (Sect. 1.4.3) like K2K [32].

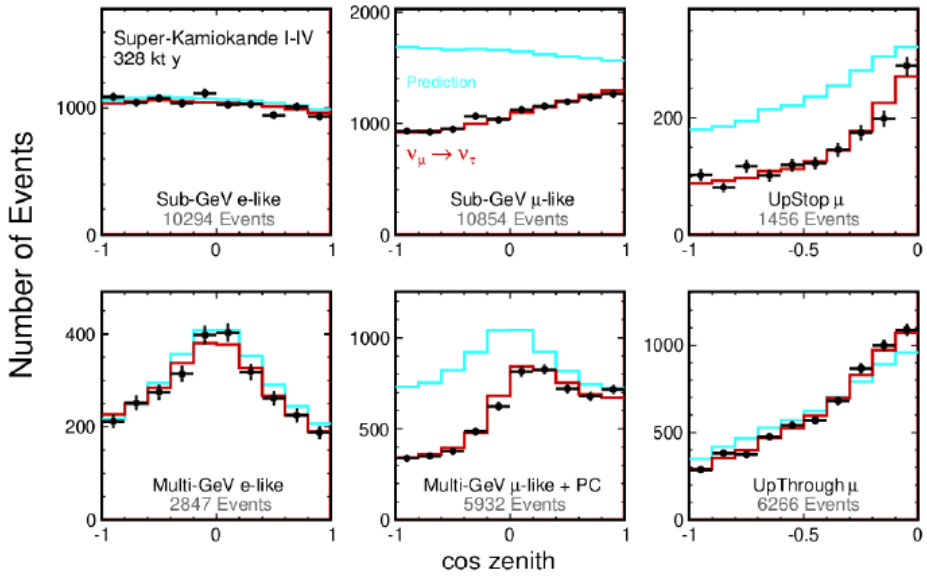

Figure 1.8: Super-Kamiokande results: experimental data, MC predictions with neutrino oscillations and MC predictions in the non oscillation hypothesis are reported as function of the zenith angle. Electron and muon events are shown. Blue histograms represent the MC predictions without neutrino oscillations, red ones show two-neutrino oscillation MC curve.[[1]]

1.4.3 Accelerator neutrino experiments

Experiments with artificial neutrino beams were designed to verify the oscillation parameters of atmospheric neutrinos, using a similar L/E ratio.

Neutrinos can be produced in accelerators by colliding high-energy protons into a target. From the beam-target interactions, hadrons are produced. Among secondary particles, pions and kaons are focused with the so-called magnetic horns into a beam, towards the desired direction before they decay into neutrinos. Other mesons and muons are stopped in the beam dump and soil. Conventional neutrino beams mainly contain muon neutrinos or antineutrinos, since pions are the most abundant products of the proton-target collisions. Moreover, by regulating the magnetic horns, the dominant component of the beam can be chosen to be of neutrinos or antineutrinos. However, beam contaminations are possible. For example, choosing to have a ν_μ beam, most of the neutrinos come from the decay $\pi^+ \rightarrow \mu^+\nu_\mu$. Beam contaminations come from subsequent muon decay $\mu^+ \rightarrow e^+\nu_e\bar{\nu_\mu}$, pion decay $\pi^+ \rightarrow e^+\nu_e$ and kaon decay into $e^+\pi^0\nu_e$.

Accelerator experiments must tune the ratio of the propagation distance and the neutrino energy (L/E) in order to increase the sensitivity to the studied oscillation. In general, there are Long Baseline (LBL) and Short Baseline (SBL) experiments. While LBL experiments use $\sim$ GeV neutrino beams and a baseline of 10^{3-4} m, SBL experiments, with a baseline of $\sim$ 1 km, are able to study neutrino oscillations at the 1 eV scale.

Due to beam contaminations, many Long-Baseline experiments are constituted by two detectors, a near detector and a far detector. The near detector provide high statistics characterization of the neutrino beam close to the source and information about the flux, the energy spectrum, and interaction cross sections in order to reduce the systematic uncertainties due to neutrino flux and ν-nucleus interactions. The far detector studies the flux of neutrinos and their possible flavor oscillation after traveling the experiment baseline.

The first LBL experiment was K2K with a total baseline of 250 km. It used a muon neutrino beam with $\langle E_\nu \rangle \sim 1.3$GeV, produced by the KEK proton synchroton, directed towards the SuperKamiokande detector. The near detector, 300 m far from the source. was 1kt water Cherenkov detector combined with a set of fine-grained detectors. This experiment confirmed the atmospheric neutrino observations that reported muon neutrino disappearance.

MINOS was another accelerator experiment that used a beam from FNAL (Fermi National Accelerator Laboratory), directed towards a far detector in the Soudan mine. The baseline was of 735 km and both the near and the far detectors were iron-scintillator tracking calorimeters with a toroidal magnetic field. This experiment also confirmed the muon neutrino disappearance and it measured atmospheric neutrino oscillation param-

eters [30].

Moreover, the OPERA experiment with the CNGS (CERN to Gran Sasso) beam confirmed the oscillation of ν_μ into ν_τ [33]. It was characterized by a baseline of 732 km with a beam of energy of 17GeV produced at CERN. The T2K experiment is characterized by a high-intensity proton synchroton accelerator, a set of near detectors about 280 m from the neutrino source, the on-axis INGRID far detector (iron-scintillator tracking detector) and the SuperKamiokande detector which performs off-axis neutrino measurements with an angle of 2.5°. This experiment, with a baseline of 295 km makes use of neutrino beam with a peak energy of 0.6GeV. It has been the first experiment to observe $\nu_\mu \rightarrow \nu_e$ oscillations [34]. The NOνA experiment is an off-axis neutrino experiment, with the far detector placed at ∼800 km distance and an off-axis angle of 14.6 mrad, while the near detector is about 1 km from the source. Both are tracking calorimeters detectors. This experiment is committed to the observation of $\nu_\mu\,(\bar{\nu}_\mu)$ disappearance and $\nu_e\,(\bar{\nu}_e)$ appearance [35].

In the near future, two new long-baseline oscillation experiments are expected to operate. DUNE (that will be detailed in chapter 2), and Hyper-Kamiokande [36] as the successor of Super-Kamiokande, a water Cherenkov detector of 260 kt of total mass.

In the SBL experiments, the detector is placed near the neutrino source. LSND used 167t of diluted liquid scintillator to perform $\bar{v}_\mu \rightarrow \bar{v}_e$ appearance searches. They reported an excess of events [37] and later the MiniBooNE experiment reported an excess in the v_e and $\bar{v}_e$ appearance in the same region [38].

In the future, the JSNS [39] at J-PARC and the short-baseline neutrino (SBN) program at Fermilab will investigate the excess reported by LSND and MiniBooNE. The SBN program will consist of three liquid argon time projection chambers at different baselines: SBND at 110 m, MicroBooNE at 470 m and ICARUS at 600 m [40].

1.4.4 Reactor antineutrino experiments

Nuclear reactors are important sources of $\bar{\nu}_e$ produced in beta decays of heavy nuclei. The main neutron-rich nuclei used for the fission chain reactions are ^{235}U, ^{238}U, ^{239}Pu and ^{241}Pu. The electron antineutrino production rate and spectrum can be estimated using information about the thermal power output and fuel composition as a function of time. However, the production of antineutrinos from fission reactions is isotropic; thus, the flux decreases rapidly with distance from the source. The detection of reactor antineutrinos is based on the inverse beta decay process $\bar{\nu}_e + p \rightarrow e^+ + n$. This reaction is characterized by a prompt energy released by the positron annihilating with a surrounding electron producing two photons that can be detected in scintillator detectors. The neutron capture on nucleus after thermalization produces a delayed energy release with

respect to the prompt signal. Hence, the inverse neutron decay process can be detected by looking for the coincidence of these two signals.

The KamLAND experiment[41] takes advantage of 55 reactors located at an average distance of 180 km from the Kamioka mine, in which the KamLAND detector is located. The detector consists of 1kt of high-purity liquid scintillator contained in a 13 m diameter spherical balloon of transparent nylon. The $\bar{\nu}_e$ spectrum is estimated from measurements of beta decay spectra from fission of uranium and plutonium and the average energy $\langle E_{\bar{\nu}_e} \rangle \simeq 3.6\text{MeV}$. Thus, this experiment is optimized to study neutrino oscillations related to the solar mass-squared difference. The first results of KamLAND in 2002 showed the $\bar{\nu}_e$ disappearance at the 99.95% confidence level (CL) and confirmed the value of the mixing angle found by solar neutrino experiments. Moreover, this experiment has a good energy resolution, but it does not see many events; on the other hand, solar neutrino experiments have a large statistical power but a poor energy resolution. Thus, from a joint analysis of the data of KamLAND and solar neutrino experiments [42]it was possible to constrain a small allowed region for the values of the Δm^2_{12} and $\sin^2\theta_{12}$ oscillation parameters, as shown in Figure 1.9.

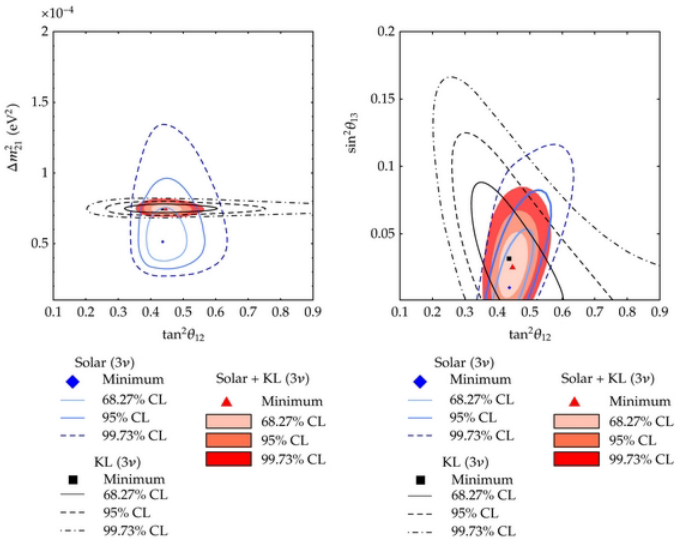

Figure 1.9: Three-flavor neutrino oscillation analysis contour using both solar neutrinos and KamLAND results [42].

Three nuclear reactor experiments have been performed to measure the value of $\sin^2\theta_{13}$ from the disappearance of $\bar{\nu}_e$: Double Chooz [43], Daya Bay [44] and RENO [45]. These three experiments have proved a non-zero value of θ_{13} and a significant contribution

comes from the Daya Bay experiment which has measured a value of $\sin^2 2\theta_{13} = 0.084 \pm 0.005$ [44].

1.4.5 Current knowledge of netrino oscillation parameters

Although most neutrino oscillation experiment results can be explained with the two-flavor paradigm individually, a three-flavor model is needed to explain all results. Table 1.1 shows the current knowledge of the neutrino oscillation parameters obtained from a global analysis of data from different experiments. Since the sign of Δm^2_{32} remains unknown, two orderings are possible: Normal Ordering, ($m_1 < m_2 < m_3$), and Inverted Ordering ($m_3 < m_1 < m_2$). For this reason, two sets of values are given in Tab. 1.1, for both possible orderings.

Normal ordering (NO)		
Parameters	best fit param. $\pm 1\sigma$	3σ range
$\theta_{12}/^\circ$	$33.82^{+0.78}_{-0.76}$	$31.61 \rightarrow 36.27$
$\theta_{23}/^\circ$	$48.3^{+1.2}_{-1.9}$	$40.8 \rightarrow 51.3$
$\theta_{13}/^\circ$	$8.61^{+0.13}_{-0.13}$	$8.22 \rightarrow 8.99$
$\delta_{CP}/^\circ$	222^{+38}_{-28}	$141 \rightarrow 370$
$\Delta m^2_{21}/\left(10^{-5}\text{eV}^2\right)$	$7.39^{+0.21}_{-0.20}$	$6.79 \rightarrow 8.01$
$\Delta m^2_{32}/\left(10^{-3}\text{eV}^2\right)$	$2.449^{+0.032}_{-0.030}$	$2.358 \rightarrow 2.544$
Inverted ordering (IO)		
Parameters	best fit param. $\pm 1\sigma$	3σ range
$\theta_{12}/^\circ$	$33.82^{+0.78}_{-0.76}$	$31.61 \rightarrow 36.27$
$\theta_{23}/^\circ$	$48.6^{+1.1}_{-1.5}$	$41.0 \rightarrow 51.5$
$\theta_{13}/^\circ$	$8.65^{+0.13}_{-0.12}$	$8.26 \rightarrow 9.02$
$\delta_{CP}/^\circ$	285^{+24}_{-26}	$205 \rightarrow 354$
$\Delta m^2_{21}/\left(10^{-5}\text{eV}^2\right)$	$7.39^{+0.21}_{-0.20}$	$6.79 \rightarrow 8.01$
$\Delta m^2_{32}/\left(10^{-3}\text{eV}^2\right)$	$-2.509^{+0.032}_{-0.032}$	$-2.603 \rightarrow -2.416$

Table 1.1: Current knowledge of the 3ν neutrino oscillation parameters. [1]

The best-known parameters are $\theta_{12}, \theta_{13}, \Delta m^2_{21}$ and $|\Delta m^2_{32}|$. As detailed in the previous section, θ_{12} and Δm^2_{21} are well characterized with a precision of 2% and 3% thanks to the study of solar (SNO[27]) and reactor neutrinos (KamLAND[41]). θ_{23} and $|\Delta m^2_{32}|$ are measured in accelerator experiments with a precision of 3% and 1%, by measuring the disappearance of ν_μ and $\bar{\nu}_\mu$ (T2K [34], NOνA[35]), or in atmospheric neutrino experiments (SuperKamiokande [26]). θ_{13} has been measured with a precision of 1.5% in

reactor (DoubleCHOOZ [43], Daya Bay [44]) and accelerator experiments (T2K[44]).

However, in addition to mass ordering, the octant of θ_{23} has not yet been determined (whether it is greater or smaller than 45°), and the CP violation phase has been poorly constrained [46] This will be detailed in Sect. 1.5.

1.5 Open questions

1.5.1 Determination of the θ_{23} octant

The θ_{23} mixing angle can be studied at long baselines via $\nu_\mu \to \nu_e$ and $\bar{\nu}_\mu \to \bar{\nu}_e$ oscillation channels, which are open to both atmospheric and accelerator neutrino experiments. Indeed, ν_μ disappearance and ν_e appearance probabilities can be approximated, being $\Delta m^2_{21}/\Delta m^2_{31} \ll 1/30 \ll 1$, as:

$$\begin{aligned} P(\nu_\mu \to \nu_\mu) &\simeq 1 - \sin^2 2\theta_{23} \sin^2\left(\frac{\Delta m^2_{31} L}{4E}\right) \\ P(\nu_\mu \to \nu_e) &\simeq \sin^2\theta_{23} \sin^2 2\theta_{13} \sin^2\left(\frac{\Delta m^2_{31} L}{4E}\right) \end{aligned} \tag{1.34}$$

where matter- and δ_{CP}-related terms have been neglected. Disappearance experiments are capable of determining both Δm^2_{31} and $\sin^2 2\theta_{23}$ with high accuracy. It is then easy to notice that, for $\theta_{23} \neq \pi/4$, there is a twofold solution of θ_{23} for a certain value of $\sin^2 2\theta_{23}$:

$$\sin^2\theta_{23} = \frac{1}{2}\left[1 \pm \sqrt{1 - \sin^2 2\theta_{23}}\right], \tag{1.35}$$

leading to the so-called octant degeneracy, as the two solutions for θ_{23} are either below 45° (first octant) or above it (second octant).

This degeneracy can be lifted by combining the results of the ν_μ disappearance and ν_e appearance channels, the latter depending on $\sin^2\theta_{23}\sin^2 2\theta_{13}$, with the independent measurements of θ_{13} from reactor experiments, discussed in Section 1.4.4.

Despite all analyses finding some preference for $\theta_{23} > 45°$, values of θ_{23} smaller, larger or equal to $\pi/4$ are still all consistent at the 3σ level. With the current data, the status of the maximality/non-maximality of the θ_{23} mixing angle is thus quite delicate; this might change, however, with the implementation of T2K data in the global fit [47].

1.5.2 Mass Ordering

In all analyses so far the best fit is for the normal mass ordering, with the IO being disfavoured with a $\Delta\chi^2$ ranging from $\sim 2\sigma$, driven by the interplay of LBL accelerator and SBL reactor data, to 3σ when including the atmospheric SK data. Current experiments, though, display too much of a limited individual sensitivity for the discrimination to be finally resolved [1].

In order to resolve the mass ordering, the next generation of experiments will thus focus on three different oscillation configurations [48]:

- Medium baseline ($L \sim 50$ km) reactor $\bar{\nu}_e \rightarrow \bar{\nu}_e$ oscillations, will be studied by the JUNO[49] and RENO-50[50] experiments.

- Long baseline accelerator muon (anti-) neutrino $\overset{(-)}{\nu}_\mu \rightarrow \overset{(-)}{\nu}_e$ oscillations at experiments like the already running NOνA[35] and the future DUNE[51];

- Atmospheric (anti-)neutrino oscillations with the same channel as above, studied by experiments such as PINGU, ORCA, DUNE and Hyper-K [52, 53, 51, 36].

The medium baseline experimental channel relies on the oscillation interference between Δm^2_{31} and Δm^2_{32}, allowed by the nonzero value of θ_{13}. The survival probability of reactor antineutrinos can be written as:

$$\begin{aligned} P_{\bar{\nu}_e \rightarrow \bar{\nu}_e} \simeq\ & 1 - \cos^4\theta_{13}\sin^2 2\theta_{12}\sin^2\left(\frac{\Delta m^2_{21}L}{4E}\right) \\ & - \sin^2 2\theta_{13}\sin^2\left(\frac{\Delta m^2_{31}L}{4E}\right) \\ & - \sin^2\theta_{12}\sin^2 2\theta_{13}\sin^2\left(\frac{\Delta m^2_{21}L}{4E}\right)\cos\left(\frac{2\left|\Delta m^2_{31}\right|L}{4E}\right) \\ & \pm \frac{\sin^2\theta_{12}}{2}\sin^2 2\theta_{13}\sin\left(\frac{2\Delta m^2_{21}L}{4E}\right)\sin\left(\frac{2\left|\Delta m^2_{31}\right|L}{4E}\right) \end{aligned} \tag{1.36}$$

where $\pm$ in the fourth term distinguishes normal and inverted ordering. This probability does not depend on the δ_{CP} phase and the MSW effect is negligible for the baselines in question. Fig. 1.10 illustrates the reactor neutrino energy spectra for both orderings compared to the unoscillated spectrum as a function of the L/E ratio.

The two experiments that are planning to leverage this channel are JUNO [54], in China and RENO-50 [50] in South Korea: their source-detector distance of ~ 50 km maximizes the mass ordering interference term and using large ($\sim$ 20kt) liquid scintillator detectors allows one to reach the required high energy resolution.

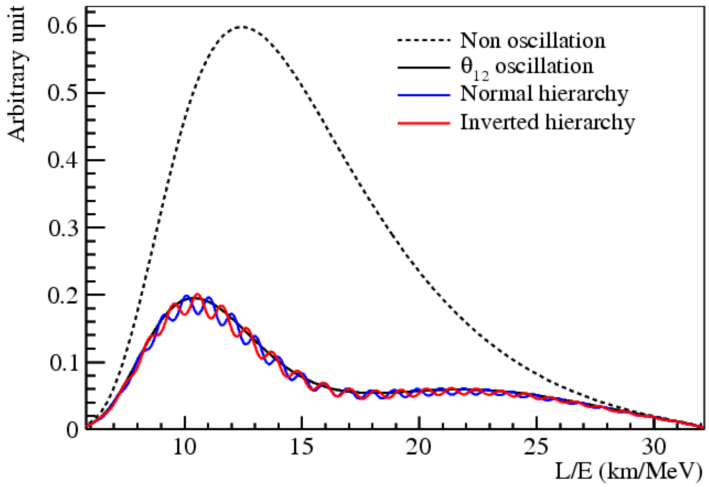

Figure 1.10: Relative shape difference of the reactor $\bar{\nu}_e$ flux for the two mass orderings. The spectra are given as the product of neutrino flux times interaction cross section times survival probability [49].

The second and third types of experiments will take advantage of the matter effect of neutrino propagation in the Earth crust at Long Baselines in the $\overset{(-)}{\nu}_\mu \to \overset{(-)}{\nu}_e$ channels. Assuming a constant matter density, the oscillation probability can be expanded to the second order in the small parameters θ_{13} and $\alpha \equiv \Delta m^2_{21}/\Delta m^2_{31}$ to:

$$\begin{aligned} P_{\nu_\mu \to \nu_e, (\bar{\nu}_\mu \to \bar{\nu}_e)} \simeq\ & 4 \sin^2\theta_{13} \sin^2\theta_{23} \frac{\sin^2\Delta}{(1-A)^2} \\ & + \alpha^2 \sin^2 2\theta_{12} \cos^2\theta_{23} \frac{\sin^2 A\Delta}{A^2} \\ & + 8\alpha J^{\max}_{CP} \cos(\Delta \pm \delta_{CP}) \frac{\sin\Delta A}{A} \frac{\sin\Delta(1-A)}{1-A} \end{aligned} \tag{1.37}$$

with

$$J^{\max}_{CP} = \cos\theta_{12} \sin\theta_{12} \cos\theta_{23} \sin\theta_{23} \cos^2\theta_{13} \sin\theta_{13} \tag{1.38}$$

and

$$\Delta \equiv \frac{\Delta m^2_{31} L}{4E}, \quad A \equiv \frac{2EV}{\Delta m^2_{31}}, \tag{1.39}$$

where V is the effective matter potential in the Earth crust and the $+(-)$ in the

third term is for the neutrino (antineutrino) channel. In this expression α, Δ and A are sensitive to the sign of Δm^2_{32} and therefore to the mass ordering. The probability is also dependent on the CP violating phase of the lepton sector: indeed, as discussed in the following, results on $\overset{(-)}{\nu}_e$-appearance at LBL experiments provides the dominant information on δ_{CP} [18]. Fig. 1.11 illustrates the appearance probabilities for ν_c and $\bar{\nu}_e$ in both mass ordering possibilities and for several values of δ_{CP}.

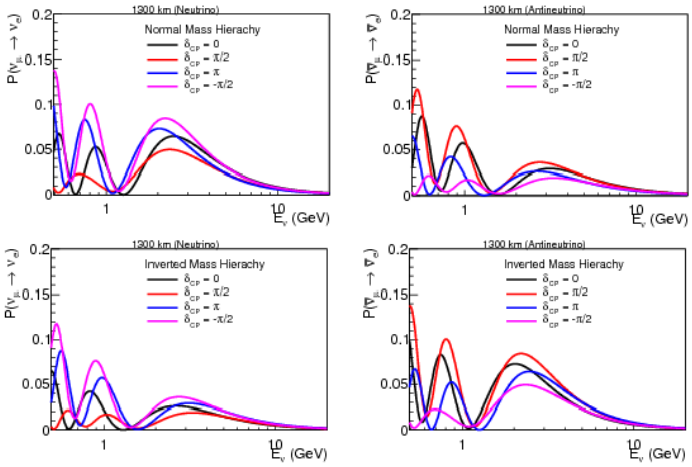

Figure 1.11: Electron neutrino and antineutrino appearance probabilities as a function of the neutrino energy E_ν at the baseline of the future DUNE experiment $L = 1300$ km and for the indicated values of δ_{CP}. Top (bottom) panels correspond to NO (IO) while left (right) panels to ν_e ($\bar{\nu}_e$). In the NO (IO), the ν_e ($\bar{\nu}_e$) appearance is enhanced, while that of $\bar{\nu}_e$ (ν_e) is suppressed[51]

The determination of the mass ordering is thus a crucial factor for measuring the δ_{CP} phase, as it appears in the same expressions for LBL oscillations as the latter: this could lead to degenerate solutions for the ordering and CP phase merge. An independent measurement, e.g. from medium baseline experiments, is thus important [49].

1.5.3 CP Violation

If $U \neq U*$, where U is the PMNS matrix, the CP symmetry is violated. There are 14 general conditions that must be met for the CP violation: charged leptons and neutrinos must not be degenerate in mass (6 conditions), the mixing angles must not be equal to 0 or $\pi/2$ (6 conditions), and the δ_{CP} phase must be different from 0 or π (2 conditions).

However, if the matrix $C = -i|M'^{\nu}M'^{\nu\dagger}, M'^{l}M'^{l\dagger}|$ is defined, it is possible to express the previous 14 conditions with just the condition $\det C \neq 0$, which becomes

$$-2J(m^2_{\nu 2} - m^2_{\nu 1})(m^2_{\nu 3} - m^2_{\nu 1})(m^2_{\nu 3} - m^2_{\nu 1})(m^2_{\mu} - m^2_{e})(m^2_{\tau} - m^2_{e})(m^2_{\tau} - m^2_{\mu}) \neq 0 \quad (1.40)$$

where $J = \mathrm{Im}[U_{e2}U^*_{e3}U^*_{\mu 2}U^*_{\mu 2}]$ is the Jarlskog invariant, useful to measure CP violation independently of parameterization. Using the standard parameterization, it becomes

$$J = \frac{1}{6}\ \mathrm{sin}2\theta_{12}\ \mathrm{sin}2\theta_{23}\ \mathrm{sin}2\theta_{13}\ \mathrm{cos}2\theta_{13}\ \mathrm{sin}\delta_{CP}. \quad (1.41)$$

In contrast to CP violation induced by Majorana phases, which occurs even for two generations of neutrinos, CP violation in neutrino oscillations is a genuine three (or more) flavor effect, so it can be observed only when there is an interference between flavor oscillations involving at least two different phases and three mixing angles. We observe that the accelerator-based long baseline neutrino oscillation experiments will provide the most promising opportunities to observe such CP violation.

The measurement consists in looking for a different behavior between neutrino and antineutrino oscillations, but matter effects introduce an asymmetry, therefore reducing the sensitivity of experiments to δ_{CP}. If $\delta_{CP} = 0$ or π, there would be no CP violation and $P_{\nu_\mu \to \nu_e}$ would be equal to $P_{\bar{\nu_\mu} \to \bar{\nu_e}}$. If $\delta_{CP} = -\pi/2$, $P_{\nu_\mu \to \nu_e}$ would be enhanced, while $P_{\bar{\nu_\mu} \to \bar{\nu_e}}$ would be suppressed. The opposite would happen in the case $\delta_{CP} = +\pi/2$. An example of oscillation probability for various values of δ_{CP} is illustrated in Fig. 1.12.

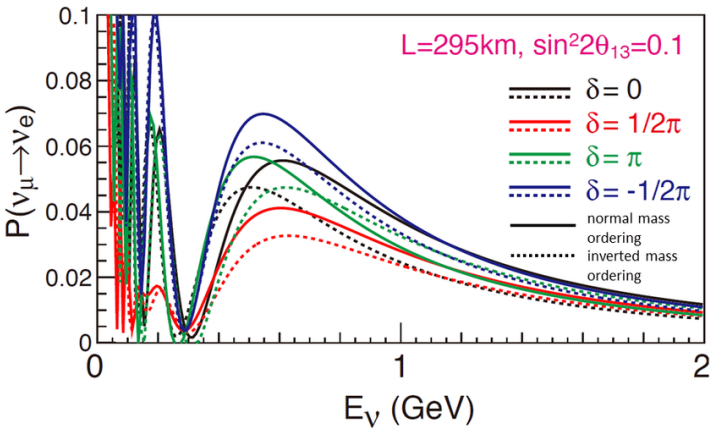

Figure 1.12: $\nu_\mu \to \nu_e$ oscillation probability at T2K as a function of neutrino energy for various values of δ_{CP} and mass ordering. The values of $\mathrm{sin}2\theta_{23}$ and $\mathrm{sin}2\theta_{13}$ are fixed to 0.5 and 0.1 respectively.[55]

T2K and NOνA are the current long-baseline experiments pursuing to measure δ_{CP}, with T2K being the first experiment to constrain the CP violation phase in a range at three-sigma confidence level interval of $[-3.41, -0.03]$ for the normal mass ordering case and $[-2.54, -0.32]$ for the inverse ordering case [46]. In comparison, NOνA constrains the CP-violating phase excluding the region around $\delta_{CP} = \pi/2$ for the inverted mass ordering, in agreement with T2K, and excluding the region around $\delta_{CP} = -\pi/2$ in the normal ordering, in tension with T2K data [56]. This tension is due to the more pronounced asymmetry of ν_e versus $\bar{\nu}_e$ oscillations measured by T2K in comparison with NOνA [56].

The status of the determination of CP violation in the lepton sector is illustrated by the leptonic unitarity triangle in Fig. 1.13: the triangle corresponding to the unitarity conditions for the first and third columns of the PMNS matrix, as in the quark sector. In this plot the absence of CP violation would result in a flat triangle, so that the confidence level of CP violation observation would be given by the confidence level at which the region crosses the horizontal axis.

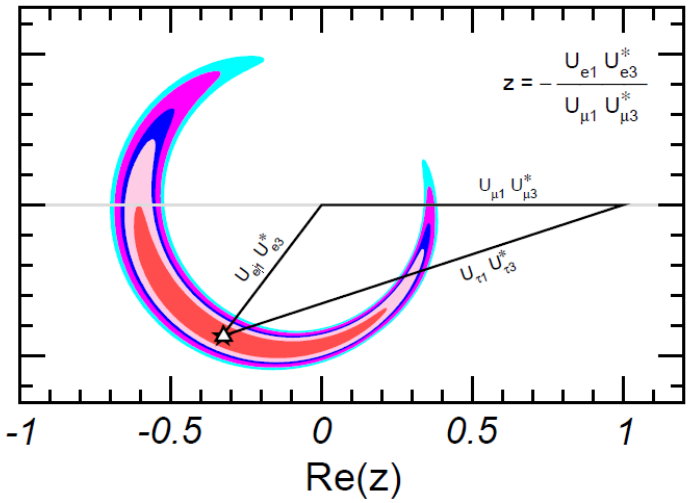

Figure 1.13: Leptonic unitarity triangle for the first and third columns of the PMNS matrix. The triangle is scaled and rotated in order to have two vertices coinciding with $(0, 0)$ and $(1, 0)$. The $1\sigma, 90\%, 2\sigma, 99\%$ and 3σ CL allowed regions of the third vertex are given, assuming NO [1]

Both leading LBL experiments in the search for leptonic CP violation, T2K and NOνA, will operate until 2024-2026. T2K will undergo a beam and near-detector upgrade, with the projected amount of data to be collected by 2026 allowing for a sensitivity

greater than 3σ to the exclusion of $\sin\delta_{CP} = 0$. NOνA should instead be able to reach a 2σ significance to disfavour CP conservation. However, both experiments have only the potential for an indication for the search for CP violation, since they cannot measure δ_{CP} with a 5σ significance.

The next generation of LBL experiment is thus needed to perform the measurement: DUNE and HyperKamiokande have among their primary goals the measurement of δ_{CP}. In this case, since the matter effect reduces δ_{CP} sensitivity, HyperKamiokande, with a shorter baseline, would be in principle more sensitive to δ_{CP}. However, due to the broad energy range of the beam that will cover two oscillation maxima, DUNE will be still competitive in the measurement of the CP-violation phase (see Sec. 2.2).

Chapter 2

The DUNE experiment

The Deep Underground Neutrino Experiment (DUNE) will be a precision long-baseline neutrino oscillation experiment and will be installed in the Long Baseline Neutrino Facility (LBNF) under construction in the United States. It will consist of a Near Detector (ND) at a distance of 547 m from the neutrino source at Fermilab in Illinos and a Far Detector (FD) located at the Sanford Underground Research Facility (SURF) in South Dakota. A qualitative schematic of the experiment is shown in Fig. 2.1.

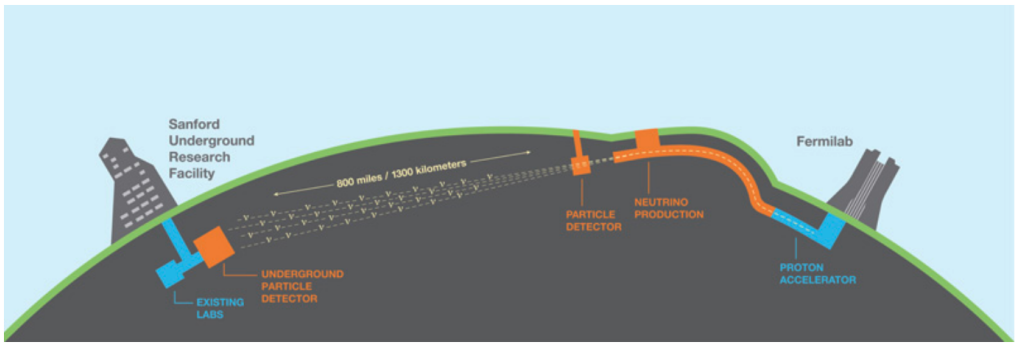

Figure 2.1: Schematic of the LBNF/DUNE facilities at Fermilab and SURF. The existing facilities are shown in blue, while the planned ones are in orange. The neutrino beam baseline of 1300 km is shown [51].

An overview of the experiment, including its motivation, will be presented in section 2.1 while the sensitivities of the experiment and its potential discoveries are described in Section 2.2. The features and design choices of the components of the experiment will be presented in 2.3. The SAND detector and GRAIN subdetector, subjects of this thesis, will be detailed in Chapter 3.

2.1 DUNE design overview and motivation

The still open questions in neutrino physics discussed in Section 1.5, namely the resolution of the mass hierarchy, the determination of the CP-violating phase δ_{CP}, the measurement of the octant of θ_{23}, and precision calculations of all the mixing angles, motivate the need for next generation experiments. The DUNE experiment will make a decisive contribution in each of these areas. It will also look for nucleon decay with the ability to set world-leading limits on proton lifetime, and make detailed, unique measurements of the v_e flux from a core collapse supernova within our galaxy should one occur during the experiment. Along with this, DUNE will be used to look for Beyond Standard Model physics (such as non-standard interactions and sterile neutrinos), signatures of dark matter, and, utilizing the near detector, measurements of a range of neutrino cross sections and nuclear effects including final-state interactions [51].

The technology chosen for the DUNE Far Detector, in order to maximize sensitivity to all of these factors, is the Liquid Argon Time Projection Chamber (LArTPC). The detector will consist of four independent modules, each with a fiducial mass of 10kt LAr and separate data acquisition and readout systems. LArTPC technology combines tracking and calorimetry, allowing identification of ν_μ interactions, as well as good resolution to both lepton and hadronic energies and scalability to the required detector mass. The imaging capability of the LArTPC FD also plays an important role in DUNE BSM searches, and the argon target provides unique sensitivity to electron neutrinos (as opposed to antineutrinos) from supernova bursts.

The neutrino beam will be provided by Fermilab as part of its PIP-II program [57]; it will be wideband, enabling the study of a range of neutrino energies. This facilitates a study of multiple oscillation peaks, and is relevant when considering the effects of an unknown CP-violating phase and unresolved mass hierarchy.

Since the impact of both of these unknown elements manifests itself as an asymmetry between neutrinos and antineutrinos (Eq. 1.37), there is an implicit degeneracy that must be resolved for both phenomena to be correctly determined. In the few-GeV range, the $\nu/\bar{\nu}$ asymmetry due to the matter effect increases with the baseline, so that an experiment with a longer baseline is more sensitive to mass ordering. Thus, the 1300 km baseline is one of the main strengths of DUNE as it provides high sensitivity to matter effects. The asymmetry between neutrinos and antineutrinos oscillation probabilities is approximately $\pm 40\%$ in the region of maximum flux (Fig. 2.2), larger than the maximum asymmetry associated with δ_{CP}.

The role of the Near Detector is to measure the neutrino beam before the onset of the oscillation effect and minimize the systematic uncertainties in long-baseline oscillation measurements. The observed neutrino energy spectrum depends on a complicated

product of flux, cross sections, and detector response, all of which have large a priori uncertainties. Because the FD is a LArTPC, the only way to be sensitive to all three of these classes of uncertainty simultaneously is with a LArTPC at the near site, with kinematic acceptance at least as good as the FD. ND-LAr (Sect. 2.3.3) is optimized to meet this requirement and is critical for all stages of the experiment. A downstream muon spectrometer (the The Muon Spectrometer, TMS, in Phase I) measures the momentum and charge sign of exiting muons.

Because neutrino cross sections depend on energy, it is important to take ND data in different neutrino fluxes. This is enabled by the PRISM technique, in which ND-LAr and TMS move laterally from the primary proton beam direction. Moving off-axis, the neutrino energy spectrum shifts downward. Data collected with different spectra can be combined to produce a data-driven prediction of the oscillated FD spectrum, which is largely independent of interaction and detector modeling.

The SAND detector remains on the axis and has a broad and complementary cross section and an exotic physics program in addition to monitoring the neutrino beam.

In phase II, the TMS will be replaced with ND-Gar, a magnetized high-pressure gaseous argon TPC with a surrounding calorimeter. Its gaseous active target volume gives extremely low thresholds, minimal secondary interactions, and particle-by-particle charge and momentum reconstruction, which extend the reach of the ND.

After a prototyping phase, excavation of the main cavern that houses the Far Detector is now underway. The installation of the first module is expected to start in 2024, followed by a staged deployment of other the modules and an upgrade of the beam intensity. Although the deployment calendar is still preliminary, the sensitivity studies presented in this section assume that the data-taking starts in Phase I with two far detector modules and a beam of 1.2 MW. The third and fourth modules are added after one and three years of operation, respectively. Finally, the beam is upgraded to 2.4MW after six years of data-taking (Phase II). Table 2.1 summarizes DUNE elements in Phases I and II [58].

Parameter	Phase I	Phase II
FD mass	20kt fiducial	40kt fiducial
Beam power	up to 1.2MW	2.4MW
ND config	ND-LAr,TMS, SAND	ND-LAr, ND-GAr, SAND

Table 2.1: A description of the two-phase approach to DUNE [58].

2.2 Expected sensitivity and discovery potential

The staged approach to the DUNE experiment will allow for early preliminary results, but will require more time for the construction and commissioning of facilities from later phases. For this and other reasons, the accumulated data are often referred to as an 'exposure', a function of detector size, beam power and time with units $kt \cdot MW \cdot year$. Current assumptions on exposures of ∼14 years of operation are shown in Table 2.2. This staging will be assumed for all sensitivities presented in this section.

Experiment stage	Exposure (kt-MW-years)	years
Phase I	16	1-2
	66	3-5
	100	4-6
Phase II	334	7-8
	400	8-9
	646	11
	936	14

Table 2.2: Expected Exposure in kt-MW-years per years of operation.

The appearance probability expected at the DUNE far detector is shown in Figure 2.2 for various values of δ_{CP}. It can be seen why a broad-band beam with the ability to operate in neutrino and antineutrino mode is critical; the value of δ_{CP} affects both the frequency and the amplitude of the oscillations, with differing effects at the different oscillation nodes and between neutrinos and antineutrinos.

2.2.1 Sensitivity to neutrino oscillations

The oscillation channels that DUNE will observe are $\overset{(-)}{\nu}_\mu \rightarrow \overset{(-)}{\nu}_e$, whose probability $P_{\overset{(-)}{\nu}_\mu \rightarrow \overset{(-)}{\nu}_e}$, through matter in a constant density approximation, is given by Eq. 1.37: both δ_{CP} phase and the effective matter potential introduce an asymmetry between the $\nu_\mu \rightarrow \nu_e$ and $\bar{\nu}_\mu \rightarrow \bar{\nu}_e$ channels [51].

Measurements of the mass hierarchy and the degree of CP violation are determined by simultaneously fitting the $v_\mu \rightarrow v_\mu, \bar{v}_\mu \rightarrow \bar{v}_\mu, v_\mu \rightarrow v_e$ and $\bar{v}_\mu \rightarrow \bar{v}_e$ oscillated spectra, assuming a 50% neutrino, 50% antineutrino exposure.

CP violation sensitivity Figure 2.3 shows the sensitivity of DUNE to the CP-violation phase. The left panel shows the expected CP violation significance as a function

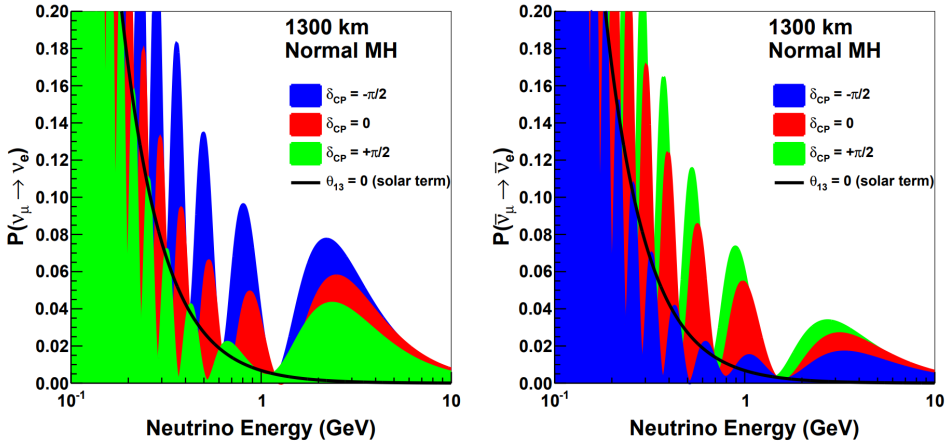

Figure 2.2: Appearance probability at a baseline of 1300 km, as a function of neutrino energy, for $\delta_{CP} = -\pi/2$ (blue), 0 (red), $\pi/2$ (green), for neutrinos (left) and antineutrinos (right), for normal ordering. The black line shows the oscillation probability if θ_{13} were equal to zero [51].

of the true δ_{CP} value, assuming normal neutrino mass ordering, for exposures of seven and ten years of data, and considering the staged deployment of the Far Detector modules. Sensitivity is maximal at $\delta_{CP} = \pi/2$ and decreases around CP-conserving values of δ_{CP}. The median CP violation sensitivity reaches 5σ for a small range of values after an exposure of seven years in normal ordering. The right panel shows the significance of the determination of CP violation in normal mass ordering for 75% and 50% of the δ_{CP} values, and when $\delta_{CP} = -\pi/2$, as a function of exposure in kt-MW-years. CP violation can be observed at 5σ after about seven years (which corresponds with 336 kt-MW-years) if $\delta_{CP} = -\pi/2$ and about 10 years for 50% of δ_{CP} values. CP violation can be observed at 3σ after about 13 years of running for 75% of the δ_{CP} values [58].

Mass ordering sensitivity The significance for the determination of the mass ordering as a function of the true value of $\delta_C P$ is shown in Fig. 2.4.a, with the same exposures described above. The characteristic shape of the diagram is due to the near-degeneracy between matter and CP violating effects that occur close to $\delta_{CP} = \pi/2$ for normal ordering.

The significance, as a function of exposure in years, that can be determined for 100% of δ_{CP} values and when $\delta_{CP} = -\pi/2$, is shown in Fig.2.4.b . DUNE will be able to establish the neutrino mass ordering at a 5σ level for 100% of δ_{CP} values after between two and three years, so the plot only extends to seven years of exposure, corresponding to 500kt $\cdot$ MW-years.

Oscillation parameters measurement DUNE will make precision measurements

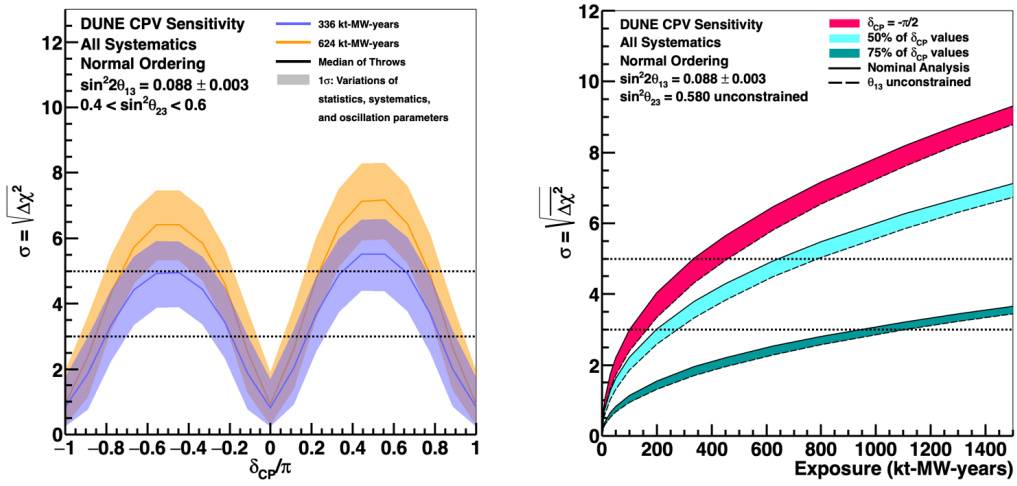

Figure 2.3: Left: Significance of the DUNE determination of CP violation as a function of the true δ_{CP} value for 336 kt-MW-years (blue) and 624 kt-MW-years (orange) of exposure. The width of the bands covers 68% of fits in which random throws are used to simulate statistical variations and select the true values of oscillation and systematics parameters. The median sensitivities are represented by the solid lines. Normal ordering is assumed. Right: Significance of DUNE's determination of CP violation for $\delta_{CP} = -\pi/2$ and for 50% and 75% of possible δ_{CP} values, as a function of exposure. Normal ordering is assumed. The widths of the bands are due to the application of an external constraint on $\sin^2 2\theta_{23}$.[58]

of all parameters that describe neutrino oscillations and improve our understanding of the phenomenology of oscillations. The least known mixing angle, θ_{23}, will be measured with a precision of at least 1°, even near 45°. This is possible by performing a combined analysis of the $\nu_\mu \rightarrow \nu_\mu$ and $\nu_\mu \rightarrow \nu_e$ channels, depending on $\sin^2 2\theta_{23}$ and $\sin^2 \theta_{23}$ respectively. The sensitivity of DUNE to the octant of θ_{23}, and the resolution of the value itself, is presented in Figure 2.5.

2.2.2 Study of Supernova and solar neutrinos

The DUNE far detector is sensitive to neutrinos produced by the Sun and in core-collapse supernovae with energies in the range of 5-100 MeV. Charged-current interactions of neutrinos from around 5 MeV to several tens of MeV create short electron tracks in liquid argon, potentially accompanied by gamma-ray and other secondary particle signatures.

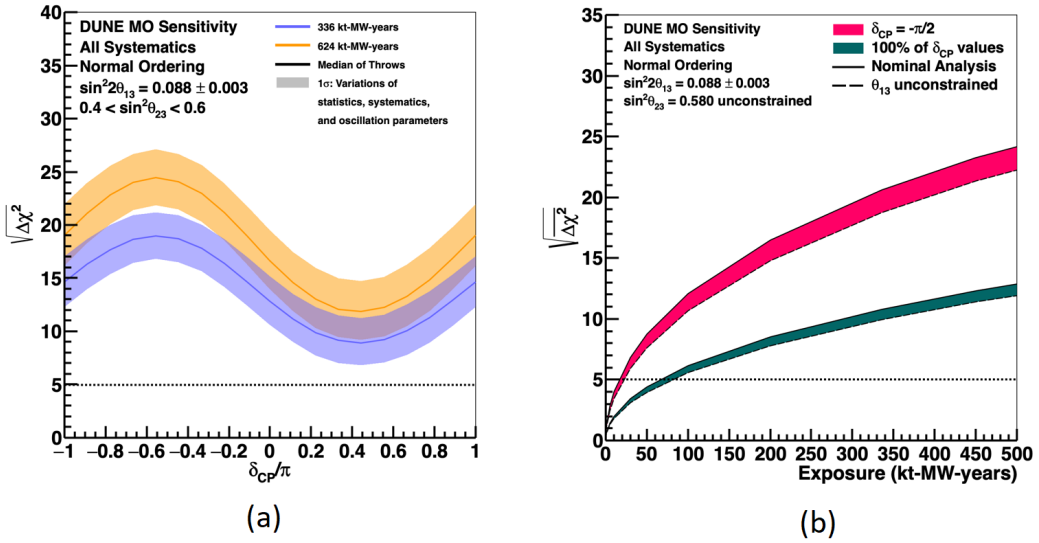

Figure 2.4: (a) Significance of the DUNE determination of the neutrino mass ordering as a function of the true δ_{CP} value for 336 kt-MW-years (blue) and 624 kt-MW-years (orange) of exposure. The width of the bands covers 68% of fits in which random throws are used to simulate statistical variations and select the true values of oscillation and systematics parameters. The median sensitivities are represented by the solid lines. Normal ordering is assumed. (b) Significance of DUNE's determination of the neutrino mass ordering for $\delta_{CP} = -\pi/2$ and for 100% of possible δ_{CP} values, as a function of exposure. Normal ordering is assumed. The widths of the bands are due to the application of an external constraint on $\sin^2 2\theta_{23}$.[58]

In a core-collapse supernova, the neutrino signal starts with a short, sharp "neutronization" burst primarily composed of ν_e . This is followed by an "accretion" phase lasting several hundred milliseconds and then a "cooling" phase which lasts about 10 seconds and represents the bulk of the signal [59]. Although the electron neutrino flavor dominates during burst and accretion, the three flavors are equalized during cooling (see Fig. 2.6). Information about the progenitor, the collapse, the explosion, and the remnant, as well as information about neutrino properties, is contained in this signal.

The expected energy threshold of DUNE is a few MeV of deposited energy, and the expected energy resolution is around $10 - 20\%$ for energies in the few tens of MeV range. Although the expected event rate varies significantly among models of supernova bursts, the 40-kt (fiducial) DUNE detector would be expected to observe approximately 3000 neutrinos from a supernova burst at a distance of 10 kpc in the charged current

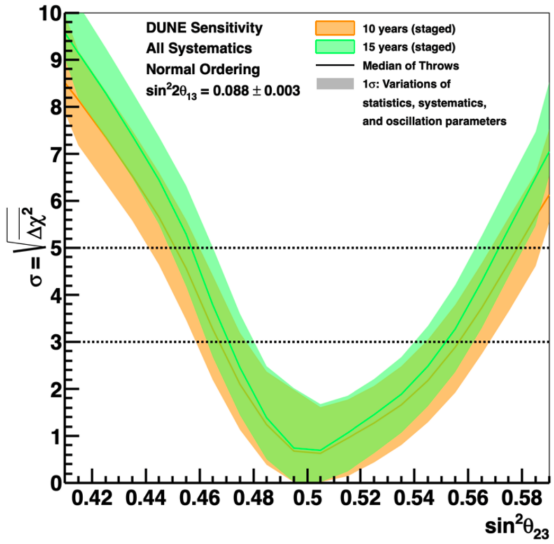

Figure 2.5: (b) Sensitivity to the determination of the θ_{23} octant, as a function of the true $\sin^2\theta_{23}$ value, for ten (orange) and fifteen (green) years of exposure. Normal ordering is assumed. The width of the bands covers 68% of fits with statistical variations and true parameter values selected by random throws. The solid lines show the median sensitivities [58]

interactions with the Argon nuclei (ν_eCC and $\bar{\nu}_e$CC). The DUNE capability to detect ν_e CC is unique among other supernova neutrino detectors, since other experiments such as Hyperkamiokande and JUNO are primarily sensitive to $\bar{\nu}_e$ [36, 54].

If a supernova burst occurs during DUNE data taking, DUNE data will be able to validate or discard some of the current stellar evolution models. Also, the detection of the neutrino burst will be a prompt alert for astronomers, since the supernova neutrino burst precedes the electromagnetic signal. DUNE will be even capable of promptly point to the region of the sky where the supernova originates, by reconstructing the direction of electrons. Furthermore, measurement of neutrino flux during the neutronization burst by DUNE would be a signature of mass ordering, since it is strongly suppressed in the normal ordering case compared to the inverted ordering[51] .

Solar neutrinos are also potentially detectable. However, because of the presence of low-energy backgrounds, such as radioactive decays, the detection of these neutrino sources is very challenging. The solar neutrino event rate for a final Far Detector fiducial mass of 40 kt is of ~ 100 per day. Initial studies suggest that with a sophisticated event selection and possibly additional shielding a high-statstics solar neutrino sample could be selected, which will be able to improve the measurement of Δm^2_{21} [51].

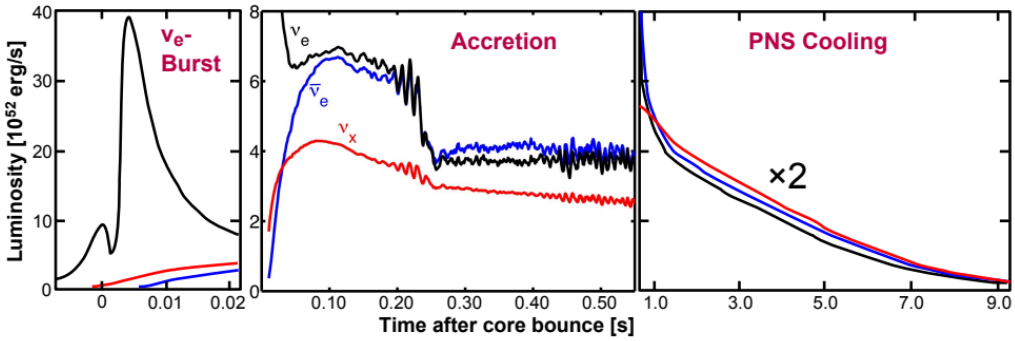

Figure 2.6: Neutrino luminosities (υ_e : black; $\bar{\upsilon}_e$: blue; υ_x as one species of $\upsilon_\mu, \bar{\upsilon}_\mu, \upsilon_\tau, \bar{\upsilon}_\tau$: red) during main neutrino-emission phases: Burst (left), accretion (center) and cooling (right). [59]

2.2.3 Beyond Standard Model searches

Sterile neutrino mixing Experimental results in tension with the three-neutrino framework, which can be interpreted as mixing between known active neutrinos and one or more right-handed-only sterile states, have led to a diverse search program. The potential mixing of sterile neutrinos with active ones can distort the standard oscillation probabilities, as shown in Fig. 2.7. DUNE is sensitive over a broad range of potential sterile neutrino mass splittings by looking for disappearance of charged-current and neutral-current neutrino interactions over the long distance separating the ND and FD, as well as over the short baseline of the ND. DUNE is expected to improve significantly on the sensitivities of previous probes.

Non-unitarity of the PMNS matrix Models that postulate the existence of sterile neutrino states imply that the 3×3 Pontecorvo-Maki-NakagawaSakata (PMNS) matrix is not unitary due to mixing with these additional states. This would imply a deviation from unitarity of the PMNS matrix which, if of order 10^{-2}, would decrease the event rate at DUNE and thus its reach to the standard parameters.[51]

Nonstandard Interactions (NSI) Non-standard neutrino interactions, affecting neutrino propagation through the Earth, can significantly modify the data to be collected by DUNE, provided that the new physics parameters are large enough. Taking advantage of its very long baseline and wideband beam, DUNE is sensitive to these probes.[60]

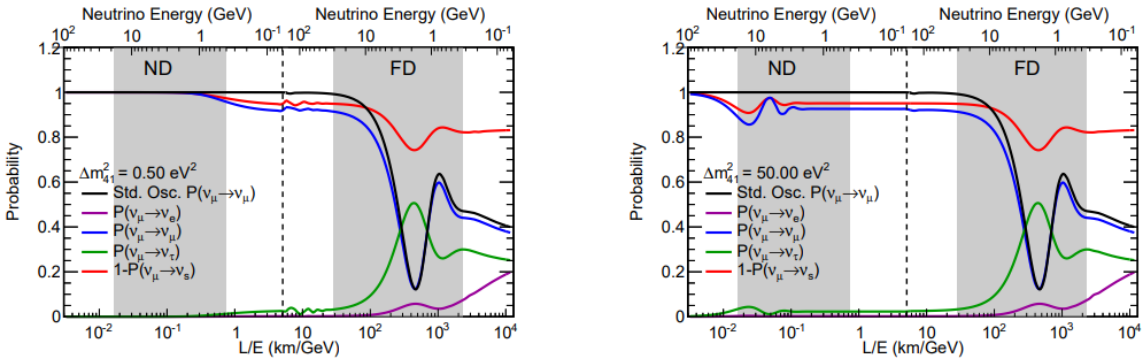

Figure 2.7: Regions of L/E (gray-shaded areas) probed by the DUNE detectors compared to 3-flavor and 3+1-flavor (including one sterile state) neutrino disappearance and appearance probabilities. The top axis shows true neutrino energy, increasing from right to left. The plots show the probabilities assuming mixing with one sterile neutrino with $\Delta m^2_{41} = 0.05\text{eV}^2$ (left) and $\Delta m^2_{41} = 50\text{eV}^2$ (right), respectively. [60]

Neutrino trident production at the ND. Neutrino trident production is an electroweak process in which a neutrino, scattering off the Coulomb field of a heavy nucleus, generates a pair of charged leptons. The high-intensity muon-neutrino flux at the DUNE ND will result in a considerable trident event production rate, providing excellent prospects for improving previous measurements[60]. A deviation from the event rate predicted by the SM could be an indication of new interactions mediated by the corresponding new gauge bosons. Of particular interest is the class of models that introduce a Z' neutral boson associated with a new $U(1)_{L_\mu - L_\tau}$ gauge symmetry, as it could explain the long-standing discrepancy between the theoretical calculation and the measurement of the muon $g-2$. The sensitivity of DUNE in the parameter space of the Z' mass and its gauge coupling g' is shown in Figure 2.8.

Proton decay Some Grand Unified Theories (GUTs) beyond the Standard Model predict the barion number symmetry breaking, allowing protons to decay. DUNE will search for two proton decay modes: $p \to e^+\pi^0$ and $p \to K^+\bar{\nu}$ (Fig. 2.9. The former is interesting, since it has the highest branching ratio among the predicted decays. The latter can be used specifically in DUNE since stopping kaons have a higher ionization density than particles with lower masses. Therefore, a LArTPC is able to recognize a K^+ track efficiently.

If proton decay is observed, the lifetime will be measured; otherwise a lower limit on the proton lifetime of $1.3 \cdot 10^{34}$ years is expected if no signal is observed in 10 years

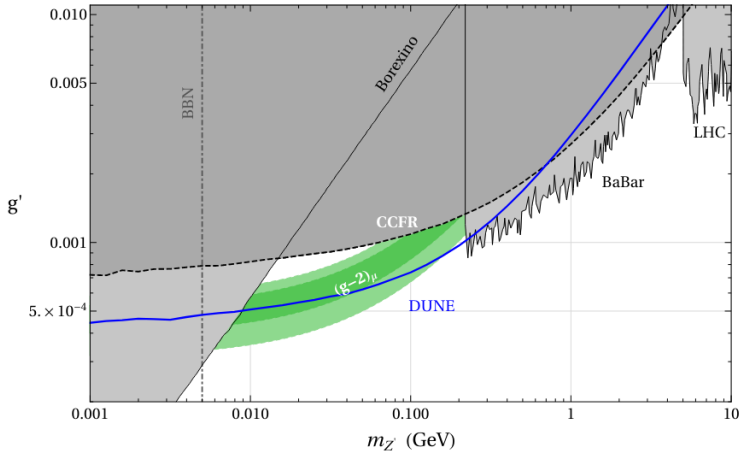

Figure 2.8: Projected DUNE sensitivity (solid blue line) and existing constraints (gray shaded area) in the $L_\mu - L_\tau$ parameter space. Shown in green is the region where the $(g-2)\mu$ anomaly can be explained at the 2σ level. The DUNE sensitivity shown by the solid blue line assumes 6 years of data running in neutrino mode. [60]

running. With its total fiducial volume, DUNE will improve the current limits established by Super-Kamiokande by an order of magnitude with 90% C.L., after running for 20 years [60].

Search for Boosted Dark Matter (BDM) Conventional direct DM searches use non-relativistic scattering of DM particles with nuclei of the detection medium, resulting in energy deposits well below the expected threshold energy of the DUNE FD. On the contrary, typical energy deposits in association with a relativistic scattering of boosted DM would readily surpass the threshold. A possible mechanism to create relativistic DM in our universe is the boosted dark matter (BDM) scenario [61], which hypothesizes two stable DM species, a heavier χ_0 and a lighter χ_1. When a pair of χ_0 annihilates into a pair of χ_1 in an astrophysical source, the mass gap between the two species allows the χ_1 to acquire a large boost factor and induce relativistic scattering signatures in terrestrial detectors. Fig. 2.10 shows two such possible detection processes. The one on the left corresponds to the ordinary elastic scattering with visible target recoil; the process on the right assumes a nonminimal dark-sector scenario allowing the transition to a heavier unstable state (χ_2) which subsequently disintegrates back to χ_1 together with possibly visible secondary particles in addition to the primary target recoil.

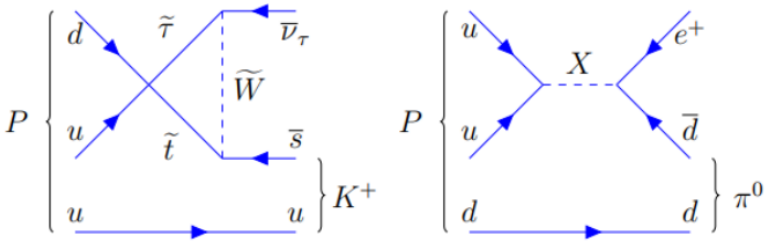

Figure 2.9: Feynman diagrams of proton decay modes according to GUTs.

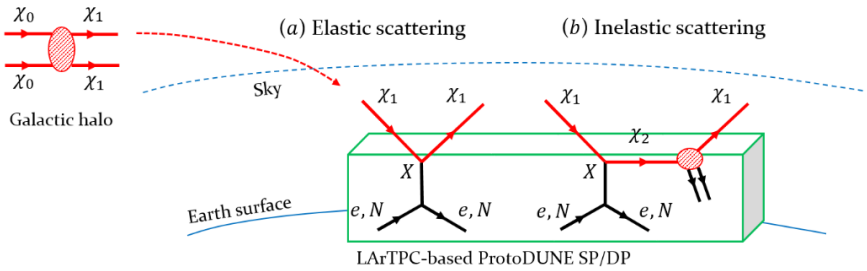

Figure 2.10: Sketch of the detection process of boosted dark matter in the DUNE FD. [62]

2.3 DUNE design

The remainder of this chapter will outline the features, design choices, and science goals of the components of the DUNE experiment: the Long Baseline Neutrino Facility (LBNF) beam, the far detector (FD), and near detector (ND).

2.3.1 Neutrino beam

The Long Baseline Neutrino Facilitity (LBNF) will provide a neutrino beam with appropriate intensity and energy range to meet the requirements of the long-baseline neutrino physics conducted at DUNE. The wideband neutrino beam will be aimed at the SURF detectors 1.5 km underground at a distance of 1300 km from the production point.
The primary proton beam will be provided by the PIP-II upgrade of the Main Injector accelerator at Fermilab, which will deliver a 1.2 MW proton beam in the energy range from 60 to 120 GeV at the start of DUNE operations. Its main specifications are listed in Table 2.3. PIP-II will also provide a platform to extend the beam power to DUNE

to > 2 MW and a further update of the accelerator complex will allow up to 2.4 MW of beam power by 2030.
The proton beam will be extracted at the new MI-10 installation, and will be bent to establish the final trajectory toward the far detector. The beam will hit a target made of graphite and beryllium. The hadronic showers produced as a result contain mainly pions and kaons, which are focused by magnetic horns into a $\sim$200 m long decay pipe. Inside the pipe, these particles decay primarily into $\mu^{\pm}$ and $\overset{(-)}{\nu}_{\mu}$.
By selecting positive or negative mesons in the magnetic horns, the beam will be able to run in neutrino or antineutrino mode. Muons are stopped in a shielding after the decay pipe, but some of them can decay, contributing to the neutrino beam contamination by introducing other neutrino flavors into the beam.

Parameter	Value
Energy	120GeV
Protons per cycle	7.5×10^{13}
Spill duration	1.0×10^{-5} s
POT per year	1.1×10^{21}
Cycle Time	1.2 s
Beam Power	1.2MW
Beam size at target	$1.5 - 1.7$ mm
$\Delta p/p$	$11 \times 10^{-4} 99\%$ $(28 \times 10^{-4} 100\%)$
Transverse emittance	$30\pi\mu m 99\%$ $(360\pi\mu m 100\%)$
Beam divergence (x, y)	$15 - 17\mu$rad

Table 2.3: Summary of the main primary proton beam parameters [63]

The neutrino beam will show a wide energy spectrum from 0.5 GeV, to 5 GeV which will allow the coverage of the first and second neutrino oscillation maxima, which are approximately at 2.4 and 0.8 GeV for $L \simeq 1300$ km. A beam spill will be 10 μs long, and its microstructure entails six batches each comprised of 84 53.1 Mhz bunches. Figure 2.11 shows the expected neutrino energy spectrum, as well as the flavor composition at the Far Detector.

2.3.2 Far Detectors

DUNE Far Detector, located 1.5 km underground at SURF, will consist of four LAr-TPC detector modules with a fiducial mass of at least 10 kton of liquid argon each. Each de-

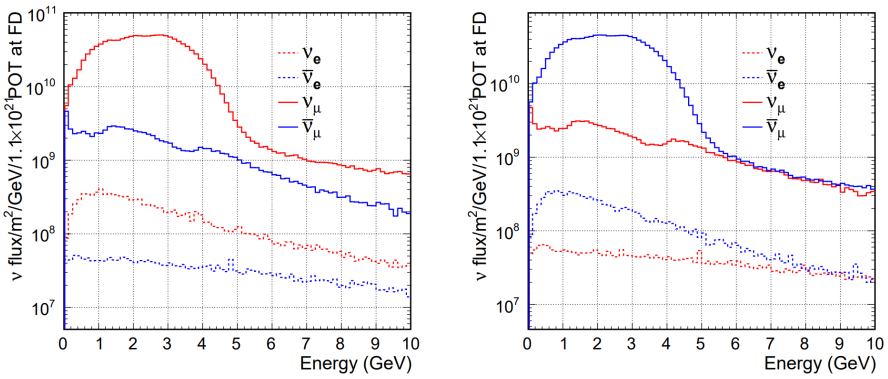

Figure 2.11: Neutrino fluxes at the Far Detector for the beam operating in neutrino mode (left) and in antineutrino mode (right).[51]

tector will be placed inside a cryostat of dimensions 15 m × 14 m × 62 m containing a total mass of 17.5kton. The LArTPC technology will provide good tracking and calorimetry performance, and the use of four modules of identical size will allow flexibility for staging construction and for the potential evolution of the LArTPC technology [51].

Several technologies have been considered for the four modules, and there is a full R&D program to validate the different technologies within the ProtoDUNE program at the CERN neutrino platform. The first module will be a single-phase horizontal drift module (DUNE SP) since the design was validated during the successful operation of ProtoDUNE Single-Phase. This is a prototype detector approximately 1/20 the size of a full-scale FD module and uses the same components as the final detector. The large-scale prototype has allowed to validate key aspects of the TPC design, engineering procedures, and collect valuable calibration data from a hadron test beam. ProtoDUNE-SP started collecting data in 2018 and a new run is planned to start in 2023.
The second module was originally proposed as a dual-phase design; however, the results of the prototype phase changed the strategy, and the dual-phase technology has been discarded in its current state of development for the second module of DUNE's Far Detector. An alternative proposal of a single-phase module with vertical drift is being considered for the second module as an evolution of the dual-phase design but renouncing to the gas phase. This is known as the Vertical-Drift design. This approach is being tested to demonstrate its viability, and a dedicated effort is underway at CERN to build a prototype and validate the design. The technology to implement in the third and fourth modules has not yet been decided. The main features of DUNE's two LArTPC detector designs are outlined below.

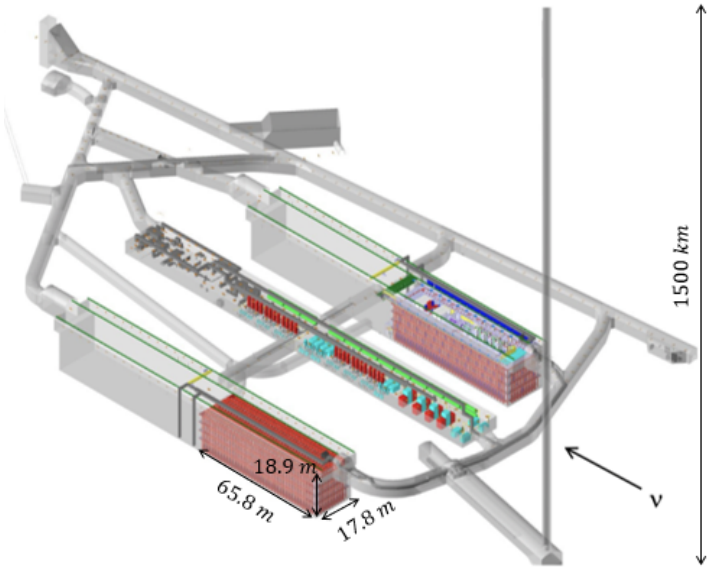

Figure 2.12: Underground caverns for DUNE FD and cryogenics systems at SURF, in South Dakota. The scheme shows the first two Far Detector modules in place [51]

Horizontal drift LArTPC

In the horizontal drift LAr TPC design, charged particles passing through the detector ionize the argon atoms and the ionization electrons drift in an intense electric field to the Anode Assembly Plane (APA) with a timescale of milliseconds. The APA consists of layers of active wires that form a grid, with the relative voltage between the layers selected so that the drifting electrons will only produce bipolar induction signals on all but the last layer, where they are instead absorbed and induce a monopolar signal.
Liquid Argon is an excellent scintillator that emits vacuum ultraviolet light (VUV) with a 127 nm wavelength. The prompt scintillation light, which crosses the detector with a nanosecond timescale, is collected by photon detectors after being shifted into the visible range: this provides a starting time t_0 for the ionization. The event topology along the drift direction is thus reconstructed from the timing of the ionization electrons reaching the anode. The coordinates along directions perpendicular to those of drift are given by the pattern of currents on the grid of anode wires. Fig. 2.13 shows the general operating principle of a LArTPC [64].

The main requirement of the LAr used in TPC is its purity, as electronegative contaminants can absorb ionization electrons, while nitrogen contaminants can quench scintillation photons. The target purity of electronegative contaminants in argon is below

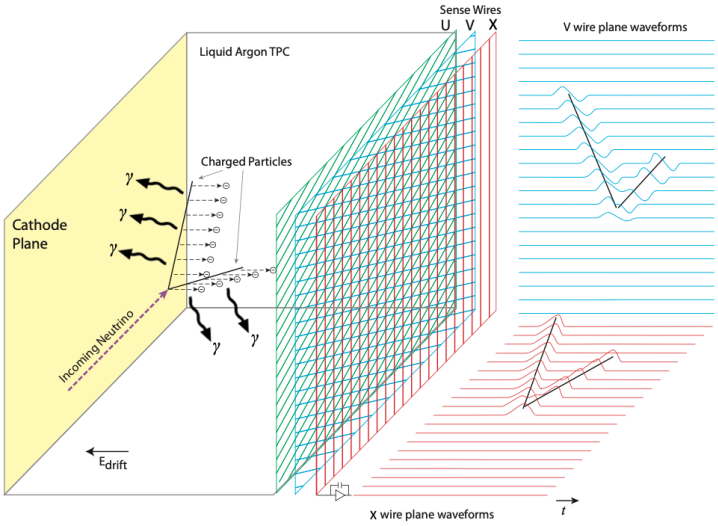

Figure 2.13: General operating principle of a single-phase LArTPC. [64]

100 ppt O_2 equivalent, enough to ensure an ionization-electron lifetime > 3 ms at the nominal drift voltage. This ensures the Signal-to-Noise-Ratios that are necessary to perform pattern recognition and track separation. Nitrogen contaminants must be kept below 25ppm to achieve the required minimum of 0.5 photoelectrons per MeV detected for events in all parts of the detector. The purity of LAr is maintained by constantly cycling argon through the purification system [64].

The DUNE single-phase LArTPC will have a total mass of 17.5kt. The module will be housed inside a cryostat of 65.8 m $\times$ 17.8 m $\times$ 18.9 m outer dimensions. The volume is divided by alternating anode and cathode walls, with a maximum drift length of 3.5 m. Each cathode wall is formed by an array of 150 Cathode Plane Assemblies, 1.2 m $\times$ 4 m panels biased at -180kV. With the anode walls kept close to the ground, a uniform 500 V/m electric drift field is produced throughout the drift volume. A field cage around the active volume composed of aluminum rings ensures a field uniformity better than 1% throughout the active volume.

The anode walls are each composed of 50 Anode Plane Assemblies (APA) units of 6 m $\times$2.3 m dimensions. The APAs, the scheme of which is shown in Fig. 2.14 are two-sided, with three active wire layers and an additional shielding layer wrapped around them. The spacing of the wires is $\sim$5 mm.

The readout cold electronics (CE) are attached to the top end of the top APA and to the bottom end of the bottom APA. Low LAr temperature benefits these front-end electronics through the reduction of thermal noise.

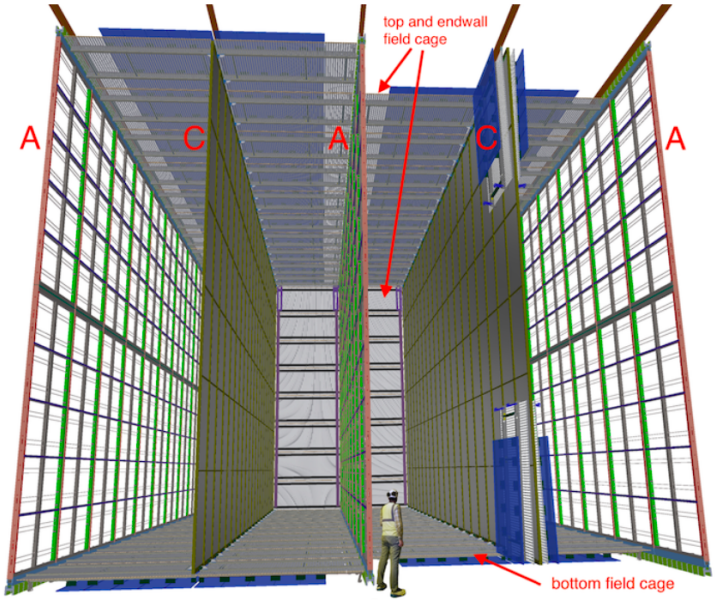

Figure 2.14: A 10 kt DUNE far detector SP module, showing the alternating anode (A) and cathode (C) planes, as well as the surrounding Field Cage surrounding the field regions. The field cage on the right is shown in its undeployed state [64].

Charged particles passing through the liquid argon will produce scintillation light, in addition to ionization, with approximately 40×10^3 photons per MeV. The scintillation light detection is performed by special devices called X-Arapucas, bars that run the width of the 2.3 m of the APA placed behind the anode wire-planes. Ten X-Arapucas are mounted on each of the APAs. Each X-Arapuca bar consists of four Arapuca cells with transparent VUV light-transparent dichroic filters, alternated with wavelength shifters (WLS) plates to convert UV photons to the visible spectrum at 430 nm. The visible photons emitted inside the WLS plate at an angle toward the surface greater than the critical angle reach the SiPMs at the edges. The visible photons that escape the WLS in turn are reflected back to the wavelength shift plates by the dichroic filters, since the former have an optical cut-off for wavelengths > 400 nm. The working principle of the X-Arapuca cells is illustrated in Fig. 2.15, while the scheme of the X-Arapuca modules and their placement within the APAs are shown in Fig. 2.16.

Vertical drift LArTPC

For the second module of the DUNE Far Detector, a vertical-drift LArTPC has been proposed, due to the experience gained by the run of ProtoDUNE at CERN. In this

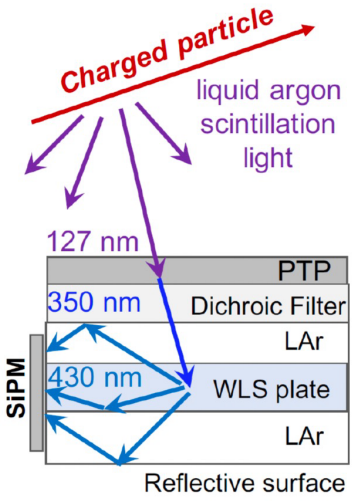

Figure 2.15: Working principle of an X-Arapuca cell: the VUV LAr scintillation light is shifted into the visible spectrum upon entering the module. The escaping visible photons are redirected back towards the SiPM by the dichroic filters.

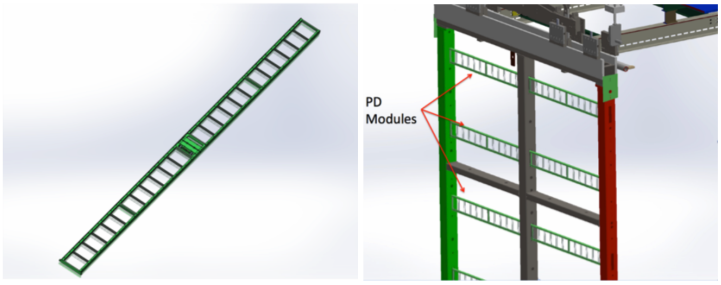

Figure 2.16: Left: an X-Arapuca photon detection module, showing the 24 X-Arapuca cells. The 48 SiPMs that detect the light from the cells are long the long edges of the module. Right: X-Arapuca modules mounted inside an APA. [64]

design, the active volume is divided by the cathode plane that hangs at mid-height in the module, separating two volumes with a maximum drift length of 6.5 m. Two 60 m $\times$13.5 m anode planes are placed at the top and bottom of the detector. The cathode is biased at -325 kV and the anode planes are grounded. The field cage ensures the uniformity of the electric field at 500 V/cm.

In this configuration, electrons drift vertically towards the top (in the top half) and the bottom (in the bottom half), where they are read out. The TPC anodes are based on

a perforated printed circuit board system because they can be hung horizontally without suffering significant deformations. Each section of anode plane will consist of two PCB boards, with the electron drifting through the amplified electric field in the induction PCB towards the collection board. The cathode will be a thin structure to reduce the loss of active volume and roughly 60% transparent to allow the free flow of the argon.

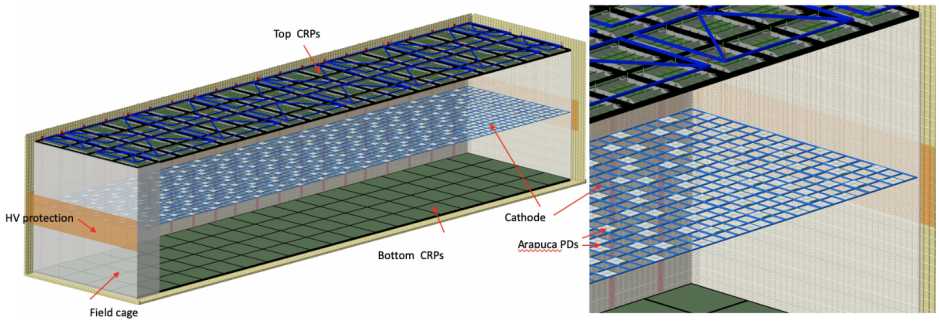

Figure 2.17: Configuration of the Vertical Drift concept [65]. The drift volume is segmented by the cathode placed in the middle.

The photon detection system is based on X-Arapucas.They will be placed on the walls of the cryostat behind the field cage, designed to be semi-transparent, and on the cathode surface. The latter position has most importantly required the development of novel optoelectronic systems for signal and power transmission: a power-over-fiber solution for power distribution and an analog optical transmitter that allows the digitization of the SiPM signals in warm conditions [65].

The VD-TPC concept is currently undergoing an intense R&D campaign of test and validate its different systems. ProtoDUNE-VD installation is underway.

2.3.3 Near Detector complex

The Near Detector complex will be located 574 m away from the source of the LBNF neutrino beam and 62 m underground in the DUNE ND Hall, shown in Fig. 2.18.

During Phase I of operations, the ND will include three primary detector components: ND-LAr and TMS, and SAND. In phase II, it is planned that TMS will be replaced by ND-GAr. According to the DUNE Precision Reaction Independent Spectrum Measurement (DUNE-PRISM) program, the ND-LAr, TMS, and ND-GAr can be moved sideways to perform off-axis measurements. The capability to move off-axis will allow to study neutrino interactions with different energy spectra at different off-axis locations. It is planned that these two detector components will spend 50% of the time off-axis, while

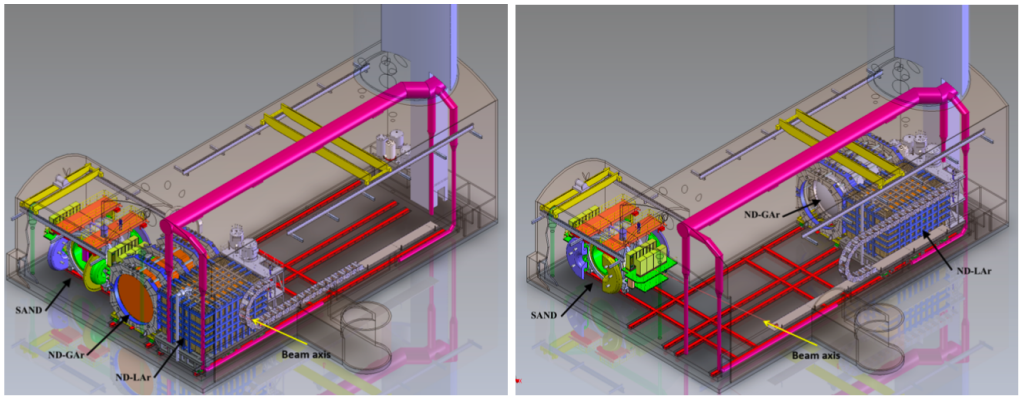

Figure 2.18: Schematic of the DUNE ND hall with all components in the on-axis configuration (left) and with ND-LAr and ND-GAr in an off-axis configuration (right). The SAND detector is on-axis, with the beam indicated by the yellow arrow. [66]

SAND is the only detector permanently on the beam axis, located in a dedicated alcove in the ND hall, to monitor the beam changes with the required sensitivity, constrain systematics, and provide a rich neutrino physics program [66]. The total rate of neutrino events expected in the ND is ~ 0.14 events / ton / spill and the total number of ν_μCC events / year / ton $\cong 1.6 \cdot 10^6$. These values are obtained assuming approximately $7.5 \cdot 10^{13}$ protons extracted every 1.2 s at 120 GeV proton energy and a corresponding protons-on-target (POT) per year of $1.1 \cdot 10^{21}$ POT/ year for an accelerator complex efficiency of 57% [66].
The Near Detector complex is supposed to serve as the experiment's control, measuring and monitoring the beam, constraining the flux and providing essential input for the neutrino interaction model. To achieve the precision required by DUNE's goals, the experiment must minimize systematic uncertainties and each component of the neutrino energy spectrum, namely, the cross section, the flux, and the energy response, must be constrained independently with data in order to avoid relying on models.
Both Far and Near detectors will measure the energy spectrum of neutrinos, using the differential rates of ν_e and ν_μ, given by:

$$\frac{dN^{FD}_{\nu_x}}{dE_{rec}}(E_{rec}) = \mathcal{N}^{FD}\int \Phi^{FD}_{\nu_\mu}(E_\nu) P_{\nu_\mu \to \nu_x}(E_\nu) \sigma^{Ar}_{\nu_x}(E_\nu) R^{Ar}_{\nu_x}(E_\nu, E_{rec}) \epsilon^{FD}_{\nu_x}(E_\nu, E_{rec}) dE_\nu, \tag{2.1}$$

$$\frac{dN^{ND}_{\nu_x}}{dE_{rec}}(E_{rec}) = \mathcal{N}^{ND}\int \Phi^{ND}_{\nu_\mu}(E_\nu) \sigma^{Ar}_{\nu_x}(E_\nu) R^{Ar}_{\nu_x}(E_\nu, E_{rec}) \epsilon^{ND}_{\nu_x}(E_\nu, E_{rec}) dE_\nu, \tag{2.2}$$

in which $\mathcal{N}$ is a normalization factor, E_ν is the true neutrino energy, while E_{rec} is the reconstructed one. σ_ν is the neutrino interaction cross section, R_ν is the probability that a neutrino produces a charged particle and ϵ_ν is the detector efficiency.
Near Detector's measurements are needed to constrain the ratio between near and far flux, the absolute neutrino flux, the detector efficiency and the neutrino interaction in argon, which cross section appears in the ratio between the fluxes [51]:

$$\frac{dN^{FD}_{\nu_e}}{dN^{ND}_{\nu_\mu}} = \frac{\int \Phi^{ND}_{\nu_\mu}(E_\nu) P_{\nu_\mu \to \nu_x}(E_\nu) F(E_\nu) \sigma^{Ar}_{\nu_e}(E_\nu) R^{Ar}_{\nu_e}(E_\nu, E_{rec}) \epsilon^{FD}_{\nu_e}(E_\nu, E_{rec}) dE_\nu}{\int \Phi^{ND}_{\nu_\mu}(E_\nu) \sigma^{Ar}_{\nu_\mu}(E_\nu) R^{Ar}_{\nu_\mu}(E_\nu, E_{rec}) \epsilon^{ND}_{\nu_m u}(E_\nu, E_{rec}) dE_\nu}, \quad (2.3)$$

Since the aim of DUNE is to reconstruct neutrino events, it is important to understand in detail neutrino interactions in argon. They can be modeled by considering a neutrino that collides with nucleons, then scattering can occur and the nucleons can produce mesons. Subsequently, these particles can interact with other nucleons while traveling in argon. The interactions of these secondary particles contribute the most to the systematic uncertainties on the interactions.

DUNE is interested especially in the energy range between 0.5 GeV and 10 GeV, to cover the regions where quasi-elastic scattering (QE), resonance production (RES) and deep inelastic scattering (DIS) can happen. SAND detector in particular has the role of constraining these kinds of neutrino interactions in argon. In fact, even a small change in relative uncertainties can have substantial repercussions on the sensitivity to different parameters of interest, increasing the total exposure needed to achieve a 5σ significance and claim therefore a discovery.

In the following, the features and objectives of each of the Nd-LAr, TMS, and ND-Gar detectors are outlined. The SAND detector will be detailed in the next chapter.

ND-LAr

At the near site, the ND-LAr will be exposed to a much more intense neutrino flux than at the FD site, leading to event pile-up. To overcome this limitation, ND-LAr will be based on ArgonCube technology, consisting of a large TPC fabricated out of a matrix of smaller, optically isolated TPC modules. The modules are hosted in a common purified bath of liquid argon, which is within a custom-designed membrane cryostat. The cryostat and adjacent mezzanine cryogenics are placed on a mobile platform that allows the entire detector to be shifted off-axis relative to the neutrino beam.
Each module consists of a high-voltage cathode, a field cage that minimizes the amount of inactive material between modules, a pixel-based charge readout and a light collection system, to provide the timing necessary to associate tracks and events across the matrix.

The current design features a 5×7 matrix of modules. The subdivision of the volume will allow for smaller drift distances and times, which, together with the optical insulation, will reduce the issues with overlapping interactions. The smaller volumes will also reduce the requirements on the high voltage and argon purity.

ND-LAr will be large enough to provide the required hadronic shower containment and statistics (1×10^8 ν_μ events per year), with a fiducial mass of 67 t in a volume of 5 (along beam) $\times$ 7 (transverse to beam) $\times$3 (height) m^3. In Fig. 2.19, an illustration of ND-LAr shows the array of ArgonCube TPCs.

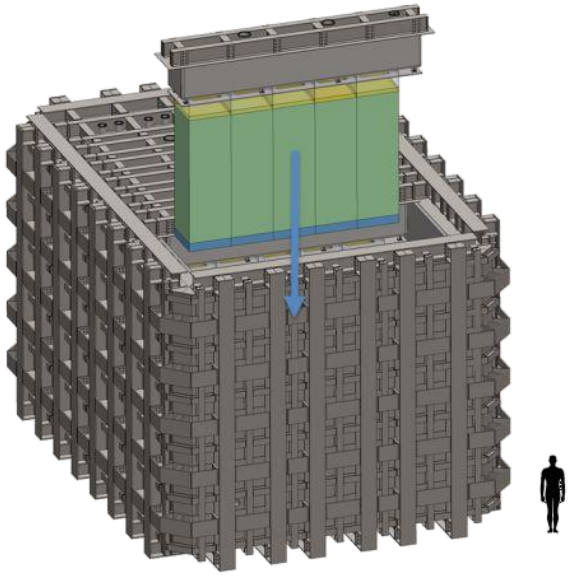

Figure 2.19: Schematic of the ND-LAr detector, showing a row of the 5×7 array of optically isolated ArgonCube modules [66].

One key aspect of ND-LAr operation is the ability to cope with a large number of neutrino interactions per spill. As discussed in Section 2.3.1, the LBNF neutrino beam consists of a 10μs wide spill, with a $\mathcal{O}$ (ns) bunch structure, delivered at a $\sim$ 1 Hz rate. This means that there will be $\mathcal{O}(50)\nu$ interactions per spill in ND-LAr. Given the relatively low expected cosmic ray rate during the beam spill ($\sim$ 0.3/ spill at 60-m depth), this beam-related pile-up is the primary challenge confronting the reconstruction of the ND-LAr events. The 3D pixel charge will be read out continuously. The slow drifting electrons (with charge from the cathode taking $\sim$ 300μ s to arrive across the 50 cm distance) will be read out with a time accuracy of 200 ns and a corresponding charge amplitude within a $\sim$ 2μ s wide bin. This, coupled with the width of the spill, gives a position accuracy of $\sim$ 16 mm.

TMS

ND-LAr has a reduced acceptance for muons with momentum above $\sim$ 0.7 GeV/c due to lack of containment. An additional spectrometer, called the The Muon Spectrometer (TMS), will measure the momenta and charges of muons downstream of ND-Lar.

TMS consists of a magnetized range stack with 100 layers, with the same dimensions as the ND-Lar face, 7.4 m wide $\times$5 m tall and a depth of 7 m (Fig. 2.20). Each plane is made of 192 scintillator slats, 3.5 cm wide and read out by SiPMs, alternated by steel plates of 15 mm thickness in the 40 layers upstream and 40 mm in the 60 layers downstream.

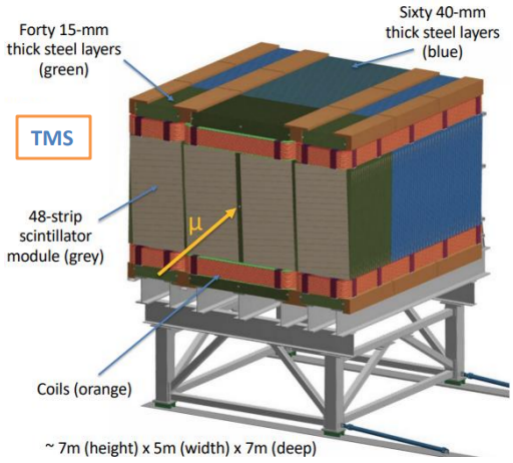

Figure 2.20: Scheme of the TMS detector.

With a magnetic field of 0.5 T, TMS will reconstruct the muon charge sign and momentum by a range with $\sim$ %5 resolution up to $\sim$ 5 GeV.

ND-GAr

The ND-GAr detector, being considered for DUNE Phase II, will be a magnetized detector system consisting of a high-pressure gaseous argon TPC (HPgTPC) surrounded by an electromagnetic calorimeter (ECAL), both in a 0.5 T magnetic field, and a muon system. A schematic of ND-GAr is shown in Figure 2.21. The basic geometry of the HPgTPC is a gas-filled cylinder with an HV electrode at its midplane, providing the drift field for ionization electrons. The gas is an argon-CH4 mixture, 90–10% (molar fraction), at 10 bar. It is oriented inside the magnet such that the magnetic and electric fields are parallel, reducing transverse diffusion to give a better point resolution. Primary

ionization electrons drift to the end plates of the cylinder, which are instrumented with multiwire proportional chambers (MWPCs) to initiate avalanches (i.e. gas gain) at the anode wires. Signals proportional to the avalanches are induced on cathode pads situated behind the wires; readout of the induced pad signals provides the hit coordinates in two dimensions. The drift time provides the third coordinate of the hit.

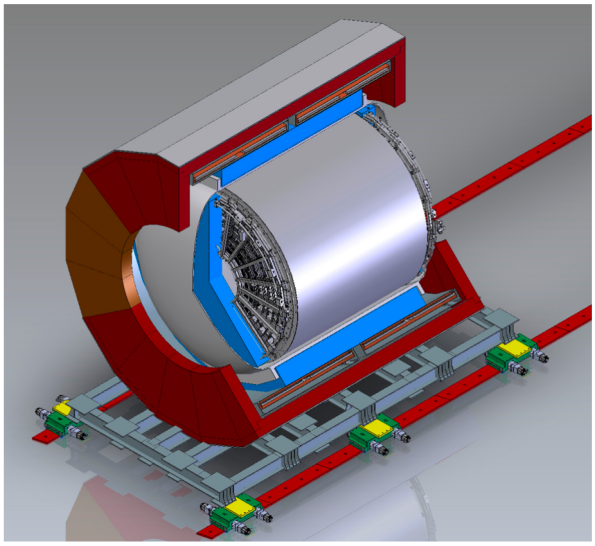

Figure 2.21: Schematic of ND-GAr which shows the HPgTPC, its pressure vessel, the ECAL,the magnet and return iron yoke. The muon-tagging system detectors are omitted [66]

With 1.0 ton Argon, ND-GAr will collect 1.6×10^6 ν_μ charged currents events per year[66]. These events can be studied with a very low momentum threshold for charged particle tracking, and with systematic uncertainties that differ from those of the liquid detectors.
Since ND-GAr can access lower-momentum protons and has charged π capabilities superior to those of ND-LAr, it will be valuable for studying the activity of charged particles near the interaction vertex. The mis-identification of pions as knocked-out protons can cause significant mis-reconstructions of neutrino energies and event topologies, in the LArTPCs.

Chapter 3

System for on-Axis Neutrino Detection

The System for on-Axis Neutrino Detection (SAND) is one of the three detector components of the DUNE near detector. It will continuously monitor the beam on-axis to produce a statistically significant neutrino beam spectrum measurement and detect spectral variations on a weekly basis.
SAND is designed to be a multipurpose detector capable of detecting neutrino interactions on different target materials, including Argon, Carbon and CH_2, performing precision tracking and calorimetry measurements. In the proposed design, a superconductive solenoidal magnet provides an axial magnetic field in which an electromagnetic calorimeter (ECAL), a tracking and target system system and a liquid Argon detector are immersed [66].
The SAND system will repurpose the already existing magnet and ECAL of the KLOE detector, which was a cylindrical collider detector previously used to study CP violation in the decays of neutral Kaons at the ϕ factory DAFNE, at the the INFN LNF laboratory in Frascati, Italy.
The chosen design for the inner tracker of SAND consists of Straw Tube Target tracker (STT) modules.The outstanding features provided by this tracking system can significantly enhance the physics program of SAND and contribute to constrain the systematic uncertainties affecting the long-baseline analyses. The GRAIN (GRanular Argon for Interactions of Neutrinos) detector is an active LAr target that is placed in the upstream region of the ECAL inner volume. It will contribute to inter-calibration with other ND detectors and to constrain the systematic uncertainty in the oscillation data analysis.
In Fig. 3.1 the external structure of the magnet and ECAL (right) and a schematic of the internal structure of SAND (on the left) are shown. The SAND physics program and

its detector components are discussed in detail in this chapter.

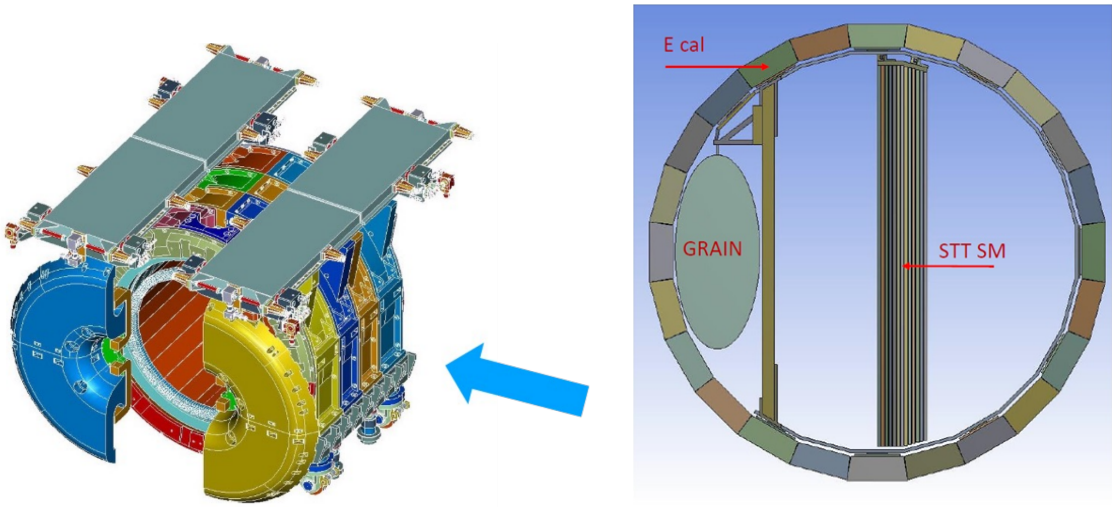

Figure 3.1: Left: KLOE magnet and ECAL. The neutrino bam direction at DUNE is shown by the arrow. Right: SAND detector cross section with its inner components.

3.1 The Physics program

The SAND detector must be able to monitor the beam on-axis, producing a statistically significant neutrino spectrum measurement in a relatively short time (one week) [67]. The SAND measurements will be decisive in fine-tuning the beam model and monitoring planned or unanticipated changes in beam flux and spectrum (e.g. target degradation). This information is essential to extract the expected FD spectra and disentangle the causes that could have induced variations in the off-axis flux observed by ND-LAr and TMS/ND-GAr.

Flux measurements

The SAND detector will determine the absolute and relative fluxes of the different neutrino components of the beam by studying the different interactions in the active volume. A precise measure of the fluxes $\Phi_{\nu(\bar{\nu})}$ is necessary to unfold the different terms that contribute to the measurement of the event rates at the ND, defined by Eq. 2.2. The various accessible measures are listed here [68]:

- Absolute ν_μ flux from $\nu + e \rightarrow \nu + e$ elastic scattering;

- Relative ν_μ flux vs. E_ν from $\nu + p \rightarrow \mu^- + p + \pi^+$with $\nu < 0.5$GeV;
- Absolute $\overline{\nu_\mu}$ flux from $\bar{\nu} + p \rightarrow \mu^+ + n$ (QE) with $Q^2 \leqslant 0.05\text{GeV}^2$: at $Q^2 = 0$ the QE cross-section is constant and dominated by β decay;
- Relative $\bar{\nu}$ flux vs. E_ν from $\bar{\nu} + p \rightarrow \mu^+ + n$ (QE with $\nu < 0.25$GeV);
- Ratio of $\bar{\nu}_\mu/\nu_\mu$ fluxes vs. E_ν from coherent π^-/π^+on C: this is performed by measuring the ratios within the same beam polarity from coherent interactions on C (isoscalar) inside CH_2 and graphite targets in the STT;
- Ratio of ν_c/ν_μ and $\bar{\nu}_e/\bar{\nu}_\mu$ from $\nu(\bar{\nu}) - H$ CC interactions;
- Determination of parent $\mu/\pi/K$ distribution from $\nu(\bar{\nu})$CC on H and CH_2 at low-ν : this measure requires a fit to both the ν_μ and $\bar{\nu}_\mu$ distributions.

As aforementioned, the measure of the neutrino event rate is the convolution of many factors, including the neutrino-nucleon interaction cross section. LAr is therefore used at both the near and Far Detector to have the same nuclear target and thus cancel the effects of nuclear smearing, reducing the uncertainties given by the theoretical models. However, a comparison between the two detectors spectra is difficult. Indeed, the large difference between the angular acceptance of the near and far detectors makes the observed spectra different. In addition, the Near Detector suffers from pile-up events due to the high intensity of the beam. The idea is to constrain the Near Detector measurements using information on flux, cross section, energy reconstruction and detector effects. GRAIN will provide a measurement of the neutrino spectrum, as well as of its flavor and it will be used to study in deep the neutrino-Argon cross section. Moreover, since ND-LAr and ND-GAr detectors will move off-axis for about half of the operation time, GRAIN will constitute a complementary Ar target permanently located on-axis.

Constraints on the nuclear effects

As discussed in Section 2.3.3, constraints on nuclear effects in Ar can be obtained by a comparison between different neutrino-nucleus interaction topologies.
Indeed the STT modules allow to study the neutrino interaction on H by subtracting measurements on dedicated graphite (pure C) targets from those on the CH_2 plastic targets. Moreover, since the H target is at rest, the neutrino Charged Current (CC) events are perfectly balanced in a plane transverse to the beam direction (up to the tiny beam divergence), so the muon and hadron vectors are back-to-back in the same plane. Instead, events from heavy nuclear targets are affected by both initial- and final-state

nuclear effects, resulting in a significant missing transverse momentum and a smearing of the transverse plane kinematics. The results of the dedicated analysis show that purities of $80-95\%$ of the selected H samples are achievable, with efficiencies of kinematic selection in $75-95\%$ depending on the process considered [68].
Having access to $\nu(\bar{\nu})-H$ interaction allows the measurement of the neutrino flux. Once the fluxes are precisely measured, from Eq. 2.2 one is left with the convolution of three terms $\sigma^m_{\nu_x} R^m_{\nu_x} \epsilon^m_{\nu_x}$. Here, a key role is played by Hydrogen whose $R^H_{\nu_x} \equiv 1$. From a comparison between Ar and H interactions:

$$\frac{\mathcal{N}^{Ar}_{\nu_x}}{\mathcal{N}^{H}_{\nu_x}} = \frac{\sigma^{Ar}_{\nu_x} R^{Ar}_{\nu_x} \epsilon^{Ar}_{\nu_x}}{\sigma^{H}_{\nu_x} \epsilon^{H}_{\nu_x}} \tag{3.1}$$

since the ratio of the efficiencies ϵ is essentially defined by $\delta p/p$ (calibrated to 0.2% from the K_0 mass peak), and $\sigma^H_{\nu_x}$ can be accurately measured given the expected statistics, one can directly constrain the product $\sigma^{Ar}_{\nu_x} R^{Ar}_{\nu_x}$. This is the probability for a final-state particle to be produced with momentum p' from a neutrino with momentum p impinging on a nucleus and is the term with larger theoretical uncertainties although of crucial importance for the flux extrapolation at the Far Detector.

Precision measurements and nucleon structure investigation

SAND will be able to make a precise measurement of the weak mixing angle $\left(\sin^2\theta_W\right)$ in (anti)neutrino scattering at DUNE energies. A measurement of $\sin^2\theta_W$ can be obtained by the ratio of NC and CC deep inelastic scattering (DIS) neutrino interactions $\mathcal{R}_\nu \equiv \sigma_{NC}/\sigma_{CC}$.
Another independent measurement can be provided studying NC $\nu_\mu e$ elastic scattering and the value of $\sin^2\theta_W$ can be extracted from the ratio $\mathcal{R}_{\nu e} \equiv \sigma\left(\bar{\nu}_\mu e \to \bar{\nu}_\mu e\right)/\sigma\left(\nu_\mu e \to \nu_\mu e\right)$. These two channels will also provide the opportunity to test the running of $\sin^2\theta_W$ as they are characterized by substantially different momentum transfer scales [68].
The availability of large sample of $\nu(\bar{\nu})$ - H interactions allows a precision test of the Adler sum rule[1] $S_A = 0.5\int_0^1 dx/x\left(F_2^{\bar{\nu}p} - F_2^{\nu p}\right) = I_p$ which gives the isospin of the target and , in the quark-parton model, is the difference between the number of valence u and d quarks of the target. The value of the S_A can be measured as a function of the transfer Q^2 from the structure functions $F_2^{\nabla^p}$ and $F_2^{\nu p}$ determined from the corresponding differential cross-section on Hydrogen. This measurement is sensitive to possible variations of the isospin (charge) symmetry, heavy quark production (charm) and strange sea asymmetries $s-\bar{s}$. Furthermore, the measurement from H can be compared with the values

[1] $F_2 = x\left(\frac{4}{9}u(x) + \frac{1}{9}d(x)\right)$ where $x = \frac{Q^2}{2pq}$ with $Q = -q$, q is the momentum transferred by the mediator of the interaction to a parton whose momentum is a fraction x of p total nucleon momentum.

of S_A obtained from the C target for which $S_A = 0$.
From a measurements of the NC elastic scattering off proton $\nu_\mu\,(\overline{\nu_\mu}) + p \rightarrow \nu_\mu\,(\overline{\nu_\mu}) + p$ it is possible to determine the strange quark contribution to the vector and axial-vector currents of the nucleon, as well as to the nucleon spin Δs. Indeed, in the limit $Q^2 \rightarrow 0$ the NC differential cross-section is proportional to the axial-vector form factor $d\sigma/dQ^2 \sim \left(-G_A/2 + G_A^s/2\right)^2$. This provides the most direct measurements of Δs by extrapolating the NC differential cross-section to $Q^2 = 0$ since in this limit $G_A^s \rightarrow \Delta s$. G_A can be experimentally determined by the measure combined measure of $R_{\nu p}\,(Q^2) \equiv \sigma\,(\nu_\mu p \rightarrow \nu_\mu p)\,/\sigma\,(\nu_\mu n \rightarrow \mu^- p)$ and $R_{\bar{\nu} p}\,(Q^2)$ [68].
Due to the possibility of integrating various thin nuclear targets within the STT, SAND will also allow inspection of the nucleon structure disentangling nuclear effects. Using neutrino and antineutrino deep inelastic scattering, the parton distribution functions, cross sections, perturbative and non-perturbative corrections can be studied in a wide range of transverse momentum Q^2 and Bjorken x [68].

3.2 Detector components

3.2.1 Magnet

The SAND system employs an existing superconducting magnet that was successfully operated until March 2018 in the KLOE experiment. The magnet is designed in conjunction with its iron yoke to produce 0.6 T over a 4.3 m long, 4.8 m diameter volume. The coil is operated at a nominal current of 2902 A and the stored energy is 14.32 MJ; it consists of a single conductor layer made of a Nb-Ti composite of Rutherford cable co-extruded with high purity aluminum. The coil is located inside a cryostat with a an outer diameter of 5.76 m, inner diameter of 4.86 m and 4.40 m length, positioned inside the return yoke and the overall cold mass is about 8.5 tons. The mass of the KLOE return yoke is 475 tons.

The cooling of the coil is performed by thermo-siphon cycles: gas Helium at 5.2 K is injected at 3 bar from the cryogenic plant and melted through Joule-Thomson valves into a liquid Helium tank in thermal contact with the coil. The current leads are directly cooled by liquid Helium and the radiation shields are cooled by gas Helium at 70K.

3.2.2 KLOE calorimeter

The KLOE electromagnetic calorimeter [69] is a lead scintillating fiber sampling calorimeter. Scintillating fibers offer high light transmission over several meters, sub-nanosecond timing accuracy, and very good hermeticity. The calorimeter cylindrical barrel (see Fig.

3.2) is located inside the KLOE magnet, close to the coil cryostat. Two calorimeters end-caps ensure hermeticity along the magnet end-caps.

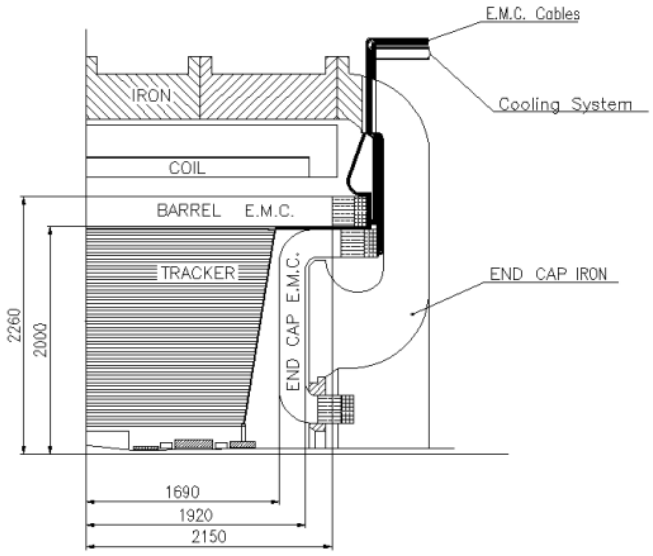

Figure 3.2: Vertical cross section of the KLOE detector.A quarter of the KLOE detector section. The outermost layer is the iron yoke, then the coil, the em. calorimeter and a tracking system in the fiducial volume. Lengths are expressed in mm. [69]

The barrel consists of 24 modules; each module (Fig.3.3.a) is 4.3 m long, 23 cm thick and has a trapezoidal cross section, with bases of 52 and 59 cm. Each end-cap consists of 32 vertical modules from 0.7 to 3.9 m long and 23 cm thick (Fig.3.3.b). Their cross-section is rectangular, of variable width. All modules are stacks of about 200 grooved, 0.5 mm thick, lead foils alternating with 200 layers of cladded 1 mm diameter scintillating fibers. Modules are bent at the upper and lower ends to allow insertion into the barrel calorimeter and also to place the phototube axes parallel to the magnetic field. Due to the large overlap of barrel and end-caps, the KLOE calorimeter has no inactive gap at the interface between those components. The calorimeter weight is approximately 100 tons and the read-out system includes 4880 phototubes.
The energy and time resolution of the calorimeter was evaluated in the KLOE commissioning and operation phases are[69]:

$$\begin{aligned} &\text{spatial resolution in } r-\phi: && 1.3 \text{ cm} \\ &\text{energy resolution:} && \sigma_E/E = \frac{5\%}{\sqrt{E(\text{GeV})}} \\ &\text{time resolution:} && \sigma_t = \frac{40}{\sqrt{E(\text{GeV})}} \text{ ps.} \end{aligned} \tag{3.2}$$

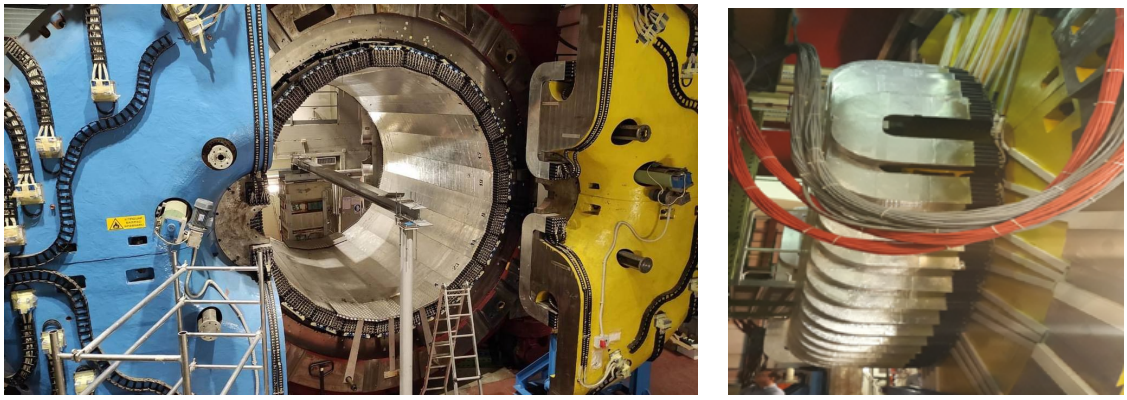

(a) (b)

Figure 3.3: (a) A view of the KLOE calorimeter with 24 trapezoidal cross-section barrels. (b) Calorimeter endcap.

3.2.3 Straw Tube Target Tracker

The Straw Tube Target Tracker (STT) system will act as the target for (anti)neutrino interactions and will provide precise measurement of all charged particle momenta. Moreover, in order to fulfill the physics needs of the long-baseline oscillation analysis, it has:

1. Low density and high track sampling to guarantee high momentum, angular, and spatial resolutions;
2. total thickness comparable to the radiation length to minimize secondary interactions;
3. capability to accommodate various target materials to extrapolate crucial information about neutrino-nucleon interactions;
4. particle identification for $e^{\pm}, \pi^{\pm}, K^{\pm}, p, \mu^{\pm}$;

5. sufficient target mass ($\sim$ 5 tons) to collect enough statistics for flux measurements.

The straw tube technology coupled with target layers offers a unique tool that can fulfill these requirements.The neutrino targets are physically separated from the effective tracking system (the straws), which are of very low mass. Additionally, in order to obtain high-resolution measurements, target mass is evenly distributed throughout the tracking volume, and the average density is low enough for the detector to be transparent to final-state particles generated in neutrino interactions.

The STT tracking system is designed to be a fully modular detector, and each module can be operated and configured independently using different nuclear targets, such as C, Ca, Fe, Pb, etc. The STT module technology is based on low-mass straws that consist of a tungsten wire, with a diameter of 20 μm and 20 nm gold coating, inside tubes with a diameter of 5 mm, mylar walls of 12 μm and Al coating of 70 nm. The tubes are filled with a gas mixture that is Xe/CO_2 70/30 and operated at an internal pressure of approximately 1.9 atm. The single-hit spatial resolution is designed to be less than 200 μm.

The tracking system design is being optimized at the moment of this thesis writing. The latest design makes use of three types of STT modules.

The first type has a polypropylene CH_2 target slab followed by a radiator and four straw layers XXYY, shown in Fig. 3.4. The slab is 5 mm thick and the radiator is made up of 105 polypropilene $(CH_3H_6)_n$ foils 18 μm thick, separated from each other by 117 μm of air gaps. The radiator has a total thickness of 15.95 mm and its configuration is optimized for e/π differentiation exploiting the transition radiation emission. This type of STT module contains a total of 6.89 mm of CH2 which corresponds to about 1.5% of the radiation length.

The second module type (Fig. 3.5.a) is equipped with a graphite (pure C) target in front of four straw layers XXYY assembly. A Carbon target allows for direct measurements of the C background in the selection of Hydrogen interactions in C_3H_6 target.The thickness of the graphite target plate is 4 mm, matching the fraction of X_0 of the target of the first module type. Moreover, to ensure the same detector acceptance for CH_2 and C targets, modules equipped with graphite are interleaved throughout with CH2 modules. The third type, called "tracking module" and shown in Fig. 3.5.b, is the simplest one and is composed of six straw layers XXYYXX glued together.

The complete STT assembly includes 70 modules with CH_2 slabs and radiators, 8 modules with graphite targets and 6 tracking modules. The STT modules fill the magnetic volume, leaving the upstream region for the LAr target, as shown in Fig. 3.1. The tracking modules are placed near the LAr target and in the downstream region, while CH_2 modules, evenly interleaved with graphite ones, fill the inner volume.

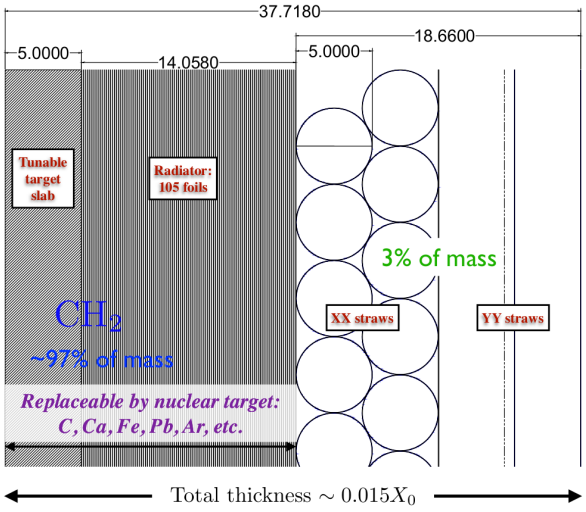

Figure 3.4: Section of the CH_2 module. Lengths are given in mm.

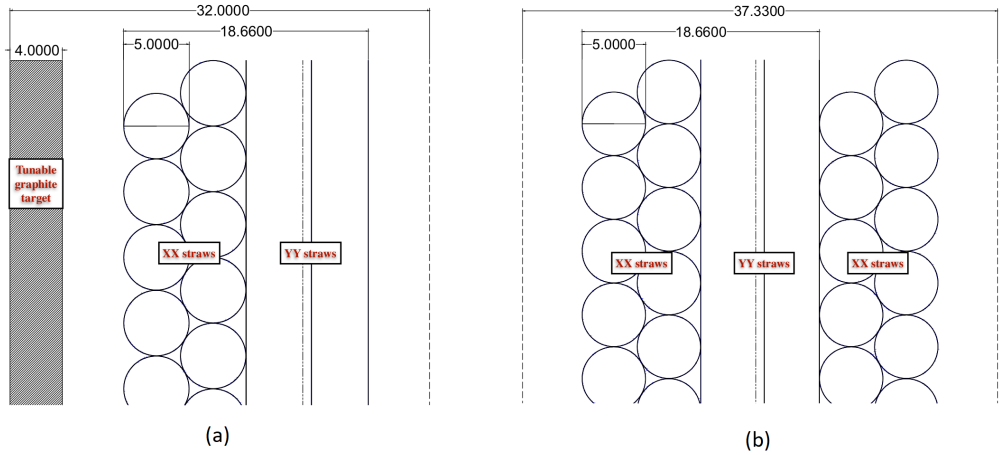

Figure 3.5: (a) Section of the graphite module with the radiator and the CH_2 slab replaced by a graphite target. (b) Section of the tracking module with six straw layers. Distances are in mm.

3.2.4 GRAIN

A ~1 ton liquid Argon active target, GRAIN (GRanular Argon for Interaction of Neutrinos) will be placed upstream in the magnetized volume of SAND. GRAIN will provide inclusive Ar interactions to constrain systematic uncertainties from nuclear effects per-

manently located on-axis for cross-calibration with the other detectors.

The design of the cryostat is being finalized at the time of writing this thesis; it will consist of two coaxial cylindrical-shaped vessels with an ellyptical base, arranged horizontally so that the neutrino beam passes through it along the minor axis of the ellipse (see Fig 3.1). The inner vessel is composed of stainless steel 6 mm thick in the curved walls and 16 mm thick in the endcaps, where flanges are placed to insert the cables of the readout electronics. Its dimensions are 150 cm long, and the axes of the elliptical sides are 145.6 cm and 46.5 cm long, respectively. Inside, the liquid Argon will be kept at 1.5 bar pressure. The dimensions of the outer vessel are 200 cm wide x 190 cm high and 83 cm deep. It is composed of 6 mm thick Carbon fiber and a 4 cm thick honeycomb structure, reinforced with an aluminum alloy along the ellipse profiles. Figure 3.6 shows the lateral projections of the GRAIN geometry with detailed dimensions. A vacuum will be maintained between the inner and outer vessels at a pressure of $10^{-4} - 10^{-5}$ bar to thermally insulate the inner vessel.

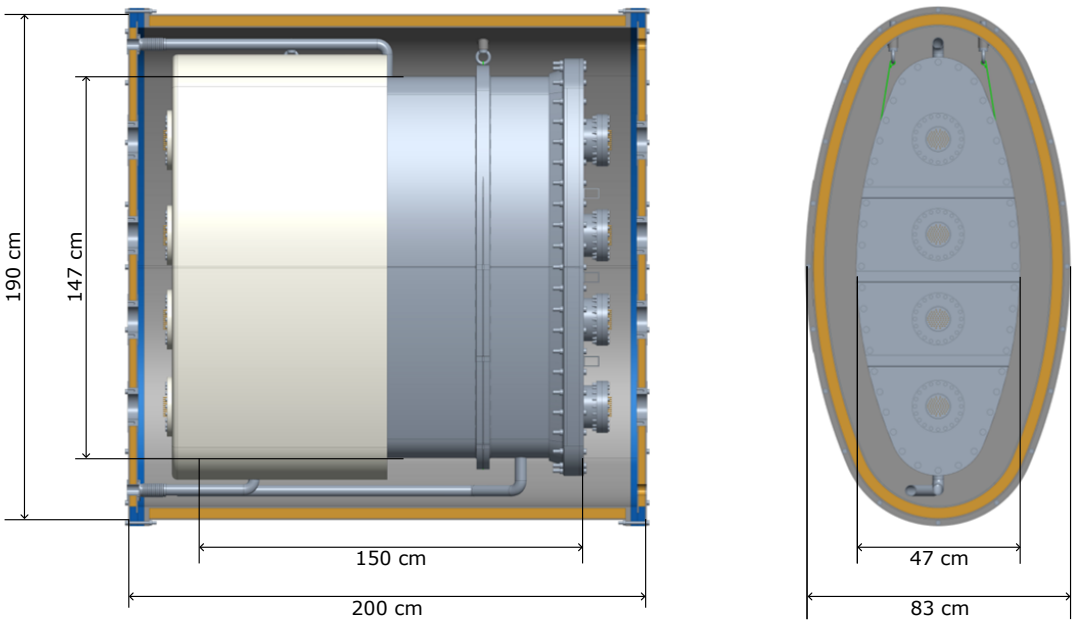

Figure 3.6: GRAIN rendering showing the inner and outer vessel with their dimensions. The inner vessel is made of stainless steel, while the outer vessel is made of carbon fiber and honeycomb in order to minimize the amount of material outside of the target. Between the vessels, a vacuum will be maintained to thermally insulate the inner one.

The design is optimized to minimize the vessel material, resulting in a thickness of a small fraction of radiation length. The overall depth of the LAr volume is kept to a

minimum (1 interaction length) to reduce energy loss, showering, and multiple scattering, as the outgoing particles will be analyzed by the downstream detector elements.
With a LAr target, the established technology for tracking and reconstruction is the TPC. However, as discussed in Section 2.3.3, the construction of a LArTPC at the ND is non-trivial. In fact, the number of events and pile-up is very high and cannot be managed with a traditional TPC because the drift time of the ionization charges is on the order of milliseconds. One possible solution is to resort to a design like the one developed for ND-Lar and build arrays of several small LArTPCs. An alternative R&D program is underway to develop a novel tracking and calorimetry system entirely based on the imaging of LAr scintillation light.
The idea behind this imaging system is analogous to that of bubble chambers. In a bubble chamber charged particles passing through a superheated liquid deposit some of their ionization-inducing energy. Along the particle trajectories the liquid vaporizes, forming microscopic bubbles. Several photographic cameras are mounted around the chamber, allowing images of an event to be captured, which can be combined to form a three-dimensional image. Similarly, when charged particles cross the Liquid Argon, in addition to ionization, part of their deposited energy generates excites Ar atoms inducing photon emission. By placing pixel-segmented photon detectors (our "cameras") on the inner walls of the cryostat and immersed in the Argon itself, it is possible to "take a picture" of the emitted scintillation light. The idea is simple, but to the best of our knowledge has never been attempted before. The development of focusing optics for photons of the wavelength of argon scintillation photons (127 nm) and capable of operating in the cryogenic environment, presents significant challenges. In addition, the availability of suitable light sensors for this purpose is rather new.
In the next sections, we will discuss how LAr scintillation light can to be used for imaging with proper precautions. Two technologies are being evaluated at the moment, one based on lenses and another on coded aperture imaging. In this dissertation we will show the development of an imaging system based on coded aperture cameras, calorimetry studies exploiting the same camera system are the subject of another thesis work [70].

LAr properties

Liquid Argon is used as active medium in a variety of neutrino and Dark Matter experiments thanks to its excellent properties of charge yield and transport and as a scintillator.

Liquid Argon scintillation photons are emitted with a characteristic time profile made up of two components that originate from the decay of the lowest-lying singlet state, $^1\Sigma_u^+$, and the triplet states, $^3\Sigma_u^+$, of the excimer Ar_2^* to the dissociative ground state. Both states decay radiatively, emitting a photon of approximately 9.7 eV, but with very

different lifetimes: 7 ns for the singlet state and 1.6 μs for the triplet one. For this reason, the singlet and triplet components are generally referred to as fast and slow components, respectively. The relative abundance of the two components strongly depends on the type of ionizing particle and allows powerful particle discrimination, as shown in Fig. 3.7. In contrast the total number of emitted photons and photon wavelength do not depend on the component: the number of emitted photons depends on the total energy deposited by the ionizing particle, with a typical light yield of around 40k photons per MeV of deposited energy.

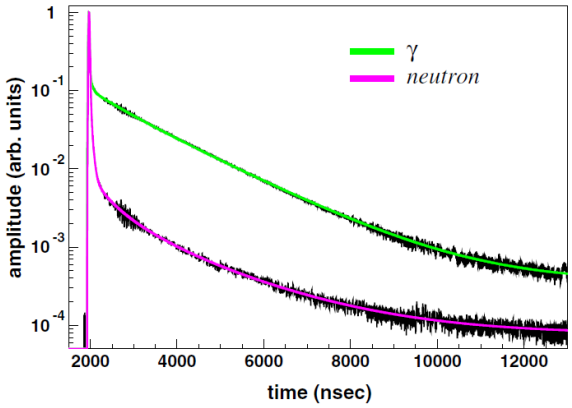

Figure 3.7: Signal shape of liquid Argon scintillation light for gammas (green) and neutrons (pink). The two scintillation components are clearly visible in both cases, with the sharp peak being generated by the fast component, and the long tails being generated by the slow component. [71]

The wavelength of the scintillation photons has been measured multiple times by different authors [71, 72, 73] and all of the measurements agree with a value around 127 nm, in the VUV range. Fig. 3.8 shows a measurement of the scintillation spectrum of liquid Argon compared to the emission spectra of gaseous Argon.

Pure LAr has a high light yield and is transparent to its own scintillation light, but impurities can dramatically affect these properties by quenching and absorption processes. Quenching leads to a significant reduction of Ar_2^+ molecules by nonradiative decay in two-body collisions with impurity molecules such as N_2 and O_2. In the case of oxygen, the absorption of scintillation photons leads to atomic metastable states, whose excitation energy is usually converted into heat.
According to [74], the dependence of the absorption length with the concentration of nitrogen contaminants is as follows:

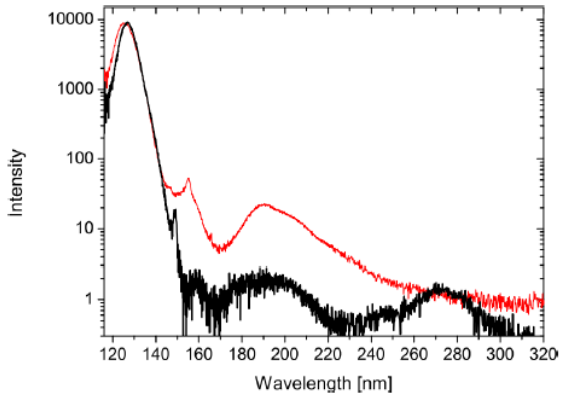

Figure 3.8: Liquid Argon emission spectrum (black line) compared with the emission spectrum of gaseous Argon (red line). The emission for liquid Argon is dominated by a 127 nm feature, with a peak at 149 nm caused by xenon impurities and much smaller contributions up to about 300 nm[72].

$$\lambda_{Abs} = \frac{66.4}{[\mathrm{N_2}](\mathrm{ppmv})}\mathrm{m} \tag{3.3}$$

where $[N_2]$ is measured in parts-per-million in volume. An absorption length of $\lambda_{Abs} = 5$ m, which is taken as a reference in these studies, corresponds to an equivalent concentration of $[N_2] \sim 13$ ppmv.

Scintillation photons emitted by Argon can interact only via Rayleigh scattering in the bulk, as the first ionization potential of Argon is 15.7 eV. This process does not directly reduce the total light yield, but changes the direction of the photons, increasing the propagation length and, consequently, the absorption probability.
The latest experimental measurements, which estimate the group velocity of the scintillation light of cosmic muons in liquid Argon, result in an estimate of $\lambda_{RS} = 99.1 \pm 2.3$ cm [75]. As the scattering length depends on the inverse of the fourth power of the photons wavelength, it is possible to increase the length by means of a wavelength shifter. This is the case for a mixture of Argon doped with a small amount of Xenon. Measurement results in Xenon-doped liquid Argon suggest an increase of the scattering length, up to about several meters [76].

Given the attenuation length of the order of several meters with due control of impurities and the high number of scintillation photons, LAr is well suited for the realization of a small imaging and calorimetry system such as GRAIN. In particular, the fast emission of the singlet component allows for a response time of a few tens of nanoseconds,

suitable for use with the expected event rate at the Near Detector. However, a Rayleigh scattering length of the order of a meter can affect imaging at GRAIN scale, and it is necessary to take this into account in the system design to mitigate its effects. The application of Xe doping in GRAIN to reduce the scattering length and increase the light collection due to an improved detection efficiency is still under investigation. In this thesis, the studies presented were performed with the target without doping.

Imaging systems

The design of an imaging system that can be operated in LAr with sufficient spatial resolution (< 1 cm) and fast timing response faces significant challenges:

- conventional lenses have poor transmissivity to vacuum ultra-violet light, so novel solutions are required;
- mirror-based optics occupy a large portion of GRAIN volume, reducing available fiducial volume;
- for such an optical system to be capable of providing an adequate resolution, it must collect enough light and the photosensors must be (finely) segmented;
- The sensors and readout electronics must be able to operate in cryogenic condition, with single-photon detection capabilities, and sufficient bandwidth to resolve multiple interactions in one spill.

In this thesis, matrices of Silicon Photomultipliers (SiPMs) are be used as photosensors. SiPMs are robust sensors sensitive to single photons: commercial models already exist that can to operate in cryogenic environment and benefit of a significant dark noise reduction at low temperatures. Moreover, a matrix of closely packed pixels can offer a relatively high resolution in the reconstruction. Shown in Fig. 3.9 are two SiPM matrices mounted on PCBs used to build an initial 256-channel prototype. The optical system will be mounted on the array with a mechanical coupling that can accomodate various types of masks and lenses.

The SiPMs main drawback is their poor sensitivity to the wavelength of the Argon scintillation light. This requires the use of a wavelength-shifter (WLS) coating to convert UV light into visible light, where these sensors have their optimal photon detection efficiency (PDE). Tetraphenylbutadiene (TPB) is an organic compound that fluoresces when excited by UV radiation. Its fluorescence spectrum is peaked at about 430 nm [77] matching the SiPM PDE spectrum (see Fig. 3.10 for Hamamatsu S14161 model) and does not vary with the wavelength of incident light in the UV range. However, the

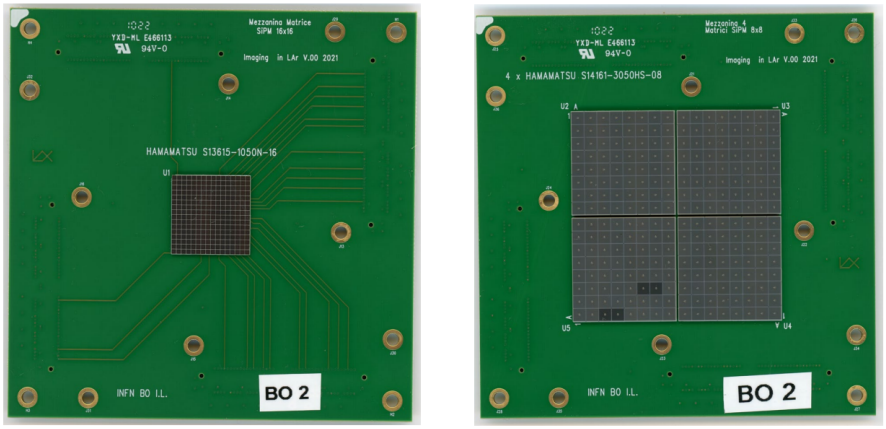

Figure 3.9: SiPM matrices used to build a 256-channel prototype. Left: Hamamatsu S13615 series 16×16 matrix, with a SiPM area of 1 mm^2. Right: 4 8×8 matrix of Hamamatsu S14161 with 9 mm^2 area placed next to each other to form a 16×16 matrix.

emission of fluorescence light is isotropic, so half of the photons reaching the SiPM are emitted back in the detector volume. These effects were taken into account in the Monte Carlo simulations by assuming a PDE of 25%.

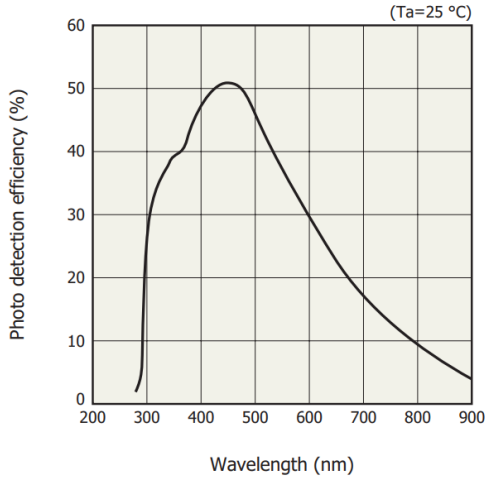

Figure 3.10: Photon detection efficiency vs wavelength of incident light of SiPM model Hamamatsu S14160 series [78]. The peak PDE corresponds to a wavelength of $\sim$ 450 nm.

Readout electronics to determine the timing of photon arrival and the number of

photons will be placed directly in Argon, connected to the back of the camera. Possible ASIC architectures under study are described in Sect. 5.2.4
As mentioned above, one of the technological solutions under investigation is a lens-based imaging system. This focusing optics consists of two plano-convex lenses of high purity non-crystalline fused silica glasses, transparent to VUV photons, separated by a nitrogen-containing volume between them. The lens design is optimized to operate with Argon scintillation light doped with Xenon at 175 nm, it provides optimal focus between 35 and 80 cm. In simulations, a camera is 5 cm in diameter by 10 cm depth, coupled with a 1024-pixel SiPM array with 2×2 mm^2 area. A possible arrangement of 38 lens cameras within GRAIN is shown in Figure 3.11. Studies on the optimization of this optical system are still in progress and will not be described further in this thesis.

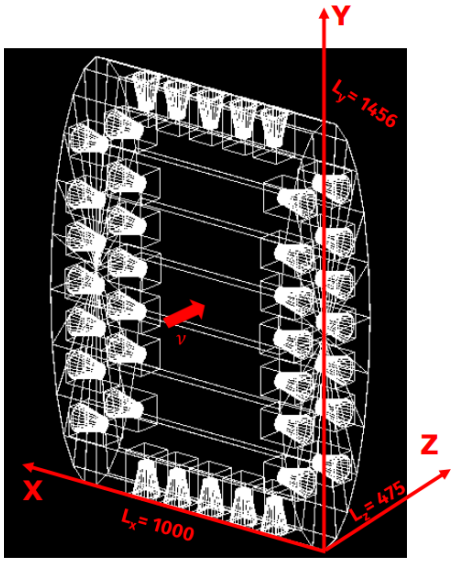

Figure 3.11: Example placement of the cameras of the lens-based imaging system inside GRAIN.

As already introduced, the approach on which this thesis is based on is one already well known in X-ray and gamma-ray astronomy but never used so far in particle physics experiments: the Coded Aperture Mask technique. In such an optical detection system (Fig. 3.12), the scintillation light signal is filtered by coded aperture masks, slabs of opaque material with a certain number of holes, placed at a fixed distance in front of the photosensor.

The advantage of using coded aperture masks is that they require no special materials and are simple to construct. The pattern and size of the mask can be optimized to create

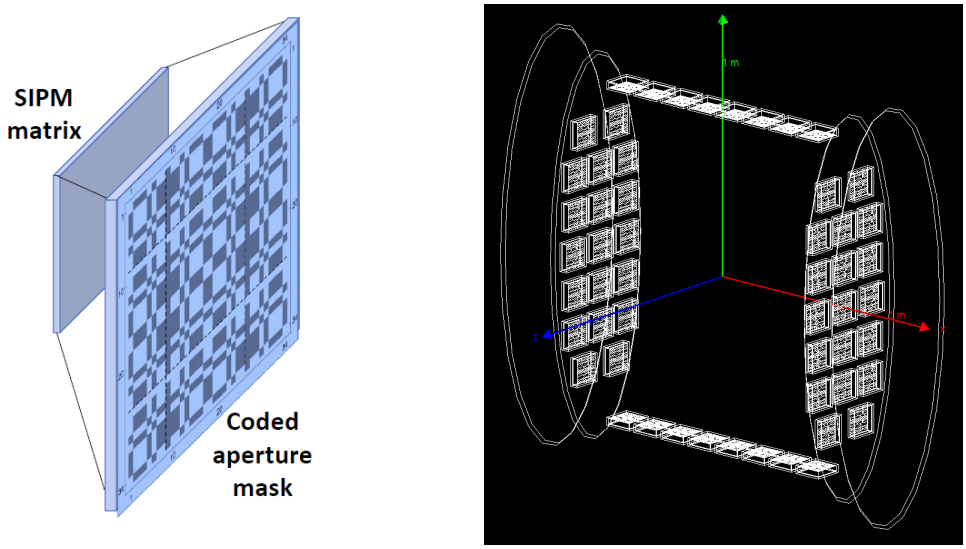

Figure 3.12: Left: Schematic diagram of a coded aperture camera. The mask is perforated, and liquid Argon fills the volume between the SiPMs and the mask, while the side walls are closed and of opaque material so that the incident light flux is *fully coded* by the mask pattern. Right: example placement of coded aperture cameras in GRAIN.

a compact system, 2-5 cm thick, with a wide field of view. On the other hand, image reconstruction is non-trivial, as the image formed on the sensor turns out to be the convolution of images from each aperture, as in a pinhole camera. The next chapters of this thesis will show the development of a three-dimensional reconstruction method for coded aperture cameras and the definition of a camera design optimized for the GRAIN geometry and its requirements.

Chapter 4

Coded Aperture Imaging

This chapter will outline the principles behind the optical properties of Coded Aperture Masks, presenting a number of their potential designs and an overview of the most used reconstruction methods.

4.1 Basic concepts of coded aperture imaging

The coded aperture concept was introduced independently by Dicke [79] and Ables [80] in 1968 as an extension of the pinhole camera. A single pinhole camera is composed of an opaque material that separates the detector plane from the emitting source and a single pinhole that allows light or radiation to pass through. The pinhole camera has the ability to deliver excellent angular resolution, but it is inefficient owing to count loss caused by the opaque material.

Coded aperture imaging (CAI) was developed to preserve angular resolution while improving efficiency. Rather than using an attenuating plane with a single pinhole, a mask consisting of an array of opaque and transparent elements is set between the source fluxes and a position-sensitive detection plane. The transparent and opaque elements, shortly "mask cells", all have equal size and are distributed in a predetermined pattern, which is placed on a regular grid. The shape of a mask element may be arbitrary.
Every source, or source element, within the field of view projects a shadow of the aperture onto the detection plane. For a single point source the detected two-dimensional distribution of events reproduces a mask pattern, or part of one, but is shifted relative to the central position over a distance uniquely correspondent to the direction of the photons. For a more complex source or arrangement of point sources, the recorded shadow is the sum of many such distributions. Fig. 4.1 shows a schematic for a pinhole and a coded aperture camera.

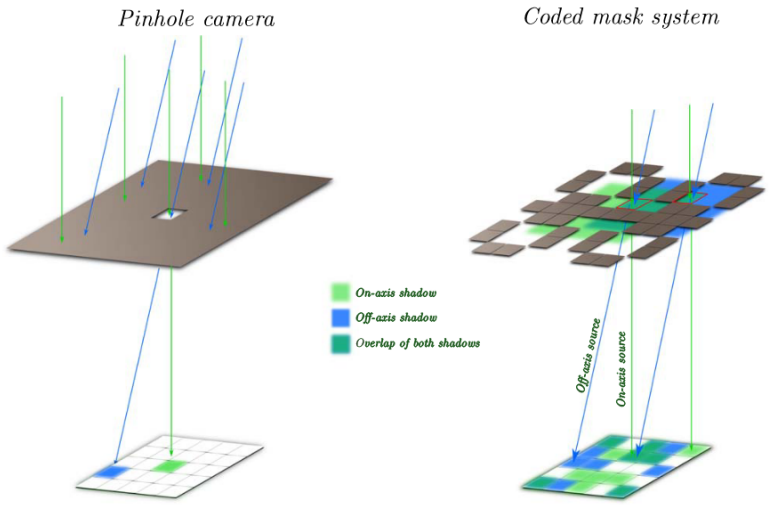

Figure 4.1: Left: a pinhole camera. The detector plane registers an image of the source field with relatively low significance peaks, since the detecting area corresponds to only one mask element. Right: a coded aperture mask camera. The detector plane registers an overlapping set of multiple images, each set associated with one point source.

4.1.1 Image formation with a mask

Assuming a two-dimensional object, we denote by $S(x, y)$ its distribution and by $A(x, y)$ the aperture transmission function. The spatial distribution of the detected flux is mathematically described by [81]:

$$D(x, y) = A(x, y) * S(x, y), \tag{4.1}$$

where $*$ is the convolution operator. Subsequently, an estimate $\tilde{S}$ of the object S can be obtained by filtering the detected flux D with a suitable decoding function $G(x, y)$:

$$\tilde{S}(x, y) = D \otimes G = S * (A \otimes G) \tag{4.2}$$

where $\otimes$ is the correlation operator. The quality of the object reconstruction therefore depends on the choice of the aperture $A(x, y)$ and the decoding function G. If G can be chosen so that:

$$A \otimes G = \delta \tag{4.3}$$

in this case equation 4.2 can be reduced to the convolution:

$$\tilde{S} = S * \delta = S \tag{4.4}$$

and the reconstructed image will represent the object.
The addition of a noise term N to the detected flux $D = A * S + N$ does not significantly change the derivation, leading, for the same choice of G as in the previous equation, to:

$$\tilde{S} = S * \delta = S + N \otimes G. \tag{4.5}$$

The imaging quality of the camera is determined by the type of mask pattern, the optical design of the camera, the spatial response of the detector, and the reconstruction method. These items will be discussed in the following sections.

4.2 Mask patterns

In general, the open fraction f (the number of open mask cells over the total number of cells, or the open area over the total area of the basic pattern) must be large enough ($f \geqslant 0.3$) to provide high throughput. However, it cannot be too large, since in this case the number of "dark" regions on the detector for a given source will be too small and the measurement of the background against which the source signal will be evaluated will be statistically poor, degrading the S/N of the reconstructed image. Therefore, an open fraction close to 1/2 is in most applications a desirable property of the basic pattern.

For the mask imaging quality, the point spread function (PSF) can be used to quantify the ability of a combination of coding (A) and decoding (G) to reconstruct a δ function, and therefore its ability to accurately reconstruct a source. The PSF is defined to be the reconstructed object of a perfectly centered point source placed infinitely far away, and can be constructed through the cross-correlation:

$$PSF = A * G \tag{4.6}$$

without the need for simulation or experiment to produce D for the point source. This will generate a reconstructed image based solely on the efficiency of the decoding process.

As will be explained in Section 3.4, the most direct way to choose the decoding function G is to use the coding matrix itself. In this case, the PSF is equivalent to the auto-correlation of the coded aperture array.

To summarize, for ideal imaging qualities, one would want the mask pattern to satisfy the following conditions:

- the auto-correlation function of the mask pattern should be as similar as possible to a delta function;

- the signal-to-noise ratio of a coded (point) source should be optimum.

The question of a suitable mask pattern for CAI instruments has been studied in detail by many authors; see, for example, [82] for a review. The following sections will be focused on the description of the patterns that were actually tested as possible options for GRAIN cameras, namely random patterns and Modified Uniformly Redundant Arrays.

4.2.1 Random array

As mentioned earlier in this chapter, the random pinhole pattern was proposed as an extension of a pinhole camera. The pinhole camera has ideal imaging properties with respect to the first condition, but it delivers a poor signal-to-noise ratio, since the sensitive area is severely restricted by the size of the pinhole. One option to improve efficiency is to increase the aperture hole size, but at the expense of angular resolution. The idea behind the random pinhole camera is to increase the open area of the plate while preserving the angular resolution by placing many duplicate pinholes at random in the plate.

Random patterns do not place any constraint on the dimensions of the aperture or its overall transparency. Although the random character is necessary to meet the first condition as closely as possible, its auto-correlation function consists of a large central peak surrounded by pronounced sidelobes structures. Imaging of many point sources or of extended sources can cause these sidelobes to produce spurious peaks in the background, or if matrix inversion decoding is employed noise amplification may occur. For this reason, random arrays do not provide ideal imaging properties. This does not necessarily mean that random arrays cannot be used without significantly degrading image quality. First, the value of any point in the sidelobes is a sample from the same probabilistic distribution: this means that, on the average, the sidelobes are flat. Furthermore, since neighbor cells are not correlated, the sidelobes do not show recognizable structures. The effect is that of adding a noisy background, even for an infinite number of counts, but not artifacts. For this reason, this noise is sometimes called “inherent noise”, because it is “built in” the mask.

Figure 4.2 shows the autocorrelation function of two random patterns with equal dimensions and the same open fraction, but with different inherent noise structures.

Later work focused on finding patterns that do have flat side-lobes. Ideal patterns were found that are based on cyclic difference sets[83].

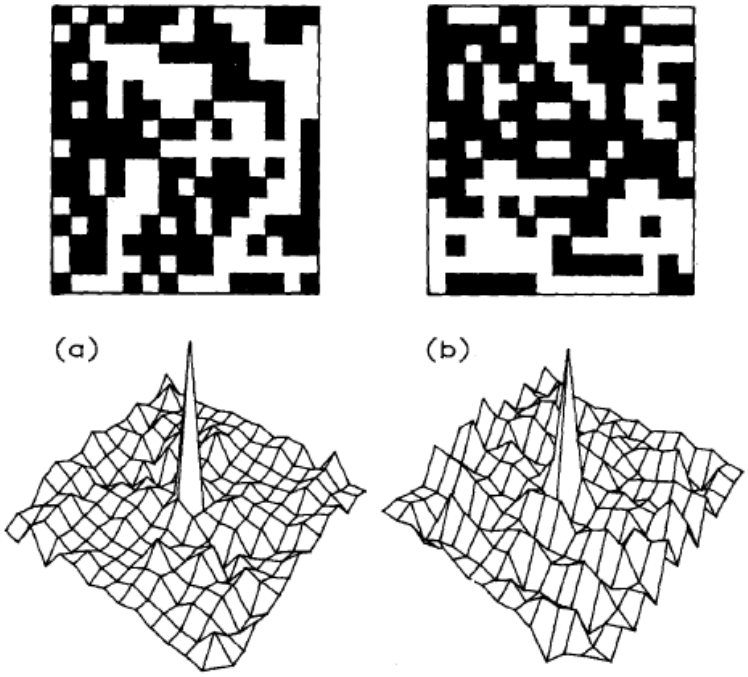

Figure 4.2: Two 15×15 random masks of 50% transparency. Their different inherent noise characteristics are reflected in their different autocorrelantion functions (below).

4.2.2 URA

A class of widely used patterns comprises the so-called Uniformly Redundant Arrays (URAs) proposed by Fenimore and Cannon [84]. They are "uniformly redundant" in the sense that the number of pairs of holes with a given separation in the pattern is the same for all possible separations.
A two-dimensional URA is a rectangular pattern built with so-called twin-prime numbers (primes separated by 2). The URAs have an open fraction of about 1/2 and possess the desirable property of never repeating themselves in any permutation.
The PSF for a URA can be seen in Figure 4.3, with a δ spike with no noise on its bounds. This is the first array to satisfy the first criterion mentioned beforehand, and theoretically produce reconstructions of a source without the presence of decoding artifacts.

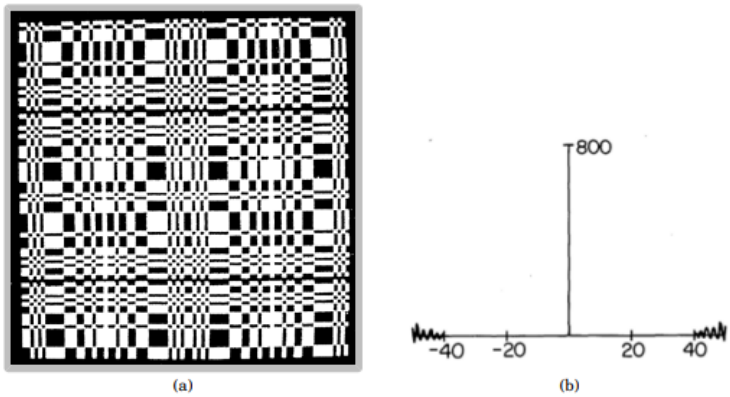

Figure 4.3: : The (a) aperture and (b) cross section of the PSF for a URA coded aperture, of 43×41 elements. The URA has been repeated in a 2x2 pattern.

4.2.3 MURA

An interesting modification (the Modified URAs or MURAs) was introduced by Gottesman and Fenimore [85]. They discovered that a slight change in the G decoding function allows the use of square patterns with any prime number p, on a $p \times p$ array. The MURAs have the exact same properties as the URAs and provide a much wider choice of patterns to instrument design.

Fig. 4.4 shows a 17 × 17 MURA mask. The pattern can be expressed by a binary matrix, where a "1" denotes a pinhole and a "0" opaque material:

$$H_{ij} = \begin{cases} 1 \text{ if } i + j = 0 \\ 1 \text{ if } j = 0, i \neq 0 \\ 1 \text{ if } C_i C_j = 1 \\ 0 \text{ otherwise} \end{cases} \tag{4.7}$$

with

$$C_k = \begin{cases} +1 \text{ if k is a quadratic residue modulo } p, \\ -1 \text{ otherwise} \end{cases} \tag{4.8}$$

and zero-based indices i and j referring to rows and columns. MURA masks also reach a fraction of opaque to transparent cells of approximately 50%. For a squared mask with sides of p pixels, the number of open elements is indeed found to be:

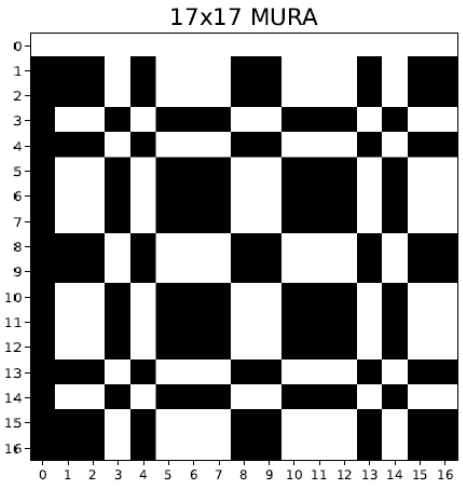

Figure 4.4: A 17×17 MURA mask. The darkened regions represent the closed mask elements.

$$N_{\text{open}} = \frac{p^2 - 1}{2} = \frac{N_{\text{total}} - 1}{2} \tag{4.9}$$

A decoding function G for a MURA pattern A_{ij} can be constructed as follows:

$$G_{ij} = \begin{cases} +1 \text{ if } i + j = 0 \\ +1 \text{ if } A_{ij} = 1, \ (i + j \neq 0) \\ -1 \text{ if } A_{ij} = 0, \ (i + j \neq 0) \end{cases} \tag{4.10}$$

When the statistical fluctuations in the reconstructed image are large compared to the intrinsic noise of the pattern, the no-artifact property becomes less relevant. Random patterns with $f \simeq 1/2$ have been used with good performance in several instruments, especially when the number of elements in the pattern is large and imaging in the Partially Coded Field of View (PCFV, see Sect. 4.3.1) is important. In applications in which the number of mask elements needs to be small (for example in gamma rays astronomy), it is important that the autocorrelation function of the pattern approaches a delta function so that the reconstructed image has no artifacts.

4.3 Optical design

The optical design of a coded-mask camera is defined by the sizes of the mask, the mask elements and the detector, the number of basic patterns used in the mask, the distance between mask and detector and the size and place of an optional collimator. Apart from the imaging quality, the design determines the resolution and the Field of View (FoV).

4.3.1 Box and Mosaic configurations

For any particular camera geometry the field of view consists of two distinct regions, as shown in Fig. 4.5: the Fully Coded Field of View (FCFV) which is defined as comprising all directions for which the detected flux is completely modulated by the mask, and the Partially Coded Field of View (PCFV) in which only a fraction of the detected photons is coded by the aperture pattern.

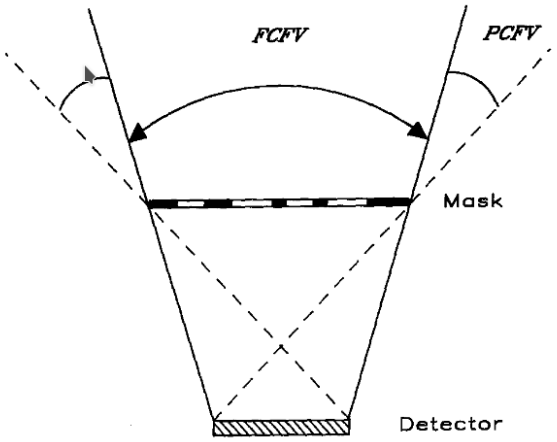

Figure 4.5: The Fully Coded Field of View (FCFV) is defined as comprising all directions for which the recorded flux is completely modulated by the mask. The Partially Coded Field of View (PCFV) is defined as comprising all the directions for which only a fraction of the detected flux is coded by the mask. The FCFV and the PCFV are shown for a geometrical configuration having the mask larger than the detector.

It is clear from the decoding procedure shown in Eq. 4.2 that ideal imaging properties are possible only if complete mask patterns are projected on the detector.
The simplest arrangement is to have the mask and detector of the same size. However, this configuration suffers from the fact that the entire FoV, except from the on-axis direction, is only partially coded. In order to increase the FCFV, a larger detector is

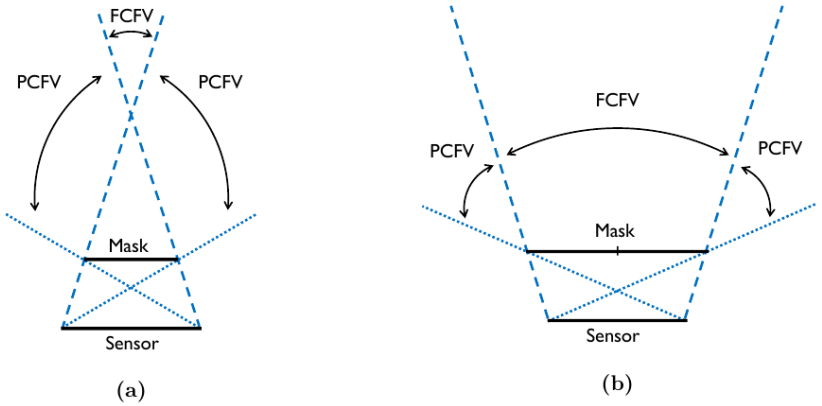

Figure 4.6: FCFV and PCFV regions for a box and mosaic configuration

a possible solution, but seldom the most practical, as fabrication issues or cost can set a limit on the detector size. In these cases it is more convenient to instead enlarge the mask by replicating it in a 2×2 arrangement called "mosaic" . With this arrangement all sources within the FCFV still project an entire mask pattern on the detector, as the pattern is periodic, but the pattern shifts are different depending on the source position, as Fig. 4.6.b shows.

The above type of mask-detector has optimum imaging capabilities. An alternative configuration is the "box" system, in which the requirement for full coding is relaxed. In a box system, only the on-axis position is coded with the full basic pattern, the remainder of the FOV is partially coded. Obviously, off-axis sources will cause false peaks in the reconstruction. However, as will be discussed later on, this coding noise can be eliminated to a large extent recurring to different reconstruction processes, such as Wiener filtering or the Maximum likelihood method, which will be illustrated in the remainder of this chapter.

4.3.2 Field of View and resolution

The two main parameters for Coded Aperture cameras are the FoV and the geometric resolution, i.e. the resolution due to its geometric design, assuming the detector to be ideal. As for simple pinholes, these two quantities are strictly related to each other and to the parameters of the detector.

For a single period mask camera, in the so-called near field configuration, a source at a finite distance will be projected according to the magnification coefficient:

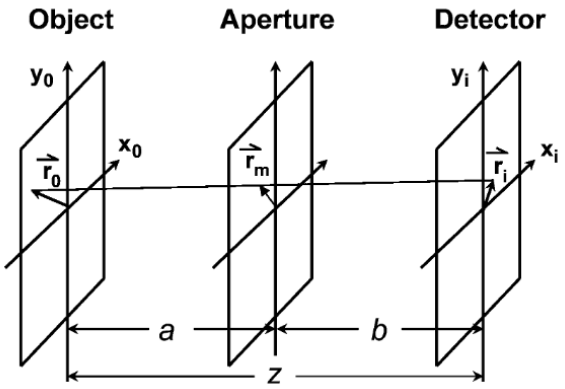

Figure 4.7: Coordinate scheme of a coded aperture camera.

$$m = 1 + b/a \tag{4.11}$$

where a is the object-to-mask distance and b the mask-to-detector distance as shown in Fig. 4.7. If the mask size is d_m and $d_d > d_m$ is the detector size, the projection will have a size md_m, leaving a space $(d_d - d_m)/2$ on both sides of the detector to shift the mask. This corresponds to a field of view:

$$FoV = \frac{d_d - md_m}{m-1} = \frac{d_d}{m-1} - \frac{md_m}{m-1}. \tag{4.12}$$

In the case of a periodic 2×2 mosaic, only one of the four copies of the basic pattern covers the detector completely, leading to a field of view

$$FoV = d_d \cdot \frac{a}{b} = \frac{d_d}{m-1} \tag{4.13}$$

which can be easily seen to be larger than the FoV of a non-periodic arrangement for a given d_d.

The resolution of an imager is defined as the minimum distance between two point sources so that their image is still perceived as two separate points. For a Coded Aperture system this definition translates to the distance that two sources must have for their projections to be a projection of a mask hole apart. This spacing λ_g is found to be:

$$\lambda_g = \frac{mp_m}{b} \cdot a = \frac{m}{m-1} \cdot p_m \tag{4.14}$$

where p_m is the size of a mask hole. A relation between FoV and resolution can thus be derived :

$$\frac{FoV}{\lambda_g} = \frac{d_d}{mp_m}. \tag{4.15}$$

Finally, combining the previous equations, the effect of the detector dimension on the geometric resolution is found to be determined by:

$$\lambda_g = p_m \cdot (1 + \frac{FoV}{d_d}) \tag{4.16}$$

which implies that a large detector allows better resolution for a given FoV.

4.3.3 Depth of Focus

For lenses, the distance range at which objects can be focused sharply, called Depth of Focus (DoF), is defined by the focal length. Coded Aperture optical systems, on the other hand, do not focus light and in theory should produce collimated images at infinity. This would enable the focusing of tracks at any distance, greatly simplifying the reconstruction. In reality, the sharpness of Coded Aperture images is constrained by the sampling artifacts emerging when the shadow of a mask element is projected over a non-integer number of pixels, which act as a limiting factor for the collimation. This allows to define a concept of focusing in analogy to lenses.

The aforementioned number of pixels α is given by

$$\alpha = \frac{mp_m}{p_d} = \frac{(1 + b/a)p_m}{p_d} \tag{4.17}$$

so that the camera configurations for which focusing is possible are those close to $\alpha = 1$, with successive αs identifying increasing in-focus magnifications. The size of the DoF is thus defined by the derivative:

$$\frac{d\alpha}{da} = -\frac{p_m b}{p_d a^2}, \tag{4.18}$$

so that, as typically $p_m \simeq p_d$, cameras that focus ($\alpha = 1$) at large distances have very small variations of α with a, i.e. a nearly infinite DoF, while configurations with a small focusing distance will have a really small DoF [86].

4.4 Reconstruction techniques

Coded-mask imaging is basically a two-step procedure. After the accumulation of spatially coded detector data, the second step involves its decoding or the reconstruction of the observed emission distribution. Several methods have been developed in the past decades, and the choice for a certain algorithm depends on the specific aim, the available computation power, and the type of instrument configuration. Several types of algorithm may, in fact, be subsequently used on the same set of detector data. This section reviews the algorithms most used in literature, with particular focus on the Maximum Likelihood Expectation Maximization algorithms, which will be adapted and used in this thesis.

4.4.1 Direct deconvolution methods

A first method of decoding is suggested by Eq.4.2 itself. The choice of the decoding matrix G must be such that $G * A$ is as close as possible to a delta function. One method is to use the array A itself as the decoding matrix.
Other forms of this algorithm are based on a decoding array derived from A, for example, in the following manner [81]:

$$G_{jk} = \begin{cases} 1 \text{ if } A_{jk} = 1, \\ -\tau/(\tau - 1) \text{ if } A_{jk} = 0 \end{cases} \tag{4.19}$$

where τ is the overall transparency of the basic mask pattern, defined as the ratio of the number of the transparent elements of the mask over the total number of elements.

Another straightforward way to perform the image reconstruction is using the Fourier transform, which reduces a convolution of Eq. 4.2 to a simple multiplication.
Provided the Fourier transform of each function exists, the estimate $\tilde{S}$ is given by:

$$\tilde{S} = F^{-1}(F(D)/F(A)) = S + F^{-1}(F(B)/F(A)) \tag{4.20}$$

where F and F^{-1} are the Fourier transform operator and its inverse, respectively.
In practice, however, the implementation of this technique using discrete Fourier transform algorithms can produce noise amplification due to small values in F(A). In this case, the distortion and deterioration of the reconstructed image can become dramatic even in relatively high signal-to-noise ratio situations.

4.4.2 Wiener filtering

The Wiener Filter was introduced for use as a reconstruction method as an extension of the direct deconvolution method in the Fourier space by Willingale et al. [87]. This

method can be regarded as a weighted cross-correlation [88], where the Fourier transform components of the detector image are weighted with the inverse power density of the mask pattern. In this way, fluctuations of the modulation of the transfer function of the mask pattern are smoothed, under the assumption the system is linear and the noise term is a Gaussian white noise. In the Fourier domain with ν as the frequency vector, the Wiener filter reads as follows:

$$w(\nu) = \frac{1}{A(\nu)} \frac{|A_\nu|^2}{|A_\nu|^2 + \frac{1}{\mathrm{SNR}(\nu)}} \tag{4.21}$$

This reconstruction method turns into a multiplication in the Fourier space and thus offers fast reconstruction. However, as the Signal-to-Noise Ratio (SNR) is not known before the reconstruction, it must be estimated, or a frequency-independent expression needs to be used for it.

4.4.3 Photon tagging

Photon tagging (or URA-tagging) was introduced by Fenimore [89]. It involves back-projecting every detected photon through the mask, towards all positions within the camera FoV from which it could originate. If a closed mask element is encountered in the back-projection, the photon is accumulated in the background contribution. If it instead encounters an open mask element, it accumulates in the source contribution for that position in the sky. Once all photons have been processed, the subtraction of the background from the source contributions (after proper normalization) completes the reconstruction. It is clear that this method is advantageous relative to a cross-correlation, in terms of computation time, only if the number of detected photons is very small with respect to the number of mask elements.

Skinner and Nottingham [90] improved the method by extending it, taking into account imperfections of the detector (limited spatial resolution, 'dead spots', etc.), the support grid of the mask plate, and telescope motion in astronomic observations.

4.4.4 Maximum Likelihood Expectation Maximization Algorithm

The methods presented in the previous paragraphs all are dependent on the geometry configuration of the coded aperture camera, but do not consider any information on the physics processes involved in the photon emission or detection, which is intrinsically stochastic.

A separate class of reconstruction methods is formed by iterative methods. These try to

reconstruct the source distribution by an iterative search for the solution that is most consistent with the detector data. Various methods for use in coded mask imaging have been investigated, such as the Maximum Entropy Method [87], Least-Squares estimator [91] and Maximum Likelihood Expectation Maximization (ML-EM)[87].

In the ML-EM algorithm, the measured data are considered samples from a set of random variables whose probability density functions are related to the object distribution according to a mathematical model of the data acquisition process. Using the mathematical model, it is possible to calculate the probability that any initial distribution density in the object under study could have produced the observed data. In the set of all possible images, which represent a potential object distribution, the image having the highest such probability is the *maximum likelihood estimate* of the original object. The algorithm can be directly extended to a three-dimensional reconstruction.

Derivation of the ML-EM algorithm

The mathematical model is based on the assumption that the emissions occur according to a spatial Poisson process in the region of interest of the source.
Let $H(s)$, $s = 1, 2..., S$ be the measured number of photons hits in the sensor matrix pixel s. This follows a Poisson distribution and can be expressed as [92]:

$$f(H(s)|\Lambda(d)) = e^{-\Lambda(s)} \frac{\Lambda(s)^{H(s)}}{H(s)!} \tag{4.22}$$

where

$$\Lambda(s) = \sum_{j=1}^{J} \lambda(j) p(j, s) \tag{4.23}$$

is the expectation of H(s), and $\lambda(j)$ represents the unknown photon counts of voxel j of the segmented volume of interest to be estimated from the measured data. The probability matrix $p(j, s)$, named *system matrix*, is the probability that an emission in voxel j is detected in sensor pixel s. The likelihood associated with the observed data is as follows:

$$L(\boldsymbol{\lambda}) = \prod_{s=1,...,S} e^{-\Lambda(s)} \frac{\Lambda(s)^{H(s)}}{H(s)!} \tag{4.24}$$

If $l(\boldsymbol{\lambda}) = lnL(\boldsymbol{\lambda})$ then

$$l(\boldsymbol{\lambda}) = \sum_{s=1}^{S}[-\Lambda(s) + H(s)ln\Lambda(s) - lnH(s)!] \tag{4.25}$$

Differentiating $l(\boldsymbol{\lambda})$ with respect to $\lambda(j)$ yields,

$$\frac{\partial l(\boldsymbol{\lambda})}{\partial \lambda(j)} = -\sum_{s=1}^{S} p(j,s) + \sum_{s=1}^{S} \frac{p(j,s)H(s)}{\sum_{j=1}^{J} \lambda(j)p(j,s)} \tag{4.26}$$

Taking now first and second derivative of the log-likelihood function, it can be shown [93] that the matrix of second derivatives is negative semidefinite and that $l(\boldsymbol{\lambda})$ is concave. Consequently, sufficient conditions for a vector $\boldsymbol{\lambda}$ to be a maximizer of l are the following Karush-Khun-Tucker conditions[94]:

$$[\lambda(j)\frac{\partial l_c(\boldsymbol{\lambda})}{\partial \lambda(j)}]_{\boldsymbol{\lambda}} = 0 \tag{4.27}$$

and

$$[\frac{\partial l(\boldsymbol{\lambda})}{\partial \lambda(j)}]_{\lambda} \leqslant 0 \text{ if } \lambda(j) = 0 \tag{4.28}$$

for each j = 1,2...J. The equation for the Expectation Maximization (EM) algorithm can be now derived by solving Eq. 4.27:

- start with an initial estimate $\lambda^{(0)}$, satisfying $\lambda^{(0)}(j) > 0$, $i = 1, 2, ..., I$.
- given $\lambda^{(k)}$ denoting the estimate of λ at the *k-th* iteration, define a new estimate $\lambda^{(k+1)}$ as:

$$\lambda^{(k+1)}(j) = \frac{\lambda^{(k)}(j)}{\sum_{s=1}^{S} p(j,s)} \cdot \sum_{s=1}^{S} \frac{H(s)p(j,s)}{\sum_{j'=1}^{J} \lambda^{(k)}(j')p(j',s)} \ , \ j = 1, 2, ..., J. \tag{4.29}$$

- if the required accuracy for the numerical convergence has been achieved, then stop iterating.

The term

$$\sum_{j'=1}^{J} \lambda^{(k)}(j')p(j',s) \tag{4.30}$$

referred to as the **Expectation** (E) step, determines the expected projection from the current estimate of the activity distribution. The term

$$\lambda^{(k)}(j) \sum_{s=1}^{S} \frac{H(s)p(j,s)}{\sum_{j'=1}^{J} \lambda^{(k)}(j')p(j',s)} \tag{4.31}$$

called the **Maximization** (M) step, is used to determine the relative difference between the estimated and measured projections to move the current activity distribution to be closer to the solution. The term $\sum_{s=1}^{S} p(j,s)$ is often called, especially in medical imaging applications, the *sensitivity matrix* of the system.

Properties of ML-EM

Given a non-negative initial image $\lambda^{(0)}$ and a non-negative $p(j,s)$ and $H(s)$, then all images produced by the algorithm are non-negative. This is an important advantage of the method in comparison to other iterative techniques such as Least Squares, which can result in meaningless negative values for the emission density in certain voxels.

For each image vector $\lambda^{(k)}$ produced by the algorithm, the sum of photons in the image is equal to the sum of the counts in the data. This property follows immediately from the iterative step Eq. 5.1, from which is found that:

$$\sum_{j=1}^{J} \lambda^{(k)}(j) = \sum_{s=1}^{S} H(s). \tag{4.32}$$

That means that the EM algorithm is self-normalizing, and the redistribution of the activity in the image cells, that occurs after each iteration, is accomplished without any net increase or decrease in the total activity.

The EM algorithm can provide a physically accurate reconstruction model, since it allows to directly incorporate many physical factors, which, if not accounted for, can introduce errors in the final reconstruction. Factors can be represented in the system matrix $p(j,s)$ include, for example:

- bulk attenuation and scattering in the active medium;
- efficiency of the detector with respect to the photon wavelength or angle of incidence;
- photon time-of-arrival.

A major disadvantage of the EM reconstruction algorithms, as it happens with most iterative techniques, is the slow convergence rate to an acceptable image and the high computational cost for a practical implementation. However, the use of EM algorithm has been found to produce superior results [95] [96] in comparison with the convolution methods by reducing noise and streak artifacts. In addition, the projection data are not required to be equally spaced [97].

Considering the reasons mentioned above and the fact that scintillation light emission in Liquid Argon and SiPM photon detection can be described with the Poisson statistics [98], we chose to implement the ML-EM algorithm as principal technique for reconstruction of tracks in the GRAIN detector. In the next chapter we will cover details of the algorithm implementation and the system matrix computation.

Chapter 5

Reconstruction implementation

5.1 ML-EM algorithm implementation with coded aperture cameras

In the previous chapter we explained the reasons behind choosing the Maximum Likelihood expectation algorithm to be implemented as the preferred method for reconstructing events with Coded Aperture Masks.
The iterative algorithm can be summarized in equation 5.1:

$$\lambda^{(k+1)}(j) = \frac{\lambda^{(k)}(j)}{\sum_{s=1}^{S} p(j,s)} \cdot \sum_{s=1}^{S} \frac{H(s)p(j,s)}{\sum_{j'=1}^{J} \lambda^{(k)}(j')p(j',s)} \quad \text{with} \quad \lambda^{(0)} = 1 \tag{5.1}$$

The key element in this algorithm is the system probability matrix, which expresses the relationship between the measured data $H(s)$ and the estimated voxel vector λ. It represents the probability $p(j,s)$ with which each photon emitted from a voxel j of the unknown photon emission distribution is detected by a specific sensor.
In this probability matrix the geometrical setup of the system is taken into account. In addition, other physical parameters such as the mask transfer function, photon attenuation, scattering, sensor detection efficiency need to be included in order to obtain a physical model as close as possible to reality [99].
A reliable method to calculate the probability matrix is to use Monte Carlo techniques. By simulating a point photon source in a voxel and implementing all the physical processes related to photon propagation and detection, it is possible to compute $p(j,s)$ as:

$$p(j,s) = \frac{\text{n photons emitted in voxel j and detected by sensor } s}{\text{total number of photon emitted in voxel } j}. \tag{5.2}$$

However, Monte Carlo simulations require a large number of photons simulated for every point source for a sufficient numerical accuracy and at least a simulation of a point source placed in every voxel, thus requiring a large computational time. While it may be a feasible and accurate method with a finalized detector geometry, it is not possible to employ it during the designing stage of a detector, where many geometry parameters need to be tested quickly.
A possible alternative is to use an analytical method. This method can prove to be a complex geometric problem, especially in a full 3D reconstruction. So, in practice, it is necessary to make geometric approximations that may affect the accuracy. However, if the required number of mathematical operations is low enough, it may also be possible to perform real-time calculation of the probabilities every time an event is processed. In the following sections we will discuss in detail the required geometrical computations for obtaining the system matrix.

5.1.1 System Matrix analytical calculation

The probability for a sensor to detect a photon emitted in a specific voxel depends on several factors that can be grouped in three categories: the geometry of the detector, the scintillating photons propagation medium characteristics, and the sensor detection efficiency. By describing each of these factors with a probability matrix, we can express the total probability with a factorization of these effects:

$$P = P_{geom} \cdot P_{LAr} \cdot P_{sensor} \tag{5.3}$$

The geometrical probability depends on the geometry of the detector, the camera geometry, and the voxel grid.
Assuming that (i) photons are emitted isotropically from each voxel; (ii) each photon propagates in a straight line; (iii) the distance is large compared to the voxel size, the geometrical probability that a photon emitted from voxel j will be detected from detector s can be approximated as:

$$P_{geom} = \frac{\Omega}{4\pi} \tag{5.4}$$

where the angle Ω is the solid angle subtended by the detector area, with origin in the voxel centre. With a coded aperture mask placed between the region of interest and the sensor, one must consider the portion of sensor area that is "visible" from the voxel through the mask holes. This is obtained by computing the mask hole shape projection from the voxel center to the sensor plane and determining in this way the intersecting

areas between the projection and the sensor, as shown in Fig. 5.1. In the event that a sensor is visible through multiple holes, the solid angle is given by the sum of the angles subtended by all the visible sensor portions.

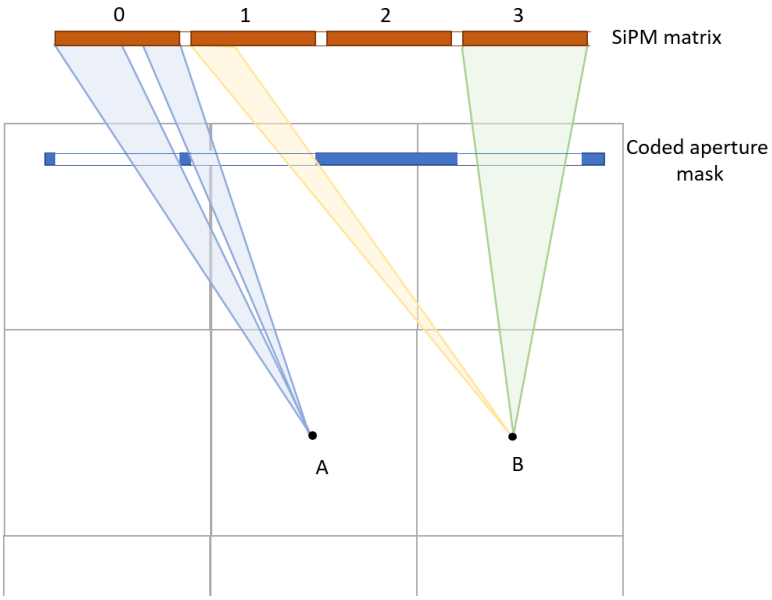

Figure 5.1: 2D diagram of the solid angle calculation for various voxels and sensors. The matrix SiPMs are drawn in red, and parallel to them, in blue, the coded aperture mask. The voxel with center in A sees sensor 0 through two holes in the mask, its solid angle is equal to the sum of the angles subtended by the two portions of sensor area visible. For voxels with center in B, the solid angle relative to sensor 1 is bounded by the mask hole, while the entire sensor area of sensor 3 is visible. The dimensions of the pixel edges and mask holes are taken into account in this geometric modeling, since they are of non-negligible size in relation to the sensitive area.

In GRAIN, photons emitted in a voxel propagate in Liquid Argon and are subjected to attenuation in the medium, due to photon absorption ad Rayleigh scattering. Both processes will affect the number of detected photon as an exponential decay depending on the LAr properties and the distance between the emission voxel and the sensor. The probability of the detection can therefore parameterised as:

$$P_{LAr} = P_{att} \cdot P_{scatter} = \exp\left(\frac{-d}{1/\lambda_{att} + 1/\lambda_{scatt}}\right) \tag{5.5}$$

where d is the distance between the voxel center and the sensor surface center, and

λ_{att} and $\lambda_{scatter}$ are respectively the attenuation length and scattering length of Liquid Argon.

Including scattering only as an attenuation effect in the probability matrix leads to an underestimation of the total number of photons measured in a camera, since some of the photons that undergo scattering could do so at a very small angle and still end up in the sensitive area of the camera. However, the literature on experimental measurements of Argon properties is limited (see Sect. 3.2.4), and there is no specific measurement of the average scattering angle of its scintillation light. Here we have used simulated process results based on theoretical calculations of the Rayleigh scattering, and we plan to return to more precise modeling of the process in the future when such measurement results become available. We can, however, consider in simulations the effects of scattering as irreducible noise that will affect the reconstruction quality.

Lastly, the probability of detection depends on the sensor detection efficiency. For a SiPM, the photon detection efficiency (PDE) strongly depends on the photon wavelength [100]. As it is not possible to measure the wavelength of a photon that impinges on the SiPM surface, an average PDE value weighted over the LAr scintillation emission spectrum is assumed.

Moreover, recent measurements report that in the VUV region a SiPM PDE also depends on the incident angle of the photon [101]. It can be seen in Fig. 5.2 that the relative PDE of a SiPM with Liquid Xenon scintillating light decreases with the incident angle of the photon. Again, a similar measurement in LAr has not been performed yet, and we approximate this behaviour with the assumption that the relative PDE tends to zero for large incident angles ($\theta > 80\circ$).

To summarize, the detection probability is given by:

$$P_{sensor} = PDE \cdot P_{\theta} \tag{5.6}$$

where P_{θ} is the relative PDE factor depending on the photon incident angle.

5.1.2 Stopping criterion

Fig. 5.3.a shows the trend of log-likelihood in an example reconstruction as a function of the number of iterations. It can be seen how the log-likelihood tends to a maximum value as the number of interactions increases. At the same time, the relative difference:

$$\frac{|l(\lambda^{(k+1)}) - l(\lambda^{(k)})|}{l(\lambda^{(k)})} \leqslant 10^{-3}. \tag{5.7}$$

decreases asymptotically to 0 (Fig. 5.3.b).

Since the EM algorithm is an iterative method, stopping the algorithm at a certain

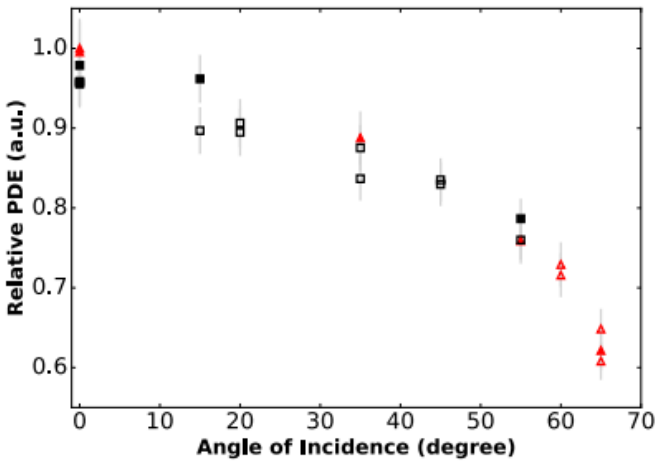

Figure 5.2: Relative PDE of the Hamamatsu S13370 VUV4 SiPM in LXe as a function of photon incident angle, taken from [101]

point for which the image quality is"good enough" or (ideally) the optimum that one can obtain, can avoid the problem of image deterioration due to noise amplification [92] and save computation time.
Convergence of the EM algorithm is generally defined as a sufficiently small change in parameters [102] or in the log-likelihood function [103]. We choose the latter based on the log-likelihood function as the criterion for stopping iterations of the algorithm in our reconstructions, as it allows us to compare a single value between iterations. We define as a limit to stop the algorithm iteration a relative variation in likelihood of 10^{-3}.

This is an immediate and easily defined criterion and, on average, stops the reconstruction after $\sim 25-30$ iterations for point sources and $\sim 8-10$ iterations for track sources. A higher level of convergence can be imposed, but in this case the absence of noise artifacts is not guaranteed.
In fact, in every MLE the likelihood function is monotonically increasing after each iteration and does not provide any direct information on the quality of the reconstructed images in terms of noise and edge artifacts. Future studies will focus on choosing or developing a more suitable criterion that also takes this issue into account. The issue of stopping the EM algorithm for imaging has been studied extensively in the literature, and quantitative criteria are either based on statistical hypothesis testing methods [104], perform cross-validation, or define an empirical figure of merit to determine the image quality of a known reconstructed source [105].

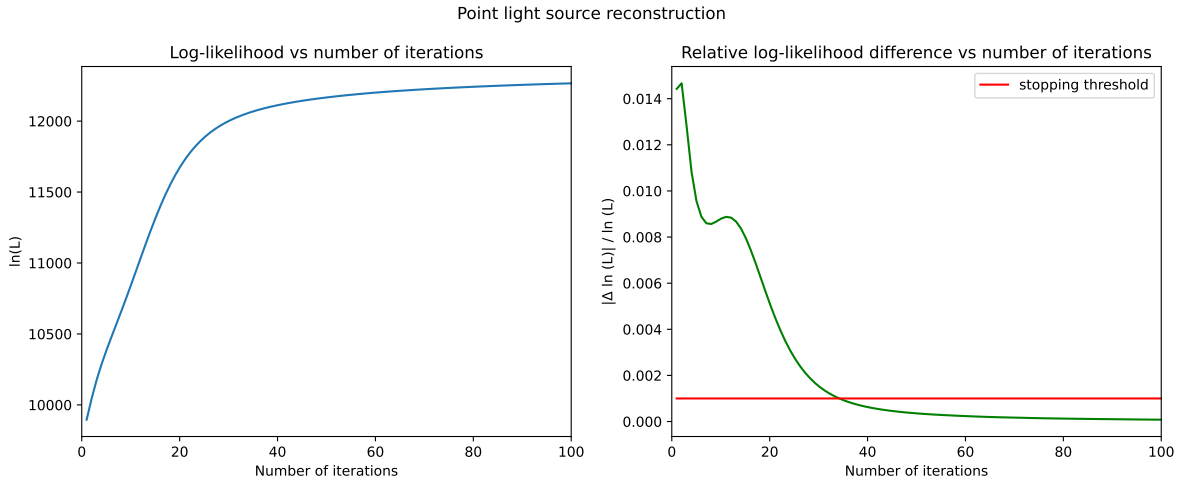

Figure 5.3: Log-likelihood (left) and relative difference of log-likelihood (right) evolution as function of number of algorithm iterations. The chosen threshold for stopping the iterations is shown in red.

5.1.3 Reconstruction with multiple cameras

While it is possible to do a three-dimensional reconstruction with a single camera, the resolution on the axis orthogonal to the camera will be very limited. At least three orthogonal cameras are needed for a reconstruction with equal resolution on all axes.
The ML-EM algorithm, described so far for use with a single camera to simplify nomenclature, can be used directly with multiple cameras by including in the system matrix the probabilities for all sensors, regardless of which camera they belong to. This is feasible with a small number of cameras, but for larger systems such as GRAIN, where dozens of cameras will be needed to cover the entire active volume, it becomes problematic due to memory constraints.
The size of the system matrix is related to the dimension (2D or 3D) of the acquisition, the required voxel granularity, the number of detectors, and the size of the reconstructed volume. In our application, this matrix is very large and may be difficult to store or manipulate. The dimension of the system matrix are J x S (number of voxels $\times$ number of pixels in a SiPM matrix) for one camera, and multiple cameras are required to perform a full 3D reconstruction. Considering GRAIN size ($130 \times 120 \times 48$ cm^3) segmented in voxels of 1 cm^3, and a SiPM matrix with 1024 pixels, a camera system matrix contains $O(7 \cdot 10^8)$ elements. If stored with single precision floating point a matrix element requires 4 bytes of storage, meaning that the system matrix size is about 2 GBytes.
It therefore becomes a practical necessity to subdivide the process and we decide to per-

form a reconstruction of the entire volume for each camera, and subsequently multiply them together to get the final result.

$$\lambda(j) = \prod_{c} \lambda(j, c) \tag{5.8}$$

5.2 Full simulation chain

To optimize the camera geometry of GRAIN and study its performance, a detailed Monte Carlo simulation was developed. Several software tools were used and implemented to perform the various steps of the simulation framework, from neutrino interaction generation to reconstruction, as shown in the schematic in Fig. 5.4. This section will describe the implementations of the different steps of the simulation framework.

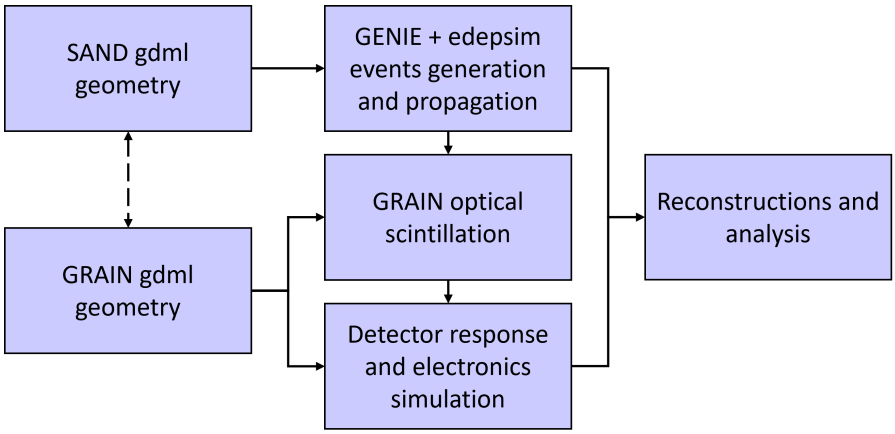

Figure 5.4: Diagram of the simulation and reconstruction chain.

5.2.1 Geometry description

All test geometries and GRAIN geometry are implemented using the Geometry Description Markup Language (GDML). It is a format based on the XML language, commonly used to describe detectors geometries in HEP framework such as Geant4 [106] and ROOT [107].

Camera geometry

Independently from its configuration, a coded aperture camera is always composed of three elements: a sensor, a mask and a body. The sensor is simulated as a 1 mm thick

silicon plane with side dimensions defined by the specific configuration under study, usually about 10 cm. The mask is obtained starting from a 0.1 mm thick metal sheet with squared holes, with dimension and position defined based on the desired configuration, usually about 3 mm. The body is a 1 mm thick metal box used to enclose the sensor and shield it from undesired light. The front face of the body is the mask, leaving only the holes of the mask as apertures between the inside of the body, where the sensor is located, and the outer volume. Liquid Argon fills the camera body. The geometry of three example cameras is shown in Fig. 5.5.

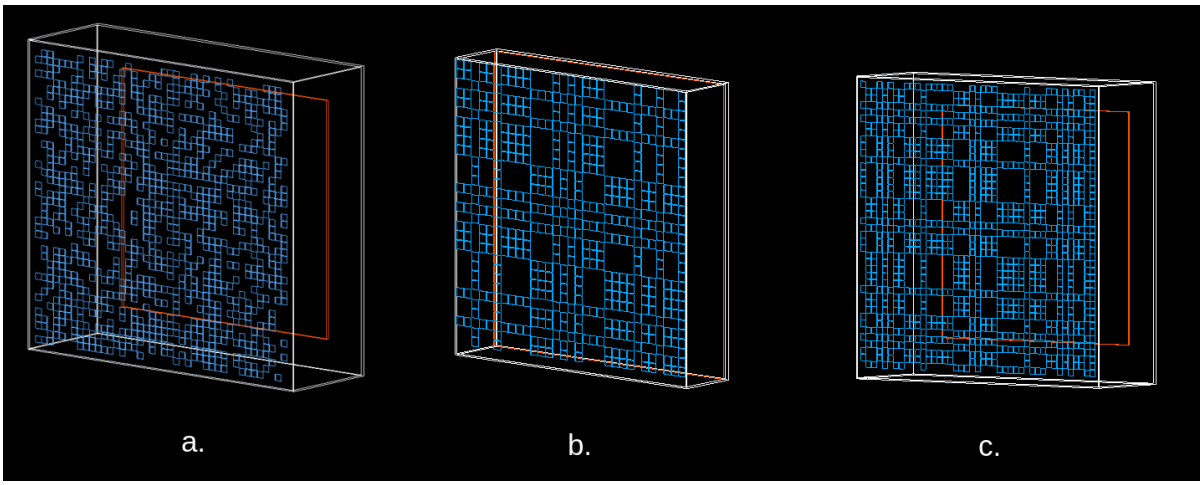

Figure 5.5: Examples of coded aperture camera geometries. The body (white) is 1 mm thick 100% opaque material, the sensor (red) is placed inside the body on the rear face. The mask (blue) replaces the body's face on the opposite side of the sensor. Each square on the mask represents a hole.

Test geometries

To evaluate the performance of a camera without the additional complexity of its positioning within GRAIN, a test geometries was employed, shown in Figure 5.6. It consists of a vessel of 50x50 cm^2 side and 80 cm depth, with a camera positioned in the center of one of the side surfaces. This geometry was used to evaluate the resolution of the camera in reconstructing point light sources (Section 6.2.1) and tracks of minimum ionizing particles (Sect. 6.2.2). The vessels is are filled with argon, simulated as a mixture of ^{36} Ar, ^{38} Ar, and ^{40} Ar, as shown in Table 5.1.

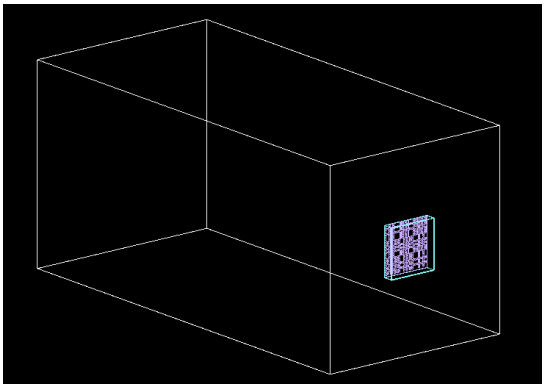

Figure 5.6: Simplified geometry used to evaluate camera performance and spatial resolution.

Argon mixture	
^{36}Ar	0.34 %
^{38}Ar	0.06 %
^{40}Ar	99.6 %

Table 5.1: Argon composition as implemented in the simulation.

SAND and GRAIN

The entire volume of the SAND detector was simulated using General Geometry Description (gegede), a software recommended by the DUNE Collaboration to generate constructive complex geometries [108] . The complete geometry of SAND is visible in Figure 5.7, which shows its XY and XZ sections. This geometry includes all the components detailed in Chapter 3. In the SAND geometry, the GRAIN external vessel material is implemented as a carbon fiber-honeycomb-carbon fiber multilayers structure, for a total thickness of 62 mm. The endcaps are simulated as 16 mm of steel. The inner vessel is entirely made of steel. Both vessels are implemented as elliptical modules with a major axis of 192.4 and minor axis of 85.4 cm and length of 193.2 cm for the external vessel, and 23.75 and 72.8 cm for the inner one, with a length of 65 cm. The geometry of the cameras inside the volume of GRAIN is not simulated at this level but is implemented in an independent geometry used exclusively to study the optical readout.

To allow a greater flexibility when studying different cameras configurations, a separate GRAIN geometry was developed. This geometry shares the same dimensions of the one in the SAND geometry, but includes only the inner vessel and the geometry of the cameras. This choice allowed us to simulate neutrino interactions just one time in the

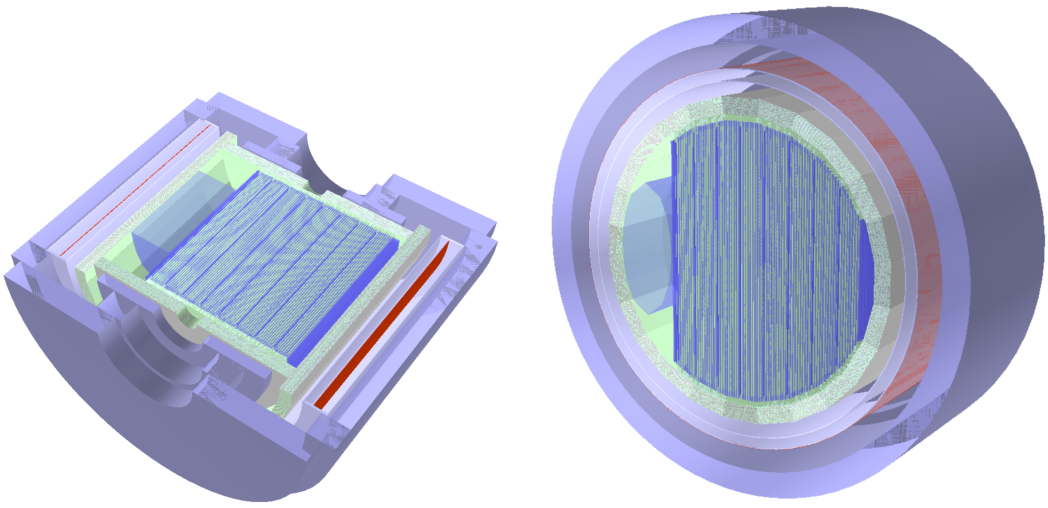

Figure 5.7: X-Z (a) and X-Y (b) sections of the SAND detector geometry.

SAND geometry and use the results to study many different readout configurations using the same events. The inner vessel was simulated as described in the previous paragraph, with multiple cameras added inside it. The inner vessel is filled with an argon mixture with isotope percentages according to Tab. 5.1. A complete geometry of GRAIN, including different camera configurations, is shown in Fig. 5.8.

5.2.2 Event generation and energy deposits

Cosmic ray tracks and light point sources used for algorithm validation and geometry optimization were simulated directly in GEANT4 through dedicated macros. A point source is defined as an isotropic emission of 10^7 photon with wavelength corresponding to LAr scintillation light spectrum.
Neutrino interactions are generated by the GENIE neutrino event generator [109], officially adopted by the DUNE Collaboration. GENIE is a ROOT-based MC generator which not only simulates the primary interactions of the neutrino with a nucleon, but also subsequent interactions of the recoiled nucleon with all the other spectator nucleons. Genie includes a description of the main scattering mechanisms for all the neutrino flavors and target types, which can be roughly subdivided into three categories: nuclear physics models, cross-section models, and hadronization models.
Particles emerging from neutrino primary interactions are also included in the GENIE output. They propagate inside the detector, depositing energy and eventually producing

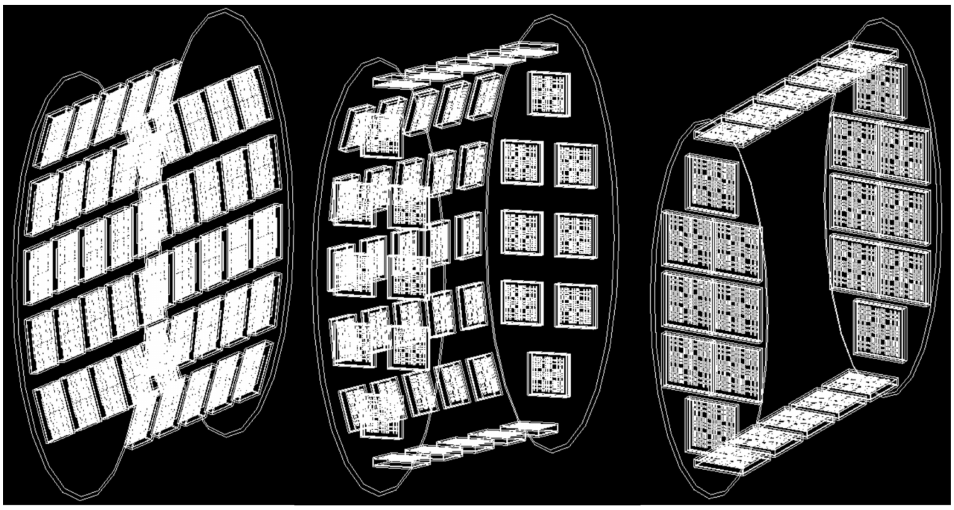

Figure 5.8: three configuration of the independent GRAIN geometry. The dimension of the inner vessel are the same as in SAND *gegede* geometry, while the position, number, and type of cameras can be freely changed.

secondary particles. The particles' propagation and their energy release were simulated by Edep-sim software [110], a wrapper around the GEANT4 simulation tool.
Edep-sim simulation implements a fairly detailed model of the energy deposited as ionization and scintillation, using the NEST simulation package [110]. NEST is an extensive collection of models that describe both the scintillation light and ionization yields of noble elements as a function of particle type,electric field, and incident energy or energy loss (dE/dx). Edep-sim processes the GENIE output file, providing information about the evolution of neutrino interaction events. In particular, it provides information on the primary particles produced by neutrino interactions, information on the trajectory of each simulated particle including all the secondary particles produced during the primaries propagation, and information on each energy deposit. For the last step, the starting and stopping positions of each deposit are recorded, as well as the particle that generates the deposit and the primary particle of the depositing ones.

5.2.3 Optical Simulation

The Edep-sim propagation results are used to simulate the optical scintillation emission by liquid argon in GRAIN. This is done by means of a dedicated Geant4 simulation, which uses the energy deposit information to emit, propagate, and collect the scintilla-

tion photons in the independent GRAIN geometry. The most relevant optical properties of the argon, such as emission spectra, singlet-to-triplet ratio, and Rayleigh scattering, are included in the simulation and parameterized on the basis of the available literature (see Sect. 3.2.4). Table 5.2 shows a recap of all the liquid argon properties as implemented in the simulation.

LAr - Light emission	
light yield	40k photons/MeV
$\tau_{singlet}$	7 ns
$\tau_{triplet}$	1.6 μs
λ	127 nm
L_s / L_3	0.25 electron recoil
	0.7 nuclear recoil
LAr - Light propagation	
$\lambda_{scatter}$	90 cm
λ_{abs}	5 m

Table 5.2: Liquid argon properties' values as implemented in the simulation.

The propagation of the photons can be affected by both the Rayleigh scattering and the absorption by impurities [71]. Despite both effects being wavelength-dependent, they are implemented in the simulation with a constant characteristic length. The scattering length ($\lambda_{scatter}$) is set to a value of 90 cm. The absorption length (λ_{abs}) is set to a value of 5 m. This value is slightly higher than the values of pure argon reported in the literature, but, as suggested in [74], the absorption length increases for very pure argon or in the case of specific argon impurities (such as Xenon). The refractive index is implemented from the results obtained in [71]. However, since the reconstruction in GRAIN is based on the imaging (Sect. 3.2.4), the reflection of the materials inside the inner vessel must be reduced to the minimum possible to avoid detecting photons not coming from the source. The surface reflection, despite being simulated, is set to 0%, with 100% absorption probability.

As described in Sect. 3.2.4, each camera in the GRAIN geometry includes a sensor volume. These volumes are set as sensitive detector of the simulation and collect information of each optical photon impinging on their surface. These information are the output of the simulation and are later used to simulate the response of the detector and the electronics. At this level, the sensors have 100% efficiency and no fine structure is simulated. This allows us to simulate different sensor and electronic properties without

the need of running the optical simulation multiple times. Among the information collected by the sensors, the most important ones are: the incident photon position and direction on the sensor, its detection time and the photon energy.

5.2.4 Detector Response

The response of the camera SiPMs to the collected photons was simulated with a standalone software. This includes modeling the SiPM response and properties of the front-end electronics, based on parameters available from laboratory measurements or datasheets. This tool returns the map of the number of photons detected on a SiPM matrix and the arrival time of the first photon for each pixel, which are then used as inputs to the reconstruction.
This simulation tool is implemented in Python, with parts in Open CL for GPU computation acceleration.
A simplified version of the detector response is also available. This one, which we will refer to from now on as the "fast response" is less detailed but much faster in execution time: instead of calculating the waveform and the response of the electronics, it only performs a count of interacting photons based on photon position and PDE of the sensor and adds a smearing for noise.

SiPM signal modeling

The first step in the simulation process is to assign each photon arriving on the matrix surface to its corresponding pixel. The total area of the matrix implemented in the geometry *gdml* file includes the edges and dead areas between pixels. Regardless of its size, each SiPM has a nonsensitive outer edge of 0.1 mm, for a dead space between one SiPM and another of 0.2 mm. This space is taken into account here, and photons that do not arrive on the active area of the SiPM are discarded. Out of the total amount of photons actually arriving on the active surface of the sensors, one can determine which of them interacts according to a random process. For each photon, a probability value with uniform distribution (0,1) is extracted; for $P < PDE$ the photon is considered to be interacting and an amplitude value is assigned, extracted as a random value from the Gaussian distribution $G(A, \sigma_A)$, where A is the average amplitude value in mV generated by a photoelectron, a quantity that can be measured in the laboratory with measurements of a single photoelectron spectrum. The PDE of the SiPM can be a fixed value, or different PDE values can be set depending on the wavelength of the incident photon, calculated from its energy.
For each interacting photon, the same calculation was performed in the above manner whether it produces a corresponding crosstalk photoelectron and/or afterpulse. In the

former case, another photon with the same characteristics (position, time, energy, amplitude) as the one that generated it is added to the list of interacting photons. If an afterpulse photon is generated, instead, it is assigned a time equal to the photon that generated it plus a randomly extracted delay from the exponential decay:

$$t_{afterpulse} = \exp(1/\tau_{afterpulse}), \tag{5.9}$$

where $\tau_{afterpulse}$ denotes the average delay time in the generation of the afterpulse. Its amplitude is calculated as the corresponding amplitude value of its primary photon waveform according to the function described in the next paragraph, but at $t_0 = t_{afterpulse}$.
A number of random photons of dark noise is also generated for each SiPM according to the Poisson distribution, with average expectation value given by the characteristics of the SiPM. A random delay due to the Single Photon Time Resolution of the SiPM (SPTR) is also added to the time of each interacting photon, extracted from a Gaussian distribution with $\mu = 0$ and $\sigma = SPTR$, typically of the order of 100 ps.

With a preliminary total number of detected and noise photons, for each photon at $t = t_0$ a waveform is simulated according to the following empirical model:

$$f(t) = \begin{cases} 0 & \text{if } t \leqslant t_0 \\ A \cdot (t - t_0)/\tau_{rise} & \text{if } t - t_0 \leqslant \tau_{rise} \\ A \cdot e^{\frac{-(t-t_0-\tau_{rise})}{\tau_{fast}}} & \text{if } t \leqslant_{rise} +\tau_{fast} \\ A \cdot e^{\frac{-(t-t_0-\tau_{rise})}{\tau_{slow}}-1} & \text{if } t > \tau_{rise} + \tau_{fast} \end{cases} \tag{5.10}$$

where A is the precalculated amplitude value for each photon, τ_{rise} the rise time of the SiPM signal, τ_{fast} and τ_{slow} are two parameters that describe its exponential decay. It is also possible to set a maximum length for the simulated waveform, its sampling period (T_{sample}) and a time offset for the arrival of photons.
The waveforms generated by each photon are then summed together to obtain the total SiPM response.

In Tables 5.3 and 5.4, we summarize all parameters that can be entered into the configuration file with the values used as baselines to perform the simulations in the next chapters. An example waveform generated with these parameters is shown in Fig. 5.9.

DAQ system modeling

Once the response signal of the matrix pixels is obtained, the electrical signal must be processed by some type of readout electronics for digitization and acquisition. At

SiPM parameters			
PDE	0.25	DC rate	0.1 Hz/mmˆ2
τ_{rise}	0.8 ns	P crosstalk	0.07
τ_{fast}	1 ns	P afterpulse	0.3
τ_{slow}	50 ns	$\tau_{afterpulse}$	1 ns
A_{1pe}	10 mV	sptr	150 ps
$\sigma_{A_{1pe}}$	2 mV		

Table 5.3: SiPM parameters used in the simulation.

Waveform parameters	
duration	500 ns
T_{sample}	0.1 ns
saturation	1.5 V
baseline	10 mV
baseline white noise	2 mV

Table 5.4: Waveform parameters used in the simulation

this point, signal processing depends on the type of readout electronics that we want to simulate. The types of architectures are limited in that there are few ASIC models currently in existence that can be used for reading SiPMs in a cryogenic environment, with characteristics that make them suitable for GRAIN, because of speed requirements, power consumption and channel density limitations. In general, there are two suitable architectures being developed:

1. A discriminator followed by a dual edge TDC, to determine the number of photons based on the time above threshold of the signal. Already available with this type of architecture is the 32-channel mixed-signal ASIC ALCOR [111], developed for the Darkside experiment, and currently under testing for the readout of the first cold prototype of GRAIN's optical system. ALCOR has two pairs of fixed threshold TDCs; for each pair, one is for the rising edge and the other for the falling edge. The TDCs have a dead time of 150 ns, but the two pairs alternate to mitigate this limitation. The time above threshold of a signal produced by a certain number of photons depends on the parameters of the SiPM waveform and the threshold set. To calculate the calibration coefficient, we simulate the waveform generated by the SiPM upon the arrival of 1, 2 , ..., N photons and measure the time above threshold. Fig. 5.10 shows an example of calibration with the parameters in Tab. 5.3 at two different thresholds.

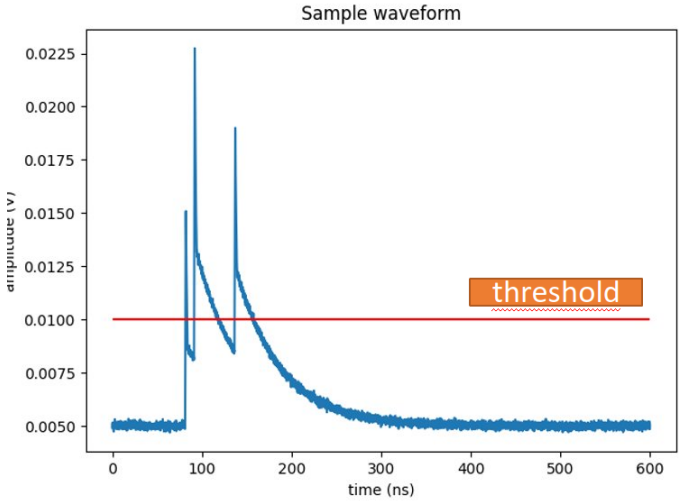

Figure 5.9: Example waveform generated from photon arrival times according to Eq.5.10. The red line represents the TDC threshold.

2. A charge integrator ADC and a TDC. With the charge integrator we can determine, after calibration, the number of photons by integrating over a fixed time interval from when the signal goes above threshold. The TDC gives the instant of time when the signal goes above the threshold. To calibrate it, multiple waveforms are simulated with the given SiPM parameters, and determine the charge corresponding to the signal produced by a photoelectron.

ASIC (1) parameters (multiple TDCs)	
threshold	7 mV
deadtime	150 ns
bandwidth	500 MHz
time resolution	50 ps
calibration coeff.	80.6 27.9 ns

ASIC (2) parameters (Charge integrator + TDC)	
threshold	15 mV
integration time	200 ns
bandwidth	500 MHz
1 pe charge	0.188 mVns
pedestal	2.00 mVns

Table 5.5: Asic parameters

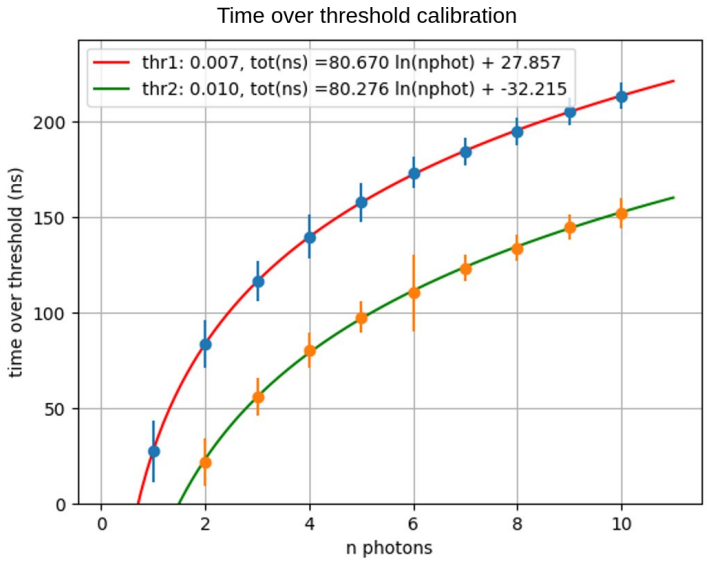

Figure 5.10: Waveform Time over threshold versus number of coincident photon that generated it at two different threshold levels. The calibration coefficients depend on both the SiPM waveform parameters and the threshold.

5.2.5 3D Reconstruction

Once we obtain the map of the number of photons measured by each camera, we can apply the ML-EM reconstruction algorithm as described in Sect. 5.1.
Given the high number of voxels and mathematical operations, the implementation of parallel computation on GPU is mandatory in order to perform the reconstruction in acceptable time. As with the detector response, this software is implemented in Python with the OpenCL kernels for parallel computation.

This software implements the elements of the geometry defined in the gdml file used for the simulation in Python objects and performs the voxel subdivision of the fiducial volume of the reconstruction, adding the possibility of excluding from the reconstruction specific voxels, e.g. those close to the walls where the cameras are positioned. The system matrix and the sensitivity matrix are precomputed as explained in Sect. 5.1.1 with a separate tool once for each geometry tested and stored. Due to the large size of the system matrix of one camera ($\sim$ 4 Gb), the reconstruction is performed separately for each camera and the voxels are successively combined as described in section. 5.1.3. For each camera contained in the output file of the detector response program, the 3D

reconstruction software applies the calculation of the ML-EM reconstruction algorithm:

1. initially sets the value of the voxels to $1/N_{voxels}$ so that $\sum_j^N \lambda = 1$;
2. performs the Expectation Step computation (see Sect. 4.4.4) on the GPU by parallelizing the execution on camera pixels;
3. performs the maximization step calculation on the GPU by parallelizing the execution on the voxels of the fiducial volume.
4. computes the likelihood value corresponding to the computed voxel amplitudes.
5. repeats steps 2-4 until the change in the likelihood ratio between iterations is less than the specified threshold ($= 10^{-3}$).

The software returns a three-dimensional array containing the λ values of voxel amplitudes of the reconstructed volume.
In the future, we plan to do a global reconstruction using the detected photons and system matrix of all cameras. This could be done with brute force and or with more sophisticated memory management and sorting algorithms.

Next steps in the reconstruction are the extraction of track points from voxel clusters with higher amplitude values and the fit of the latter. These steps, along with the integration of traces with STT and SAND calorimeter reconstructions, are the subject of future studies and we will provide some examples in the next chapters.

Chapter 6

Optimization of camera geometries

6.1 Camera geometries for GRAIN

Having described the details of the simulation and reconstruction chain implemented to test the different cameras and evaluate the performance of GRAIN, we can now discuss the decision-making process that led us to choose a selected number of camera geometries for comparison.

The number of pixels in the SiPM matrix was set at 1024 for both the lens-based and coded aperture mask systems, because although they are not available at the moment, it is entirely reasonable to expect matrices of at least this size to be produced in a few years. In addition, and perhaps most importantly, the number of channels you can have on a readout board can be a limitation. 1024 channels may be reasonable with an evolution of ALCOR, the current ASIC being tested for the camera prototype.

To ensure sufficient light collection while keeping SiPM overall costs low, a sensor area of 9 mm^2 with an edge thickness of 0.1 mm was chosen. The square SiPM array thus has a side of 102.4 mm, in all the camera geometries discussed in this chapter.

Having fixed the dimensions of the sensor, it is necessary to define the parameters of the mask and its distance from the sensor. The number of possible parameter combinations is very large, and testing all of them systematically with the MLEM algorithm is not feasible in the scope of this thesis. Therefore, we selected some mask configurations using the depth of focus, and the width of the FCFV (see Sect. 4.3.2), as a reference in relation to the size of the GRAIN detector. The characteristics of the cameras, denoted by the letters A, B, C, D, are summarized in Tab. 6.1.

In particular, it is of interest to place the depth of focus at infinite distance (mask A, B, D), or about half the width of GRAIN (C), and verify how it affects the reconstruction of point sources. In principle, the amplitude of the point spread function or the track

Mask types

Name	Type	Rank	Hole pitch (mm)	b (mm)	Focus depth (cm)	FCFV at 60 cm distance
A	mosaic	31	3.2	20	$+\infty$	$\sim$ 1 m
B	box	31	3.2	20	$+\infty$	10.2 cm
C	box	43	3.0	40	60	60 cm
D	box	43	3.2	20	$+\infty$	60 cm

Table 6.1: List of masks tested for optimization of camera geometry.

width as a function of distance from the camera is expected to be approximately constant with infinite depth of focus, and minimum at the distance equal to the depth of focus when the depth of focus is finite.

For the FCFV we chose an option in which this is as large as the sensor itself (B), as wide as the depth of GRAIN (C, D), or $\sim$ 1.5 m large and using a mosaic mask (Sect.4.3.1) (A). In particular, we are interested in assessing how the extent of the FCFV affects the ability to reconstruct tracks on the upstream edge of the fiducial volume, as it is important for GRAIN to distinguish between tracks that originate within its volume and thus potentially come from neutrino interactions on LAr and particles entering GRAIN from outside.

The pattern used for the masks is of the MURA type (Sect. 4.2.3). Fig. 6.1 shows the rank 31 and 43 MURA patterns used in the selected camera geometries. A comparison between a mosaic (mask A) and box (B) configuration, with the same parameters, lets us assess whether and how much the mosaic configuration allows for better reconstruction with the MLEM algorithm, at the expense of a larger space occupied by the camera.

Finally, the camera with the best performing configuration will be compared to a mask with the same parameters but a random pattern to see if there is a difference in performance and/or a variation in the reconstruction artifacts present, as random masks are much easier to adapt to the required dimensions or depth of focus.

6.2 Camera Comparison

In this section, we describe the procedure defined to compare different camera configurations.
As mentioned in Section 5.1.3, at least two orthogonal cameras are required to obtain a reconstruction with the same resolution on the spatial axes. However, this renders the performance evaluation of the camera geometry itself complex, as the reconstruction is

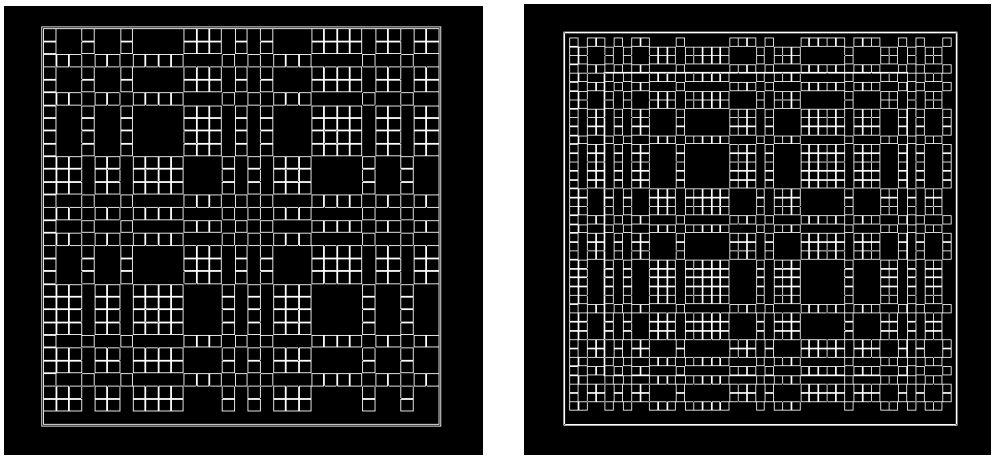

Figure 6.1: MURA mask patterns with rank 31 (left) and 43 (right) used for the camera geometries.

also affected by the relative positioning of the cameras.
However, we can evaluate the reconstruction of a single camera in the X-Y plane parallel to the camera, assuming known Z-axis distance from the camera of the light source, either a point or a two-dimensional track.
The camera under test is placed in test geometry 1., shown in Fig. 6.2 and described in Sect. 4.2.1, in the center of the lateral side.

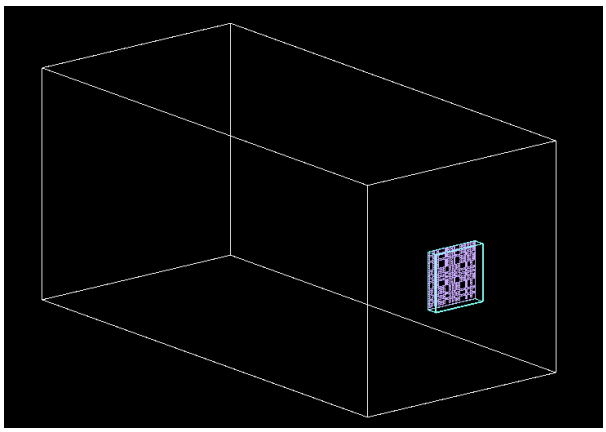

Figure 6.2: Schematic of the simulated test geometry with one camera.

By simulating light sources at different distances from the camera, we first assess their reconstruction capabilities by comparing the position of the reconstructed point or

track with the MC truth, and evaluate the quality of reconstruction considering its point spread function width or tracks width and length. A smaller reconstructed point spread function and track width indicate a better reconstruction, while the track length should be the same as the true one, and it can be considered as an estimation of the effective FoV of a camera.

In the simulations aimed at choosing the best performing camera geometry, we used the fast detector response (Sect. 5.2.4), with a sensor PDE set to 25%. Only photons arriving at the sensor surface in the first 200 ns from the onset of the event were collected.

Once we have selected the best performing camera for the reconstruction in the source plane, we will evaluate their abilities to reconstruct minimum ionizing particle tracks in three dimensions using test geometry 2.

6.2.1 Point source reconstruction

For each camera configuration we simulated 1000 uniformly distributed point sources emitting isotropically 1×10^7 photons each. Examples of the reconstruction, shown on the x-y voxel slice corresponding to the simulated point distance along z, are presented in Figure 6.3. The reconstructed point spread function was then fitted with a two-dimensional multivariate Gaussian function, whose standard deviations σ_x and σ_y are defined to be the quantitative value of the width of the reconstruction. In the same example figure, the contour line of the fitted Gaussian corresponding to 1 σ is shown in red.

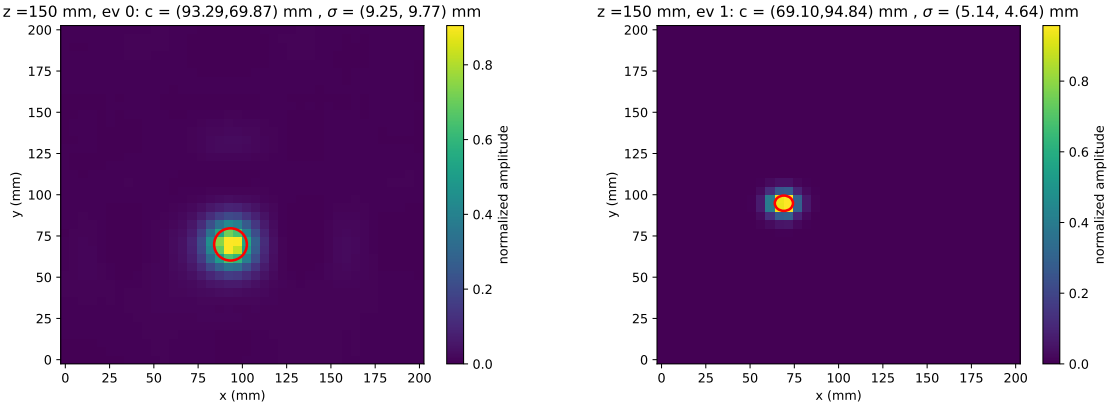

Figure 6.3: Reconstruction examples of a point source at different positions and distances from camera A. In red the profile of the 2D gaussian that fits the voxel distribution.

Figure 6.4 shows the average value over xy of the standard deviation obtained from the fits, as a function of distance from the mask. In Fig. 6.5, on the other hand, the x and y distance between the reconstructed position corresponding to the center of the Gaussian distribution and the Monte Carlo truth is shown.

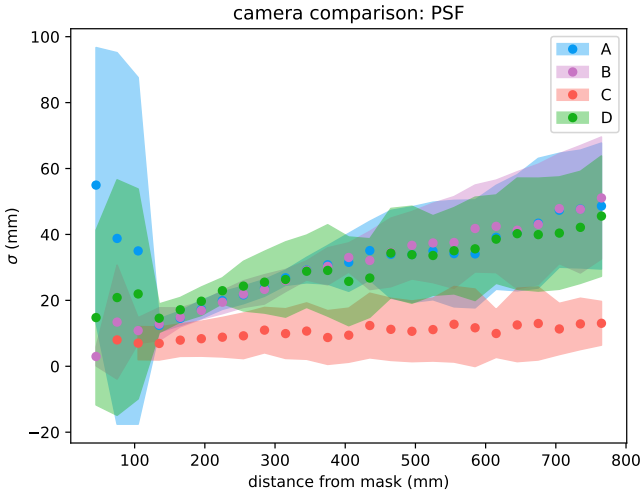

Figure 6.4: Average value over xy the point spread function width, as a function of distance from the mask. Values are plotted in bins corresponding to 3 cm distance. The colored bands represent 1 standard deviation of the values in the bin.

From these results we can infer that:

1. a depth of focus corresponding to the distance to the center of GRAIN (camera C) allows a better reconstruction of the point source: its standard deviation is approximately constant as a function of the distance of the source from the mask, with an average value of 10.4 mm;

2. there are no substantial differences between the cameras with depth of focus at infinity for distances from the mask greater than 10 mm. Camera B manages to reconstruct with comparable performance to camera A and D despite its much narrower FCFV. In contrast, camera A and C fail to correctly reconstruct sources at distances less than 100 mm.

3. Although a depth of field placed at infinity should in theory maintain the PSF width constant, the farther away the source, the wider the reconstruction appears. This is due to two factors:

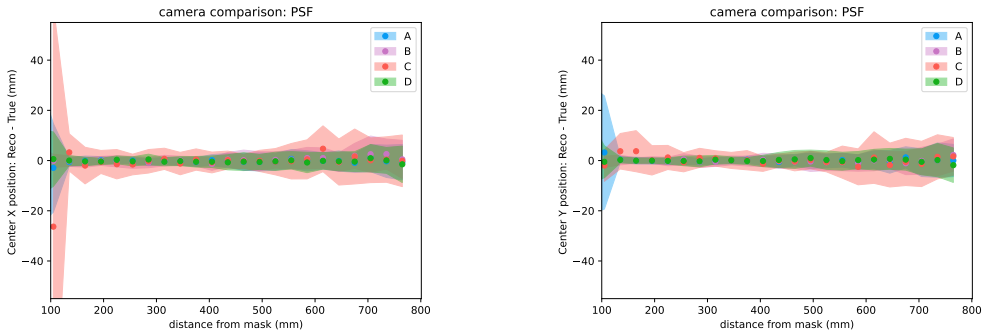

Figure 6.5: Distance between the reconstructed position corresponding to the center of the Gaussian distribution and the Monte Carlo truth, along the horizontal (left) and vertical (right) axis. Values are plotted in bins corresponding to 3 cm distance. The colored bands represent the range of $\pm 1\sigma$ of the values in the bin.

- for the same number of simulated photons per point source, as the distance increases, the number of photons arriving on the camera exponentially decreases due to absorption and scattering in LAr, in addition to the decrease due to distance itself;
- with increasing distance, photons that are scattered at small angles accumulate in incorrect pixels, leading to reconstruction artifacts.

In contrast, for camera C, an improvement in focus as one approaches the plane corresponding to the depth of field compensates for the degradation effects of the reconstructed image due to attenuation and scattering.

This preliminary test suggested that a depth of focus at a finite position may be advantageous for GRAIN, but the deciding factor for use within GRAIN is the camera's ability to reconstruct tracks, which will be analyzed in the following section.

6.2.2 2D track

In order to assess the quality of the reconstruction of the track cameras, we simulated 1000 horizontal muons crossing the test volume parallel to the camera at various distances, from 2 to 80 cm following a uniform distribution, and random origin range (-20, +20) cm on y and (-20, 0) on x , with (0,0) corresponding to the camera axis.
The simulated muons have random kinetic energy according to a Gaussian distribution with mean = 3 GeV and $\sigma = 0.5$ GeV. In this energy range, the muon is almost a minimum ionizing particle, and at 3 GeV energy it deposits an average of 2.52 MeV/cm [1].

To obtain an estimation of the reconstructed track width we calculate the reconstruction profile along the X axis and perform a Gaussian fit of it, and define the track width as twice the standard deviation of the resulting distribution.

To determine the track length instead, we first perform a cut on the background voxels: knowing from the fit of the previous profile the Y_0 coodinate of the track, we set to zero the amplitude of voxels whose center is located a distance greater than 2 sigma from Y_0. We then calculate the cumulative profile of voxels along the Y-axis, and determine as extremes of the trace the coordinates X_0 and X_1 at which the cumulative amplitude is higher than 0.6, normalized to (0,1), where 0 corresponds to the average value of the background we have previously excluded. Figure 6.6, shows two examples of reconstructed tracks, and on its right, the fit of the normalized profile to obtain the Y coordinates at which the particle has crossed the volume, while below the profile distribution to calculate the width of the track as described.

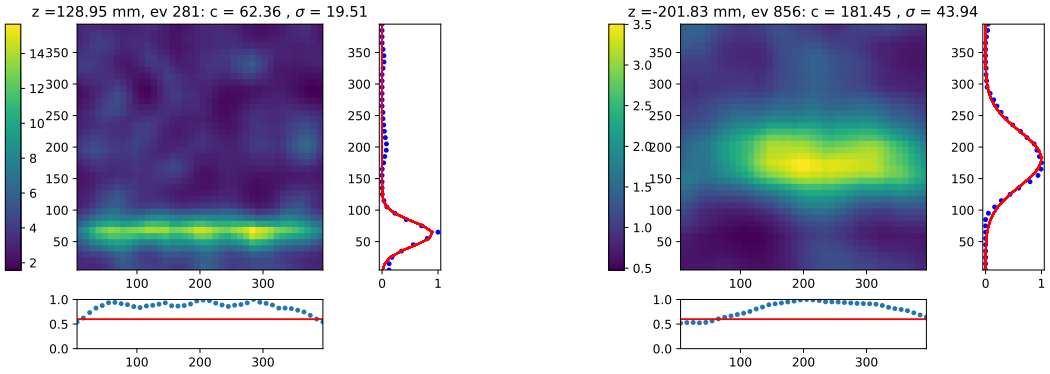

Figure 6.6: Two Reconstruction example of a horizontal minimum ionizing particle source at different positions and distances from camera A. On the right of the reconstructed image, the gaussian fit of the horizontal profile to obtain an estimate of the track width. Below, vertical profile of the image after removing the pixels corresponding to background: the start and end points of the reconstructed track are determined by the point where this distribution exceeds the 0.6 threshold on normalized values (marked by the red line).

For each camera, the distribution of the deviations between the reconstructed Y_0 position and the Monte Carlo truth is shown in Figure 6.7 (left). As can be seen, although camera C had better performance in reconstructing point sources, the error on the deviations of the reconstruction from the true position is greater than ± 5 cm, which means that the camera cannot reconstruct the tracks reliably. Because of this, camera

C is excluded from further analysis.

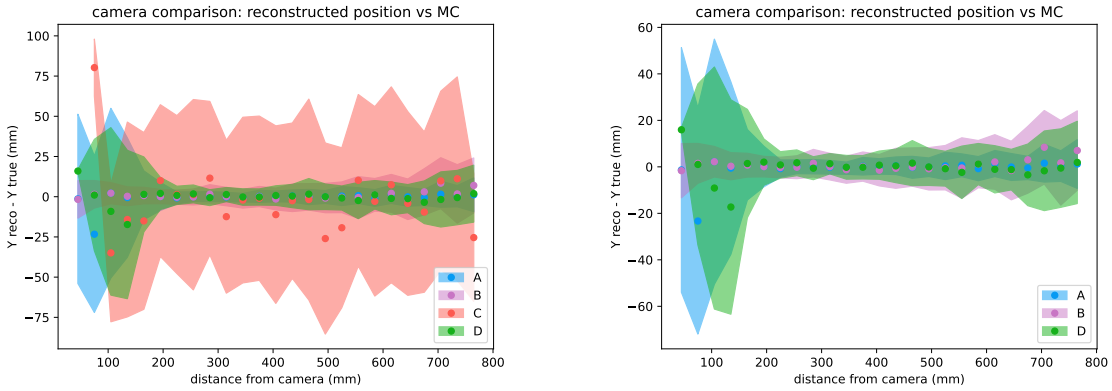

Figure 6.7: Distance between reconstructed track Y_0 position and MC truth as a function of track distance from camera, grouped in bins corresponding to 3 cm distance. The colored bands represent the range of $\pm 1\sigma$ of the values in the bin. Left: all cameras. Right: camera C exluded.

In figure 6.9 are shown, respectively, the average width of the μ track as a function of its distance from the camera, for all camera configurations under test.

Based on these simulations, we can conclude that the most suitable camera for (single) track reconstruction is configuration B. In fact, while the A, B, and D cameras have equivalent behavior in track reconstruction at distances greater than 25 cm, at closer distances, the A and D cameras, which have a wider field of view, have a standard deviation of about 5 cm on the distribution of the deviations between the reconstructed and the actual position. Similarly in this range of distances the width of the reconstructed track is on the order of 10 cm for these track cameras, indicating that the camera cannot reconstruct the track correctly.

The disadvantage of configuration B is that it has a narrower FCFV than the others, but unlike A and D, it succeeds in reconstructing even near tracks. We are less concerned about the narrowing of the length of the reconstructed trace as a function of distance, because on the scale of GRAIN size, the contribution of the cameras on the opposite wall will be relevant to improve the reconstruction. For tracks very close to a camera, it is important that the closest camera reconstructs well. We can also get around the narrow field of view of camera B by placing several cameras side by side thanks to its small size.

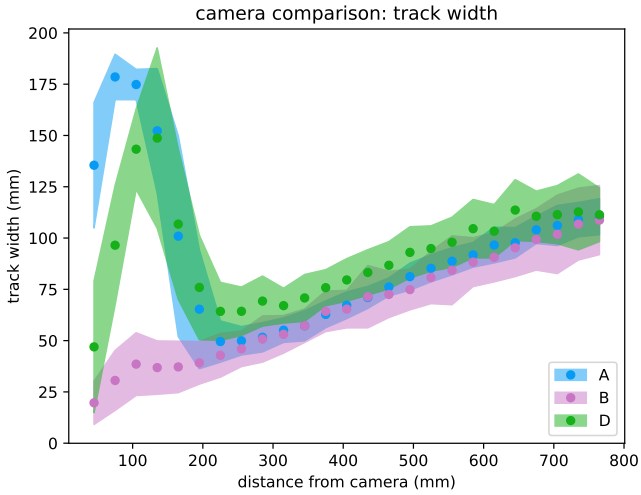

Figure 6.8: Track width as a function of track distance from camera, grouped in bins corresponding to 3 cm distance. The colored bands represent the range of $\pm 1\sigma$ of the values in the bin.

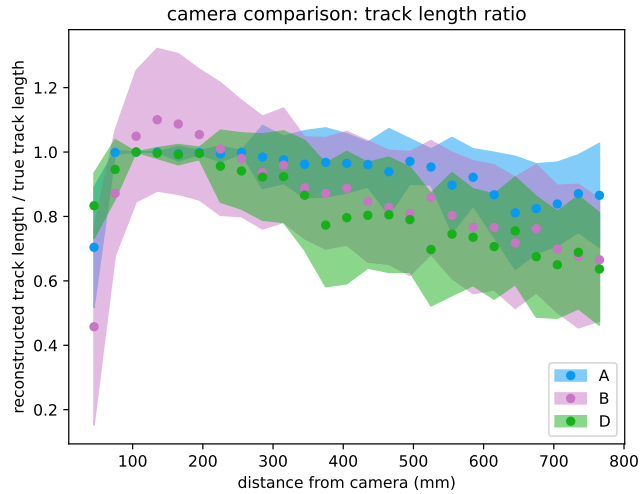

Figure 6.9: Ratio of reconstructed track length over true length as a function of track distance from camera, grouped in bins corresponding to 3 cm distance. The colored bands represent the range of $\pm 1\sigma$ of the values in the bin.

6.2.3 MURA and random mask pattern comparison

In the same way as in the previous section, we made the comparison between camera B and a camera with the same aperture size and distance between mask and sensor, but with a random hole pattern, as shown in Figure 6.10, generated with 50% of uncovered area.

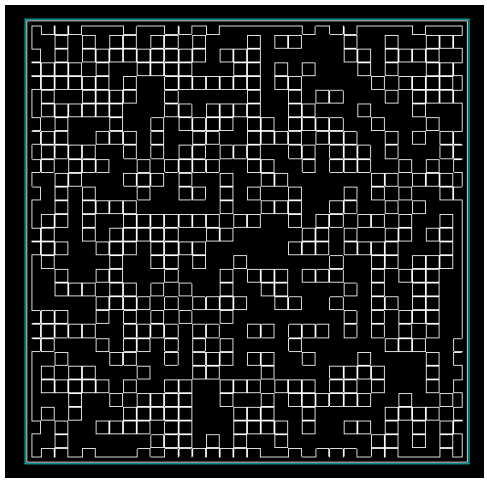

Figure 6.10: Camera geometry with random pattern mask. The pitch of the mask holes and their distance from the SiPM matrix are the same as for camera B.

The performance of the two cameras is comparable, as can be seen in the figures 6.11. Should it be necessary to use a matrix with a number of SiPMs for which a MURA pattern cannot be adapted (the rank of the matrix must be a prime number, cf. section 4.2.3), a random pattern is also suitable for use with this reconstruction algorithm.

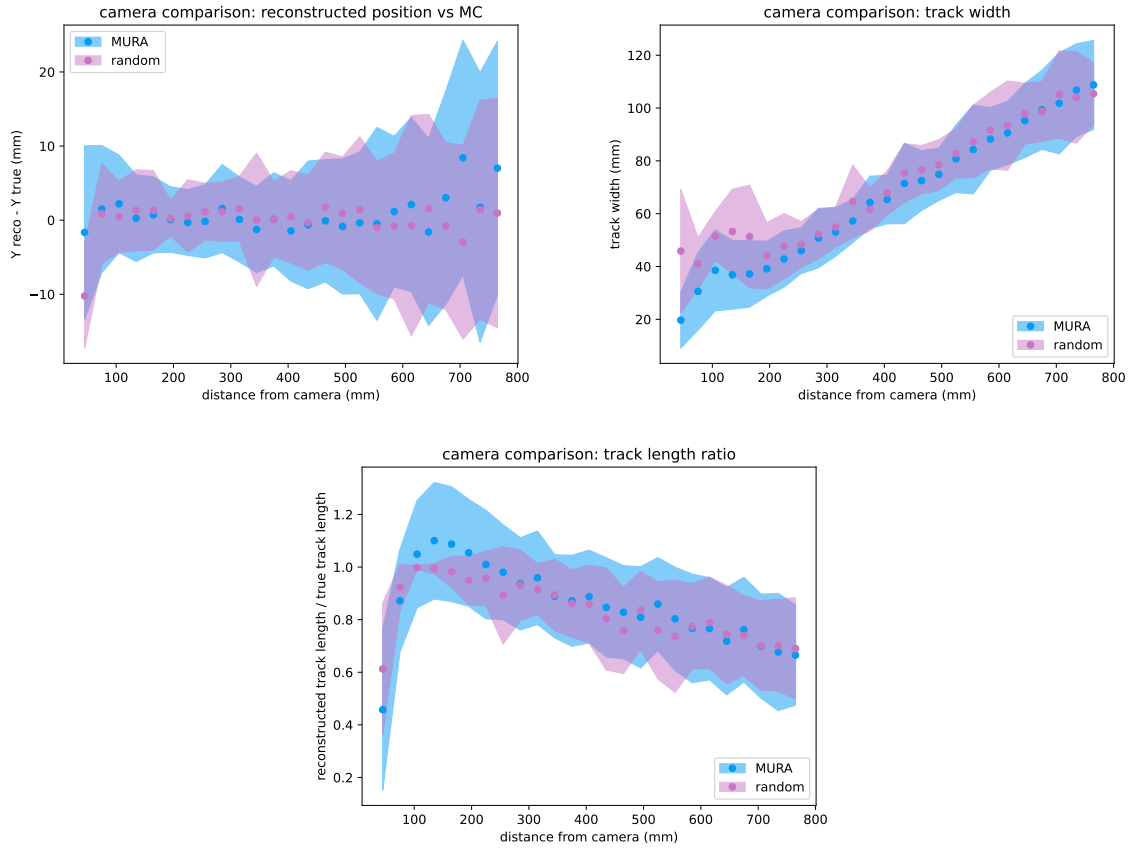

Figure 6.11: Reconstructed track position - MC truth, track width and track length ratio as a function of distance the camera, for camera (B) and a camera with a mask of equal dimensions, hole pitch, but a random hole pattern. Data is grouped in bins corresponding to 3 cm distance and the colored bands represent the range of $\pm 1\sigma$ of the values in the bin.

Chapter 7

3D event reconstruction in GRAIN

7.1 GRAIN optical system

Based on the considerations and results of the previous chapter, the best performing camera among those tested is camera B, with a MURA pattern and a mask-to-sensor distance of 20 mm. We implemented this camera configuration in the GRAIN geometry. In order to maximize the coverage of the elliptical side walls of GRAIN and with one row above and one below, as described in Section 3.2.4, a total of 54 cameras are assumed : 8 in the top and bottom rows, and 19 on each side. The cameras are 5 cm apart to leave enough space for a mechanical structure to support (and keep in tension to avoid deformations of) the masks, and they are 10 cm away from the GRAIN walls, leaving room for readout electronics and electrical connections. Figure 7.1 shows the geometry used in the simulations in the remainder of the chapter. The fiducial volume of the reconstruction is the entire volume of liquid argon, excluding the volume behind the cameras and the first 5 cm in front of them.

Given the small thickness occupied by a camera, it would be possible to place cameras on one of the curved GRAIN walls as well, particularly the downstream one, in order to improve the reconstruction of the vertex from the upstream side and to verify whether the detected particles are produced by neutrino interactions in argon or in the outer material of the detector. However, it must be considered that neutrino interaction products will have a forward boost and can directly cross a camera located on the downstream wall. Since in the space between mask and sensor there is Liquid argon, if scintillation light is then emitted within it, the light signal is no longer encoded by the mask and information is lost for reconstruction. We call the camera "dazzled" when this happens; in Figure 7.2 one can see a typical photon pattern on the sensor array, in which the particle has passed through both the camera volume and the sensor itself, compared to other cameras.

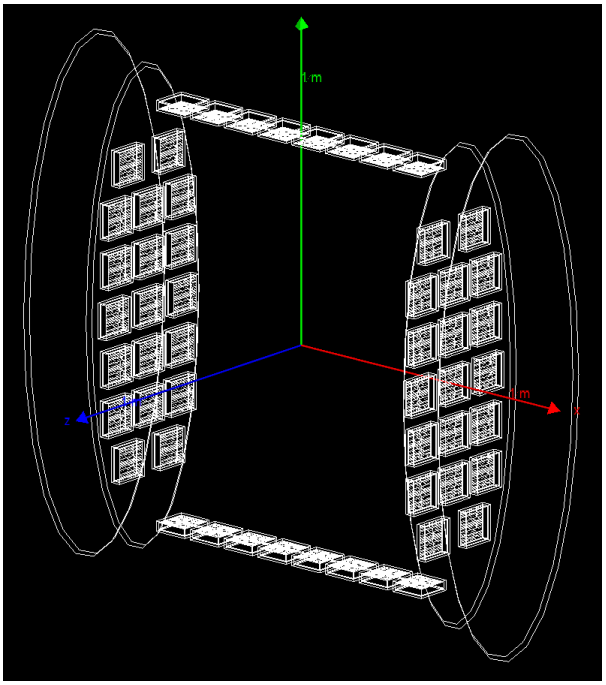

Figure 7.1: Camera (B) placement inside GRAIN volume, maximizing surface coverage of its elliptical side walls.

Cameras can be dazzled at any location, but in the other regions of GRAIN it happens less frequently than in the downstream region, where it would happen at almost every event.

In the simulations, the potentially dazzled cameras are currently identified using Monte Carlo truth, by verifying that there are no energy deposits inside the camera. We plan to develop a system for recognizing these cameras from the image formed on the SiPM matrix based on Convolutional Neural Networks, which are particularly well-suited for this kind of task. Within the reconstruction algorithm, dazzled cameras are currently excluded once recognized; it is the object of future work to look for a method to include their spatial information.

7.2 Voxel selection cuts

In the two-dimensional reconstructions performed so far, we did not perform any background removal in the images because the iterative process of the MLEM algorithm ensured a good contrast between the amplitude values of the voxels belonging to the sig-

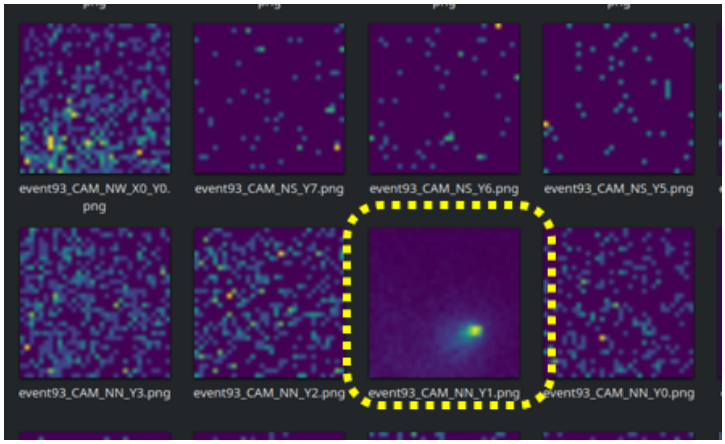

Figure 7.2: Example distributions of photon counts in a camera. Each pixel in the image corresponds to one SiPM in the sensor matrix. Highlighted in yellow is a "dazzled" camera where the particle passed through the sensor.

nal and those belonging to the background. As explained in section 5.1.3, due to memory constraints, we were unable to apply the algorithm simultaneously to the whole ensemble of cameras placed in the volume, but had to perform the reconstruction individually for each camera and to combine the results by taking the product of the amplitude values of the corresponding voxels. This simplification reduces the advantages of the iterative process of the MLEM algorithm, and the combination of reconstructions leads to a reduction of the overall contrast compared to a single camera reconstruction.
The resulting voxel amplitude distribution for a generic event is shown in the left panel of Fig. 7.3 for amplitudes $\lambda(x, y, z) > 0$. The true spatial distribution of the energy deposits is shown on the right panel of Fig. 7.3 instead.

It is clear that the output of the MLEM reconstruction algorithm with camera combination features a significant background, as most of the voxels have a nonzero amplitude. Moreover, as explained in Sect. 4.4.4, the voxel amplitude in a camera reconstruction is an estimation of the true number of photons emitted in that voxel, so characteristics of the voxel amplitude distribution, such as the maximum amplitude value, depend on the energy deposited in each voxel and differ between event and particle types. Example voxel amplitude distributions are shown in Fig. 7.4 for three different events. Therefore, it is necessary to devise a criterion for the discrimination of the reconstructed event from the combinatorial background.

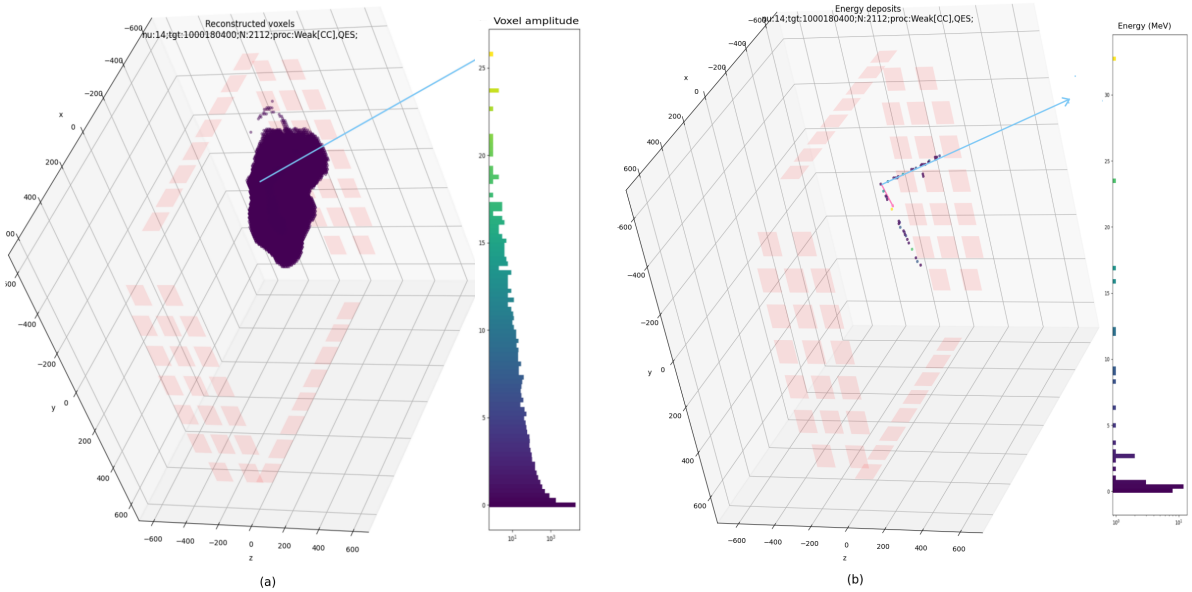

Figure 7.3: (a) Spatial amplitude distribution of a reconstruction. (b) Spatial distribution the true Monte Carlo energy deposits

7.2.1 Histogram equalization

One of the simplest improvements that can be applied is a transformation to increase the contrast between the signal and background voxels. A simple technique widely used for this purpose in image analysis is histogram equalization. For an image, this method maps the observed pixel gray values to new values so that the new image has a uniform gray-level histogram. We can apply a similar transformation to voxel amplitude values to obtain a uniform voxel amplitude spectrum.
Let $f(i,j,k)$ be a reconstruction represented as a three-dimensional matrix of voxel amplitudes normalized in the interval [0,1]. The normalized histogram of f with 1/(B-1) amplitude levels and B bins is defined as [112]:

$$p_b = \frac{N_{selected}}{N_{total}} \qquad b = 0, 1, ..., B-1. \tag{7.1}$$

where $N_{selected}$ is the number of voxels with intensity $> (b-1)(1/B-1)$ and $< b(1/B-1)$, and N_{total} is the total number of voxels.

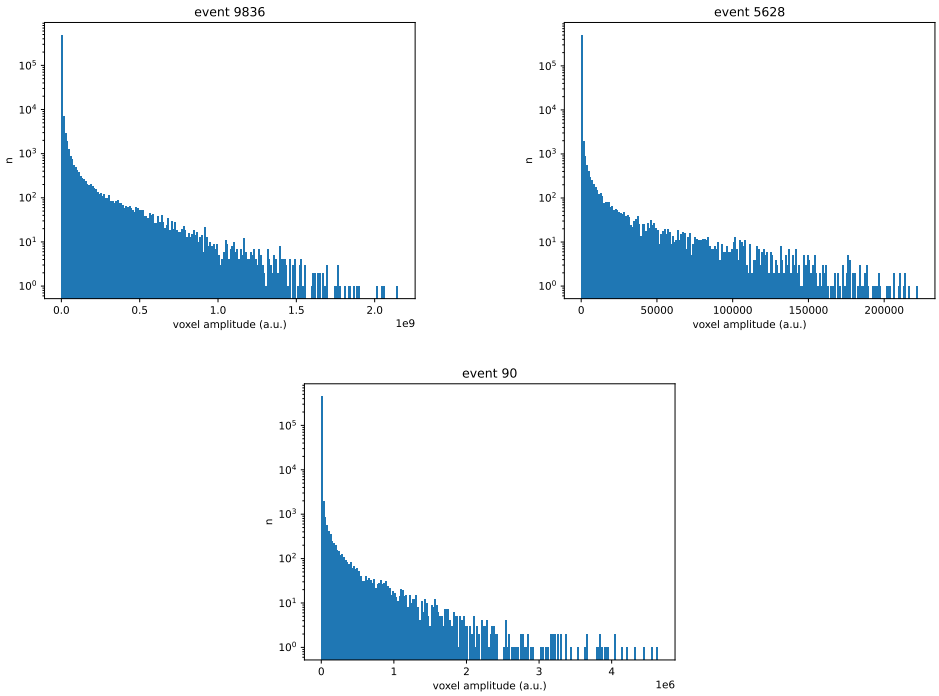

Figure 7.4: Amplitude spectrum of three example events. While the distributions of the values are similar, the scale of the amplitudes is different for each event and depends on the total number of photons detected and the combination of the cameras.

The histogram equalized reconstruction g will be defined by:

$$g_{i,j,k} = (B-1)\sum_{n=0}^{f_{i,j,k}} p_b \tag{7.2}$$

This is equivalent to transforming the voxel intensities, h, of f by the function

$$T(h) = (B-1)\sum_{n=0}^{h} p_b. \tag{7.3}$$

Figure 7.5 shows the distribution of the voxel amplitudes of a reconstructed event before and after histogram equalization. This method is particularly useful when reconstruction artifacts are present, especially voxels reconstructed with an amplitude value significantly different from the average amplitude of the other voxels, as shown in Fig. 7.5(left panel). These artifacts prevent the possibility of selecting signal pixels simply

by making a cut on voxel amplitudes relative to the maximum amplitude. By contrast, histogram equalization narrows the amplitude gap between the artifact voxels and the remaining distribution, and the voxel amplitude spectrum is made uniform. It is then possible to apply a cutoff on the maximum amplitude of the normalized and equalized voxels: we empirically determined that a threshold between 0.8 and 0.9 yields the best results in terms of the number of voxels preserved along the direction of the tracks of Monte Carlo truth.

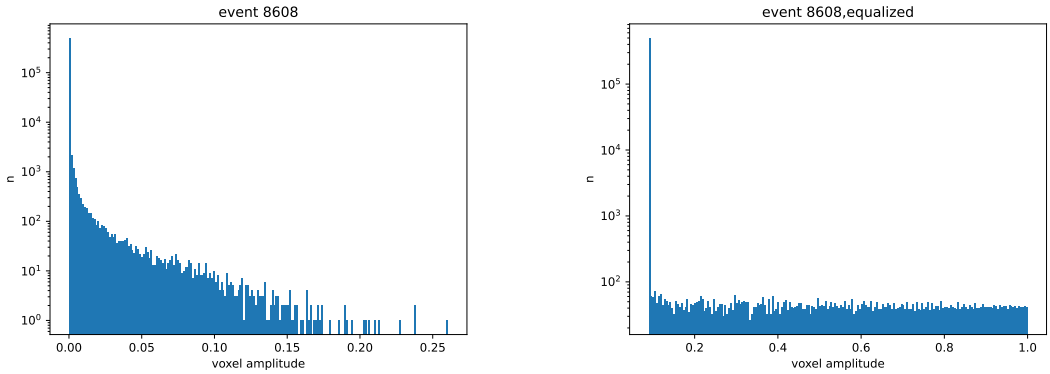

Figure 7.5: Example voxel amplitude distribution (left) and its equalization (right). After equalization, the voxel distribution is uniform.

7.3 Muon tracks

To verify the capabilities of the selected camera to reconstruct tracks of minimum ionizing particles, we simulated muon events crossing GRAIN volume along the beam direction. We simulated 100 muon events with a random energy extracted from a Gaussian with a mean of 3 GeV and sigma of 1 GeV, and the origin at a random position in the z = -50 cm plane and an angle of $[-20°, +20°]$ with respect to the X-Y plane and $[-30°, +30°]$ with respect to the Y-Z plane. This distribution is reasonable because it represents the angular distribution of the muons produced by typical CCQE events in GRAIN. For reconstruction, we applied a cutoff on voxel amplitudes as described in the previous section, with a threshold at 90% of the normalized maximum.
Two example reconstructed tracks are shown in Fig. 7.6. As can be seen, the selected voxels are arranged approximately symmetrically around the direction of the particle, with the amplitude value of the voxels being higher the closer they are to the point through which the particle passed.

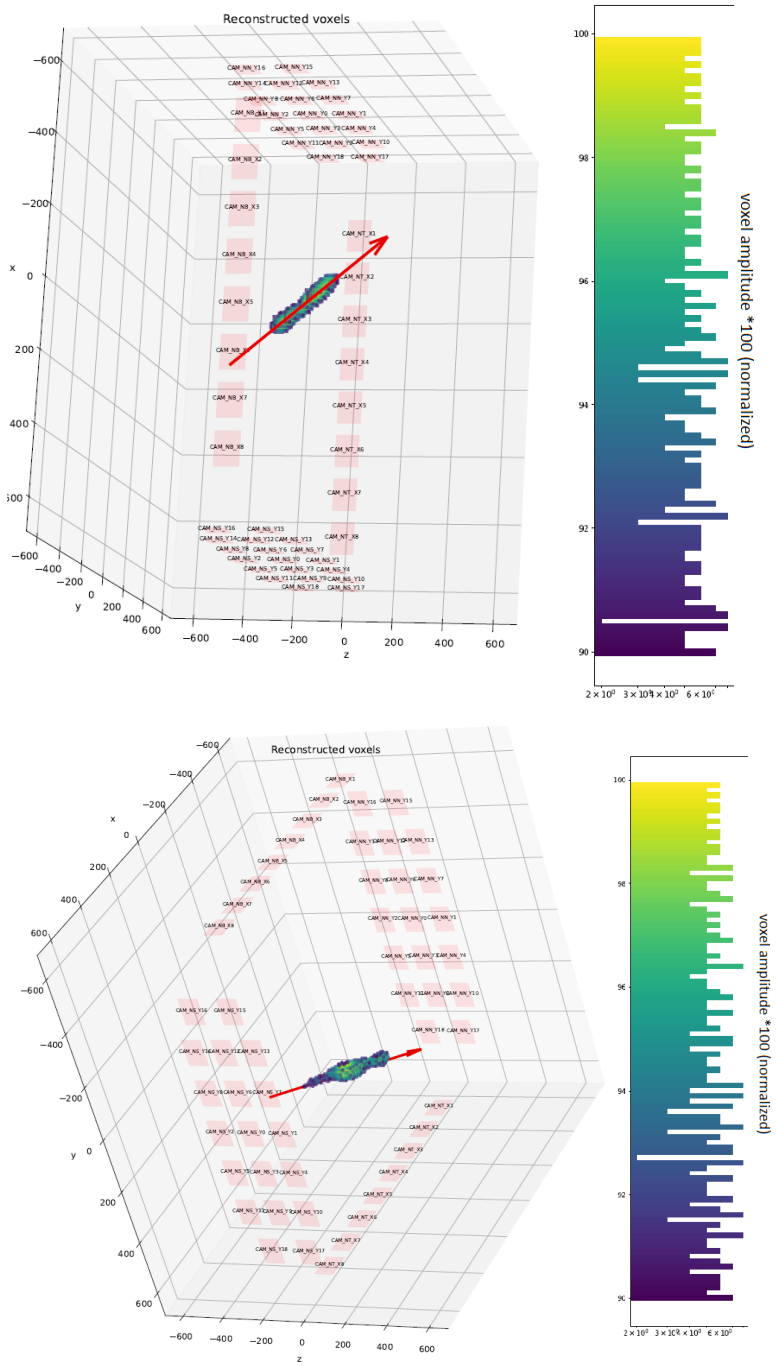

Figure 7.6: Two simulated muon events crossing the GRAIN volume with random direction and origin. Voxels with amplitudes greater than 90% of the maximum are shown, after histogram normalization of the voxel amplitude distribution, as described in sect. 7.2.1. Shown with the red arrow is the direction of the simulated muon according to the Monte Carlo truth.

We can estimate the direction, length, and width of the reconstructed track by performing Principal Component Analysis (PCA) [113], applied to the centers of the voxels of the clusters preserved after cutting. The first principal component represents the length and direction of the track, while the second and third components represent the width of the reconstructed track in the directions orthogonal to the direction of the particle.
This technique can only be used with straight tracks, and GRAIN will actually be immersed in a magnetic field, so, although limited in the small thickness of GRAIN, the tracks will have curvature. Furthermore, PCA is not weighted by the amplitude value of the voxels, so the results of PCA are closely related to the chosen cutoff criterion on the voxels. Regardless, PCA is a robust technique and can be implemented effectively within the scope of this work.

In order to verify the correctness of the track reconstruction, we defined as figures of merit:

- the minimum distance between the first principal component (indicating the reconstructed track's direction) and the simulated particle's true direction;
- the angle between these two when projected onto the X-Z and Y-Z planes.

As shown in Fig. 7.7, the minimum distance between the reconstructed line and the simulated particle track is at most $\sim$ 13 mm, which is a little more than one voxel distance, with a mean value of 3.6 ± 2.8 mm. Figure 7.8 shows the distribution of the angle between the reconstructed direction of the particle, and the true direction of the track, respectively on the XZ plane and the YZ plane. The distributions are centered around 0°, as expected. There is a slight bias toward negative angles in the X-Z plane, caused by only partially reconstructed tracks. We have performed a Gaussian fit on the distributions, and obtained a resolution on the reconstructed angle, corresponding to one standard deviation of the Gaussian, of $2.7^\circ \pm 0.7^\circ$ on the X-Z plane and $3.2^\circ \pm 0.7^\circ$ on the Y-Z plane.

In Fig. 7.9 the distribution of the mean widths along the second and third components, and the ratio of the reconstructed track length to the actual length in volume are displayed. It can be seen that the mean width of the reconstructed tracks is 53.1 ± 7.6 mm, as expected from the results of the tracks reconstructed with a single camera at distances > 50 cm. The track length is considerably reduced compared to the original size, even compared to single camera reconstructions. This suggests that the subsequent combination of single-camera reconstructions is a limitation that, although it allows for the correct detection of portions of the track, needs to be overcome by implementing the algorithm globally on all cameras to obtain a correct reconstruction.

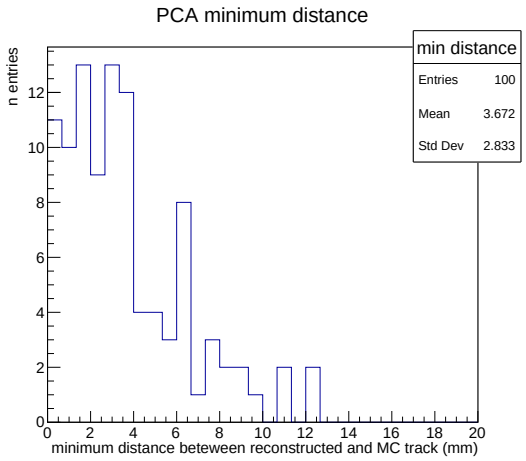

Figure 7.7: Minimum distances distribution between the reconstructed track's direction and the simulated particle's true direction.

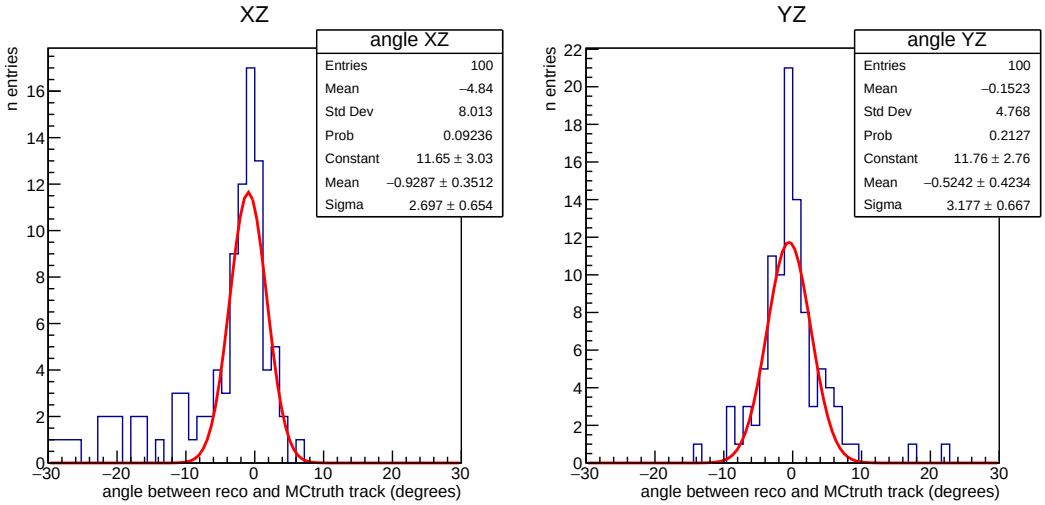

Figure 7.8: Angle distribution between the reconstructed direction of the particle and the true track direction, on the XZ (left) and YZ (right) plane respectively.

As mentioned earlier, PCA does not take into account the amplitude values of the voxels, which, as can be seen in figure 7.6, have a higher value the closer they are to the point where the track passes. There are other algorithms that allow points to be extracted from clusters of voxels, weighted according to the amplitude value associated with each voxel. In the future, after proper implementation of the camera combination

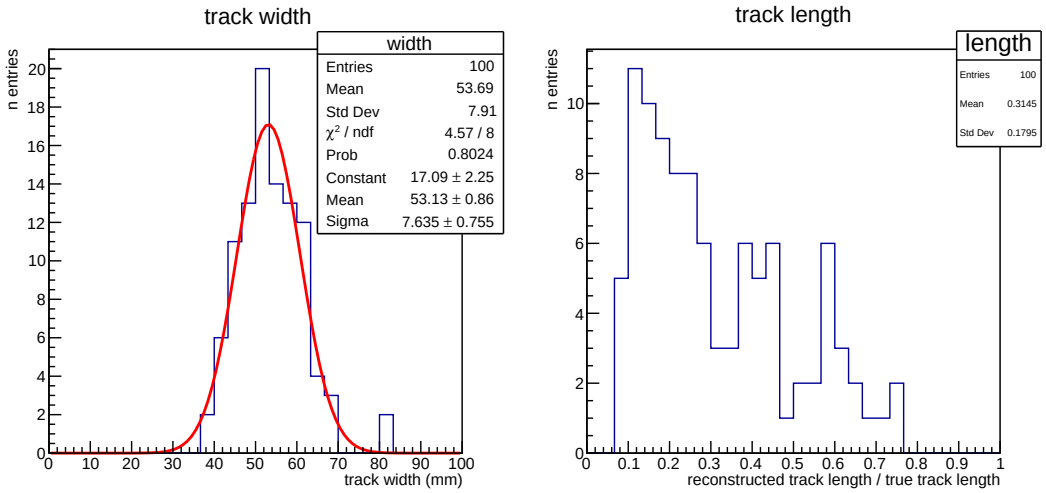

Figure 7.9: Left: track width distribution, computed as twice the mean length of the second and third principal component. On average, a voxel cluster reconstructing the track is 53.13 ± 7.64 mm wide. Right: Ratio of the length of the reconstructed track, computed as twice the length of the first principal component, over the true track length in Argon.

in the reconstruction, it might be of interest to study the possibility of applying one of such algorithms. For example, for automated track and shower detection of neutrino interactions in a liquid argon time projection chamber, the *local principal curves* (LPC) algorithm has been successfully implemented in three dimensions [114], and it appears to be an interesting option to apply it also in the case of our Coded Aperture Imaging system reconstruction.

7.4 Neutrino CCQE events

We tested the reconstruction capabilities of the imaging system in GRAIN by reconstructing muon-neutrino charged current quasi-elastic (CCQE) events:

$$\nu_\mu + n \rightarrow \mu + p \tag{7.4}$$

which have a simple two-track topology involving a short proton track and a long muon track originating from a common primary vertex point, with variable opening angle.
We have performed the reconstruction of 110 events using Edep-sim simulated energy deposition within the entire SAND detector.The selected events have interaction vertices

within the fiducial volume of GRAIN, excluding the last 10 cm of thickness along the beam direction to ensure that tracks of at least 10 cm length are obtained within the volume of GRAIN. Of these 203 events, we excluded from the sample events with one or more dazzled cameras (62) and events with tracks that could not be reconstructed because they were completely outside the fiducial volume of the optical system reconstruction (31).

In Fig. 7.10, the GRAIN volume region where the interacting vertices were selected is marked.

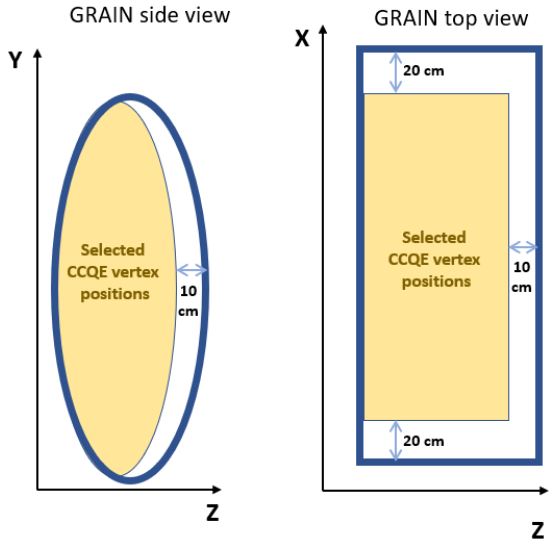

Figure 7.10: Regions in GRAIN where the vertexes of CCQE events were selected for the simulation.

Some reconstructed events are displayed in Figs. 7.11 7.12, alongside the energy deposits generated by Edep-sim. It's worth mentioning that the event reconstruction will be gathered not only from GRAIN, but also from other SAND detector components and particles that release limited energy in GRAIN may emerge from the Argon target and detected by the STT. Therefore, it is crucial to accurately reconstruct the particles that are produced and stopped within GRAIN, such as the proton in this instance. It can be seen in fact that while the proton is always at least partially visible in the reconstruction, for the muon this is not always the case. This is due to the fact that the proton has a higher average $\frac{dE}{dx}$ than the muon in the argon and therefore produces more photons. The presence of the brighter track often almost completely prevents the reconstruction of the muon, since the number of photons arriving at the sensor from the

scintillation caused by the muon is only a fraction of the total light arriving from the two tracks, and is easily confused with the statistical fluctuations from the other track introduced by the Poisson nature of the process.

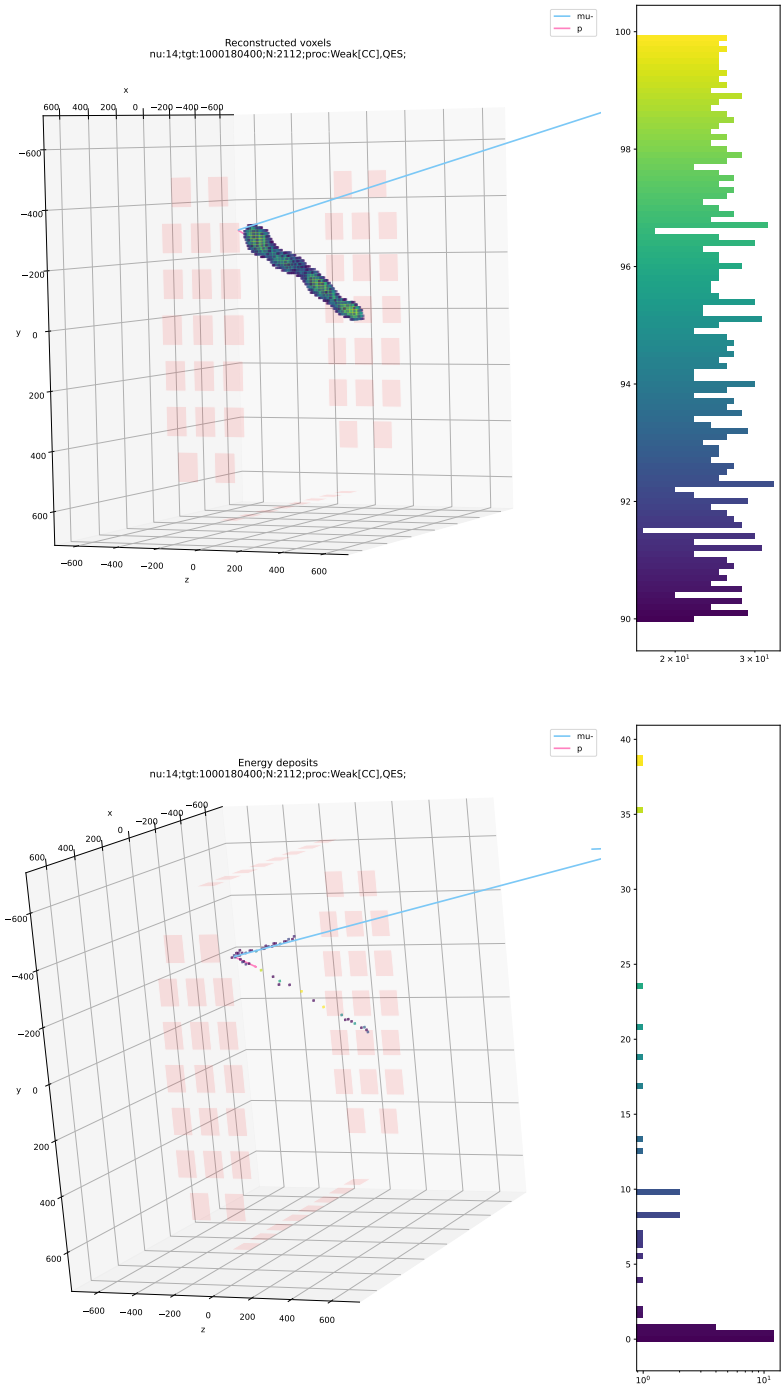

Figure 7.11: Top: Example reconstructed CCQE event. The proton track is fully reconstructed but the muon track is not visible. The amplitude values of the selected voxels in the reconstruction are shown in the histogram on the right.Bottom: deposited energy distribution in the volume, as generated by Edep-sim.

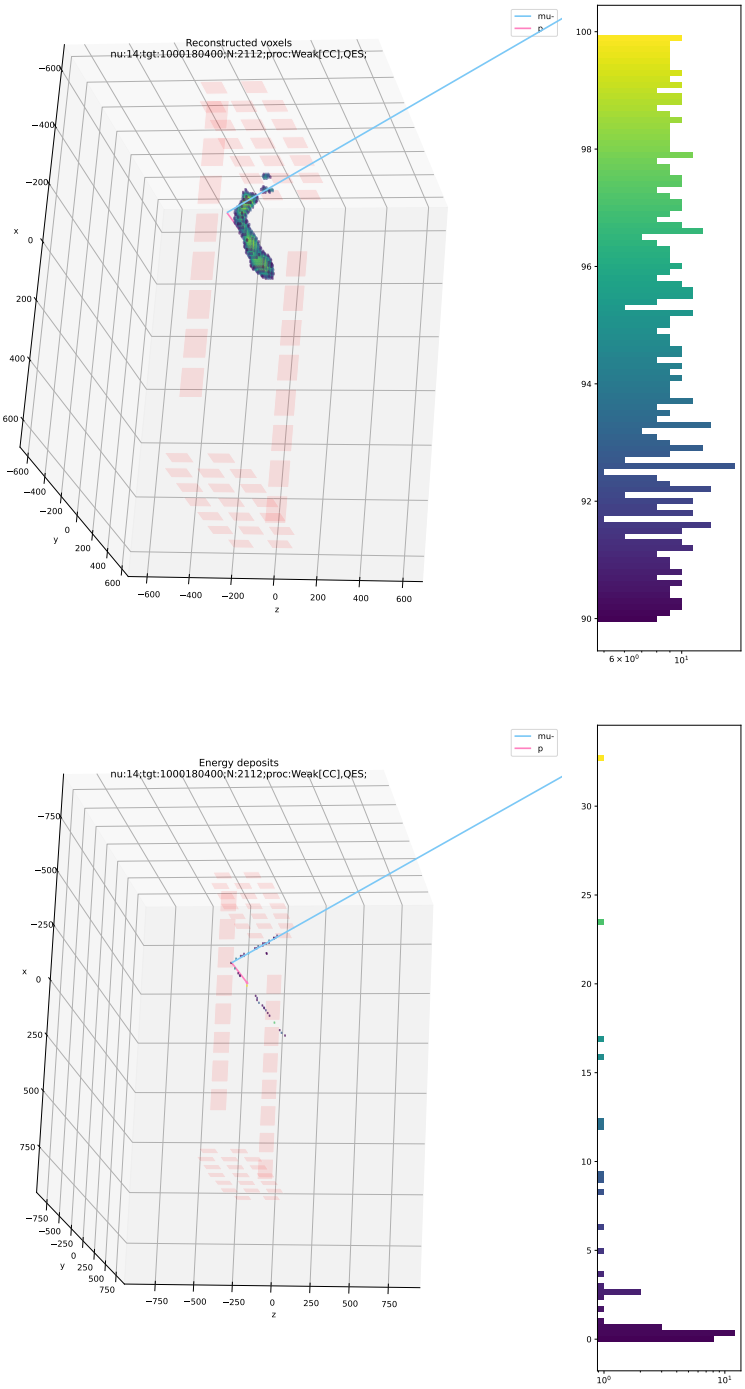

Figure 7.12: Top: Example reconstructed CCQE event. Both the proton track and the muon tracks are partially reconstructed. The amplitude values of the selected voxels in the reconstruction are shown in the histogram on the right. Bottom: deposited energy distribution in the volume, as generated by Edep-sim. The histogram on the right represents the distribution of energy deposited in the particle in the GRAIN volume.

7.4.1 Proton Track fitting

Tracks reconstructed by the Straw Tube Tracker next to GRAIN, can be extrapolated to the Argon volume and associated to voxels selected by the reconstruction. After that, it is possible to detect clusters of voxels not connected to any track in the STT and thus identify the possible presence of particles that did not leave the liquid argon volume.
Since there is currently no integration of the STT reconstructions with those of the GRAIN imaging system, we used the Monte Carlo truth to identify the muon track in argon and associate the corresponding reconstruction voxels with it. We considered the reconstructed voxels belonging to the muon whose center is less than 6 cm from the muon track direction. This distance was chosen taking into account the average width of the muon tracks that were reconstructed in the 7.3 section. The reconstructed voxels not associated with the μ track are then considered to belong to the proton. Figure 7.13 shows the reconstruction of the proton track and part of the μ track. The voxels associated with the track based on the distance from the actual muon direction are shown in blue.

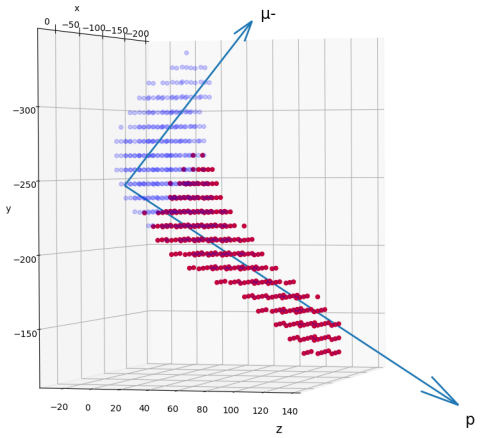

Figure 7.13: Example of voxel clustering when both tracks are reconstructed. Each dot corresponds to a voxel center, represented in blue are the voxel associated with the muon track, in red with the proton track.

Once the voxels belonging to the proton track were identified, we applied the Principal Component Analysis to obtain the direction of the track. Fig. 7.14 shows the angle between the reconstructed track and the Monte Carlo truth and Fig. 7.15 the minimum distance between the track directions.

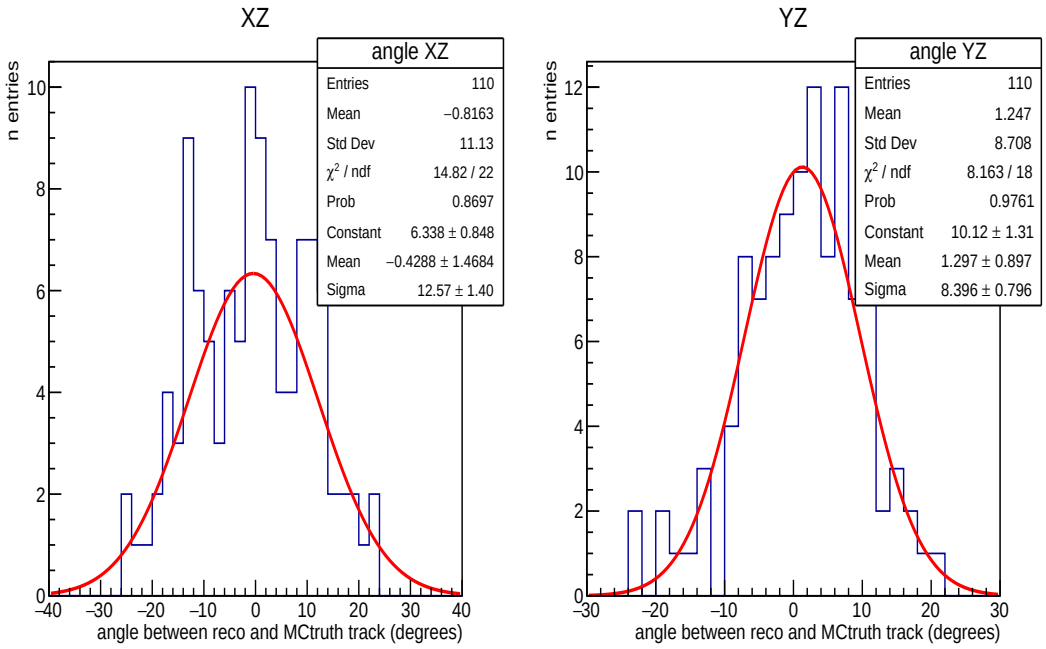

Figure 7.14: Angle distribution between the reconstructed direction of the muon and the true track direction, on the XZ (left) and YZ (right) plane respectively.

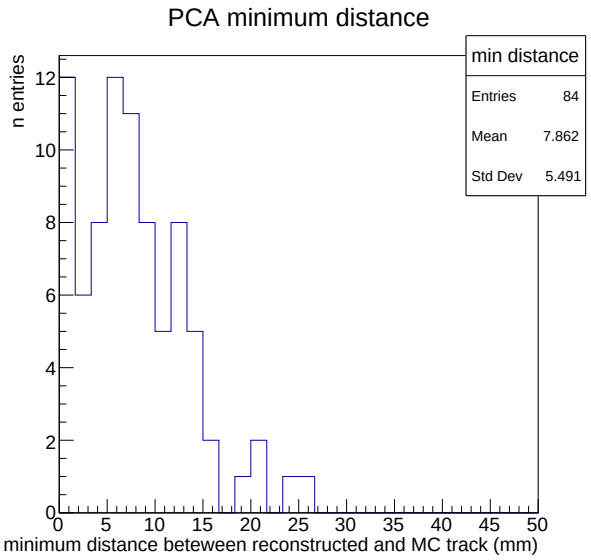

Figure 7.15: Minimum distances distribution between the reconstructed proton track's direction and the simulated particle's true direction.

7.4.2 Vertex position estimation

Using the fit of the proton track, we estimate the position of the neutrino interaction vertex where it intersects the muon track known from the Monte Carlo Truth (STT). We define the interacting vertex as the midpoint of the segment where the distance between the two tracks is minimized. Figure 7.16 shows the distributions of the distance between the reconstructed primary vertex position and the MC truth in X, Y and Z directions. The distributions are fitted to Gaussian functions and the resolution of the vertex position in each coordinate direction is taken to be the standard deviation of the corresponding Gaussian fit. The vertex positions in X and Y are centered around zero, with a standard deviation of 13.2 and 9.9 mm, respectively. In Z, however, the reconstruction appears to be biased at -20.6 mm, with a standard deviation of 12.4 mm. This bias is due to the coarse cut made during the voxel assignment process: As can be observed in Fig. 7.13, some of the voxels upstream of the proton track are also assigned to the muon. As illustrated by Fig. 7.17 approximately 90% of the selected events have a primary vertex found within 3.5 cm from the generated position.

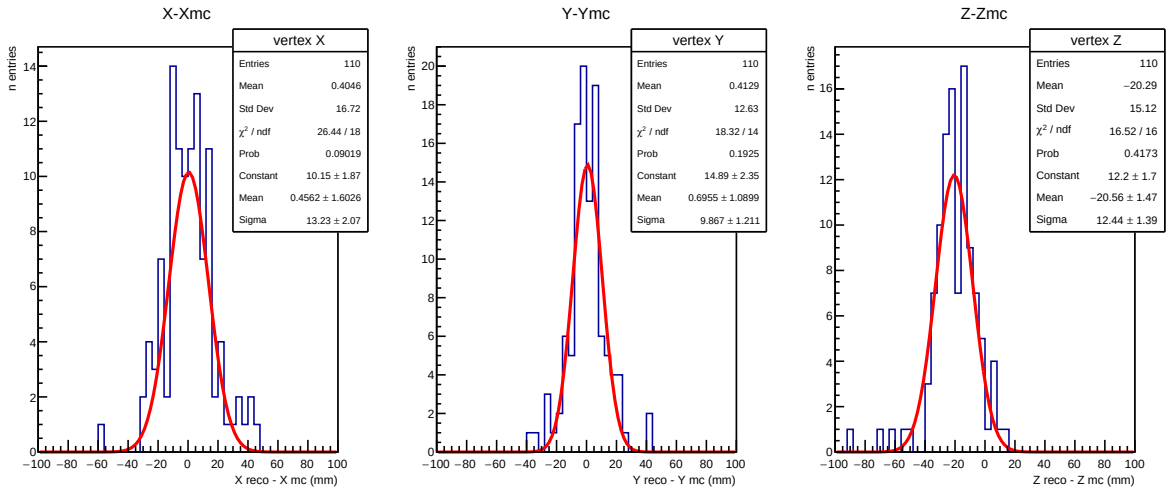

Figure 7.16: Gaussian fits to the distributions of the reconstructed primary vertex position in x, y and z for muon-proton events.

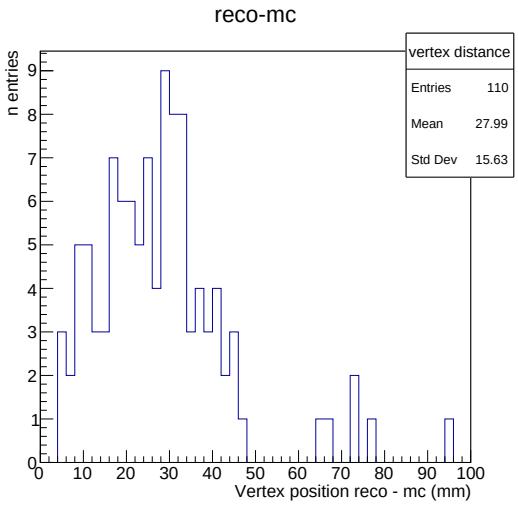

Figure 7.17: The distribution of the distance of the reconstructed primary vertex position from the generated position for muon-proton events. Approximately 90% of these events have a primary vertex found within 3.5 cm from the true vertex position.

Conclusions

The GRAIN detector, a component of the SAND apparatus of the DUNE ND complex, will play an important role in the characterization of the neutrino beam and the improvement of LAr interaction models. GRAIN employs an innovative high-performance optical reconstruction technique in order to achieve high granularity and a fast time response to contribute to the SAND physics case.
In this work, we have developed an imaging system based on Coded Aperture Masks that exploits Argon scintillation light to detect tracks associated to charged particles. A reconstruction algorithm based on Maximum Likelihood Expectation Maximization was implemented, which allows us to directly obtain a three-dimensional voxel distribution proportional to the energy deposited by charged particles passing through the LAr volume. The implemented algorithm was used to evaluate reconstructions of point sources and tracks of minimum ionizing particles with different camera configurations with different sizes and patterns of the coded aperture mask. The best-performing type was selected, and a multi-camera optical system design was proposed to be implemented in the GRAIN geometry.
An assessment was then made of the capability of GRAIN when equipped with this camera system to reconstruct muon tracks, and CCQE neutrino events with production of a muon and a proton. This assessment is of particular interest since GRAIN can complement the information provided by the tracker and ECAL of SAND when ν interaction products, e.g. a proton, stop in the LAr volume. For muons and other minimum ionizing particles the reconstructed track direction matches with Monte Carlo truth with an angular residual of $< 2.7^\circ$ on the XZ plane and $< 3.1^\circ$ on the YZ plane, with an average minimum distance between them of 3.7 ± 2.8 mm. On the other hand, when reconstructing CCQE events, it may happen that muon tracks are not reconstructed if the proton track is brighter. This limitation is due to the fact that it is not possible to implement the algorithm to perform the reconstruction globally using information from all cameras. This is because the matrix of weights describing the system far exceeds the available computer memory. Either by implementing a more memory efficient version of the algorithm or by a computer system with more memory, we plan to address these

limitations in future work.
In reconstructing the event we assumed that the direction of the muon, as reconstructed by the SAND tracking system, is known. This allowed us to correctly assign the voxel clusters of the reconstruction to the corresponding particle. We have quantified the error in reconstructing the direction of the proton: the distribution of the angle between the reconstructed direction of the track and the Monte Carlo truth has a standard deviation of $12.6^\circ \pm 1.4^\circ$ on the XZ plane and $8.4^\circ \pm 0.8^\circ$ on the YZ plane. A preliminary estimate of the resolution of the vertex reconstruction has been made from the analyzed events, which leads to a residual between reconstructed and true position < 13 mm in the three directions. Overall, this work has demonstrated that a Coded Aperture-based imaging system is feasible in GRAIN. As the algorithm improves, GRAIN, along with the rest of SAND, will be able to provide reconstructed samples of $\nu-$Ar interactions that will be essential for the constraining of the systematics for DUNE and for its long baseline oscillation analysis.

Bibliography

[1] Particle Data Group, R L Workman, V D Burkert, et al. "Review of Particle Physics". In: *Progress of Theoretical and Experimental Physics* 2022.8 (Aug. 2022). 083C01. ISSN: 2050-3911. DOI: 10.1093/ptep/ptac097. eprint: https://academic.oup.com/ptep/article-pdf/2022/8/083C01/45434166/ptac097.pdf. URL: https://doi.org/10.1093/ptep/ptac097.

[2] Carlo Giunti and Chung W. Kim. *Fundamentals of Neutrino Physics and Astrophysics*. Oxford University Press, Mar. 2007. ISBN: 9780198508717. DOI: 10.1093/acprof:oso/9780198508717.001.0001. URL: https://doi.org/10.1093/acprof:oso/9780198508717.001.0001.

[3] Chris Quigg. *Gauge Theories of the Strong, Weak, and Electromagnetic Interactions: Second Edition*. USA: Princeton University Press, Sept. 2013. ISBN: 978-0-691-13548-9, 978-1-4008-4822-5.

[4] M. Aker, K. Altenmüller, M. Arenz, et al. "Improved Upper Limit on the Neutrino Mass from a Direct Kinematic Method by KATRIN". In: *Phys. Rev. Lett.* 123 (22 Nov. 2019), p. 221802. DOI: 10.1103/PhysRevLett.123.221802. URL: https://link.aps.org/doi/10.1103/PhysRevLett.123.221802.

[5] A. Monfardini et al. "The microcalorimeter arrays for a rhenium experiment (MARE): A next-generation calorimetric neutrino mass experiment". In: *Nuclear Instruments and Methods in Physics Research Section A: Accelerators, Spectrometers, Detectors and Associated Equipment* 559.2 (2006). Proceedings of the 11th International Workshop on Low Temperature Detectors, pp. 346–348. ISSN: 0168-9002. DOI: https://doi.org/10.1016/j.nima.2005.12.006. URL: https://www.sciencedirect.com/science/article/pii/S0168900205023922.

[6] Guofu Cao. "Search for $0\nu\beta\beta$ decay with EXO-200 and nEXO". In: *Proceedings of XIV International Conference on Heavy Quarks and Leptons — PoS(HQL2018)*. Vol. 332. 2018, p. 054. DOI: 10.22323/1.332.0054.

[7] Felix Boehm and Petr Vogel. *Physics of massive neutrinos*. Cambridge University Press, 1992.

[8] H Ohsumi and (forthe NEMO Collaboration). "NEMO 3 double beta decay experiment". In: *Journal of Physics: Conference Series* 120.5 (July 2008), p. 052047. DOI: 10.1088/1742-6596/120/5/052047. URL: https://dx.doi.org/10.1088/1742-6596/120/5/052047.

[9] Irene Nutini, D. Adams, C. Alduino, et al. "The CUORE Detector and Results". In: *Journal of Low Temperature Physics* 199 (Apr. 2020). DOI: 10.1007/s10909-020-02402-9.

[10] M. Gunther et al. "Heidelberg - Moscow beta-beta experiment with Ge-76: Full setup with five detectors". In: *Phys. Rev. D* 55 (1997), pp. 54–67. DOI: 10.1103/PhysRevD.55.54.

[11] A. Bettini. "GERDA. Germanium Detector Array. Search for Neutrino-less Decay of 76Ge". In: *Nuclear Physics B - Proceedings Supplements* 168 (2007). Proceedings of the Neutrino Oscillation Workshop, pp. 67–69. ISSN: 0920-5632. DOI: https://doi.org/10.1016/j.nuclphysbps.2007.02.018. URL: https://www.sciencedirect.com/science/article/pii/S0920563207001144.

[12] A. Gando, Y. Gando, T. Hachiya, et al. "Search for Majorana Neutrinos Near the Inverted Mass Hierarchy Region with KamLAND-Zen". In: *Phys. Rev. Lett.* 117 (8 Aug. 2016), p. 082503. DOI: 10.1103/PhysRevLett.117.082503. URL: https://link.aps.org/doi/10.1103/PhysRevLett.117.082503.

[13] Planck Collaboration, Aghanim, N., Akrami, Y., et al. "Planck 2018 results - VI. Cosmological parameters". In: *A&A* 641 (2020), A6. DOI: 10.1051/0004-6361/201833910. URL: https://doi.org/10.1051/0004-6361/201833910.

[14] E. Grohs, G. M. Fuller, C. T. Kishimoto, et al. "Neutrino energy transport in weak decoupling and big bang nucleosynthesis". In: *Phys. Rev. D* 93 (8 Apr. 2016), p. 083522. DOI: 10.1103/PhysRevD.93.083522. URL: https://link.aps.org/doi/10.1103/PhysRevD.93.083522.

[15] Shadab Alam, Marie Aubert, Santiago Avila, et al. "Completed SDSS-IV extended Baryon Oscillation Spectroscopic Survey: Cosmological implications from two decades of spectroscopic surveys at the Apache Point Observatory". In: *Phys. Rev. D* 103 (8 Apr. 2021), p. 083533. DOI: 10.1103/PhysRevD.103.083533. URL: https://link.aps.org/doi/10.1103/PhysRevD.103.083533.

[16] Kevork Abazajian, Arwa Abdulghafour, Graeme E. Addison, et al. *Snowmass 2021 CMB-S4 White Paper*. 2022. DOI: 10.48550/ARXIV.2203.08024. URL: https://arxiv.org/abs/2203.08024.

[17] B. Pontecorvo. "Neutrino Experiments and the Problem of Conservation of Leptonic Charge". In: *Zh. Eksp. Teor. Fiz.* 53 (1967), pp. 1717–1725.

[18] B. Pontecorvo. "Mesonium and anti-mesonium". In: *Sov. Phys. JETP* 6 (1957), p. 429.

[19] L. Wolfenstein. "Neutrino oscillations in matter". In: *Phys. Rev. D* 17 (9 May 1978), pp. 2369–2374. DOI: 10.1103/PhysRevD.17.2369. URL: https://link.aps.org/doi/10.1103/PhysRevD.17.2369.

[20] John N. Bahcall, Walter F. Huebner, Stephen H. Lubow, et al. "Standard solar models and the uncertainties in predicted capture rates of solar neutrinos". In: *Rev. Mod. Phys.* 54 (3 July 1982), pp. 767–799. DOI: 10.1103/RevModPhys.54.767. URL: https://link.aps.org/doi/10.1103/RevModPhys.54.767.

[21] Aldo Serenelli. "Alive and well: A short review about standard solar models". In: *The European Physical Journal A* 52.4 (Apr. 2016), p. 78. ISSN: 1434-601X. DOI: 10.1140/epja/i2016-16078-1. URL: https://doi.org/10.1140/epja/i2016-16078-1.

[22] P. Anselmann, W. Hampel, G. Heusser, et al. "Solar neutrinos observed by GALLEX at Gran Sasso". In: *Nuclear Physics B - Proceedings Supplements* 31 (1993), pp. 117–124. ISSN: 0920-5632. DOI: https://doi.org/10.1016/0920-5632(93)90122-M. URL: https://www.sciencedirect.com/science/article/pii/092056329390122M.

[23] M. Altmann, M. Balata, P. Belli, et al. "Complete results for five years of GNO solar neutrino observations". In: *Physics Letters B* 616.3 (2005), pp. 174–190. ISSN: 0370-2693. DOI: https://doi.org/10.1016/j.physletb.2005.04.068. URL: https://www.sciencedirect.com/science/article/pii/S0370269305005149.

[24] V.N. Gavrin, J.N. Abdurashitovi, T.J. Bowles, et al. "Solar neutrino results from SAGE". In: *Nuclear Physics B - Proceedings Supplements* 91.1 (2001). Neutrino 2000, pp. 36–43. ISSN: 0920-5632. DOI: https://doi.org/10.1016/S0920-5632(00)00920-8. URL: https://www.sciencedirect.com/science/article/pii/S0920563200009208.

[25] K. S. Hirata, T. Kajita, T. Kifune, et al. "Observation of ^{8}B solar neutrinos in the Kamiokande-II detector". In: *Phys. Rev. Lett.* 63 (1 July 1989), pp. 16–19. DOI: 10.1103/PhysRevLett.63.16. URL: https://link.aps.org/doi/10.1103/PhysRevLett.63.16.

[26] Y. Fukuda, T. Hayakawa, E. Ichihara, et al. "Measurements of the Solar Neutrino Flux from Super-Kamiokande's First 300 Days". In: *Phys. Rev. Lett.* 81 (6 Aug. 1998), pp. 1158–1162. DOI: 10.1103/PhysRevLett.81.1158. URL: https://link.aps.org/doi/10.1103/PhysRevLett.81.1158.

[27] A. Bellerive, J.R. Klein, A.B. McDonald, et al. "The Sudbury Neutrino Observatory". In: *Nuclear Physics B* 908 (2016). Neutrino Oscillations: Celebrating the Nobel Prize in Physics 2015, pp. 30–51. ISSN: 0550-3213. DOI: https://doi.org/10.1016/j.nuclphysb.2016.04.035. URL: https://www.sciencedirect.com/science/article/pii/S0550321316300736.

[28] D. Casper, R. Becker-Szendy, C. B. Bratton, et al. "Measurement of atmospheric neutrino composition with the IMB-3 detector". In: *Phys. Rev. Lett.* 66 (20 May 1991), pp. 2561–2564. DOI: 10.1103/PhysRevLett.66.2561. URL: https://link.aps.org/doi/10.1103/PhysRevLett.66.2561.

[29] Y. Fukuda, T. Hayakawa, E. Ichihara, et al. "Evidence for Oscillation of Atmospheric Neutrinos". In: *Phys. Rev. Lett.* 81 (8 Aug. 1998), pp. 1562–1567. DOI: 10.1103/PhysRevLett.81.1562. URL: https://link.aps.org/doi/10.1103/PhysRevLett.81.1562.

[30] M. Sanchez, W. W. M. Allison, G. J. Alner, et al. "Measurement of the L/E distributions of atmospheric ν in Soudan 2 and their interpretation as neutrino oscillations". In: *Phys. Rev. D* 68 (11 Dec. 2003), p. 113004. DOI: 10.1103/PhysRevD.68.113004. URL: https://link.aps.org/doi/10.1103/PhysRevD.68.113004.

[31] M Ambrosio et al. "Measurement of the atmospheric neutrino-induced upgoing muon flux using MACRO". In: *Physics Letters B* 434.3 (1998), pp. 451–457. ISSN: 0370-2693. DOI: https://doi.org/10.1016/S0370-2693(98)00885-5. URL: https://www.sciencedirect.com/science/article/pii/S0370269398008855.

[32] M. H. Ahn, E. Aliu, S. Andringa, et al. "Measurement of neutrino oscillation by the K2K experiment". In: *Phys. Rev. D* 74 (7 Oct. 2006), p. 072003. DOI: 10.1103/PhysRevD.74.072003. URL: https://link.aps.org/doi/10.1103/PhysRevD.74.072003.

[33] N. Agafonova, A. Alexandrov, A. Anokhina, et al. "Final Results of the OPERA Experiment on ν_τ Appearance in the CNGS Neutrino Beam". In: *Phys. Rev. Lett.* 120 (21 May 2018), p. 211801. DOI: 10.1103/PhysRevLett.120.211801. URL: https://link.aps.org/doi/10.1103/PhysRevLett.120.211801.

[34] K. Abe, J. Adam, H. Aihara, et al. "Observation of Electron Neutrino Appearance in a Muon Neutrino Beam". In: *Phys. Rev. Lett.* 112 (6 Feb. 2014), p. 061802. DOI: 10.1103/PhysRevLett.112.061802. URL: https://link.aps.org/doi/10.1103/PhysRevLett.112.061802.

[35] M. A. Acero et al. "First Measurement of Neutrino Oscillation Parameters using Neutrinos and Antineutrinos by NOvA". In: *Phys. Rev. Lett.* 123.15 (2019), p. 151803. DOI: 10.1103/PhysRevLett.123.151803. arXiv: 1906.04907 [hep-ex].

[36] Kamiokande Collaboration, K. Abe, P. Adrich, et al. *The Hyper-Kamiokande Experiment – Snowmass LOI.* 2020. DOI: 10.48550/ARXIV.2009.00794. URL: https://arxiv.org/abs/2009.00794.

[37] A. Aguilar, L. B. Auerbach, R. L. Burman, et al. "Evidence for neutrino oscillations from the observation of $\overline{\nu}_e$ appearance in a $\overline{\nu}_\mu$ beam". In: *Phys. Rev. D* 64 (11 Nov. 2001), p. 112007. DOI: 10.1103/PhysRevD.64.112007. URL: https://link.aps.org/doi/10.1103/PhysRevD.64.112007.

[38] A. A. Aguilar-Arevalo, B. C. Brown, J. M. Conrad, et al. "Updated MiniBooNE neutrino oscillation results with increased data and new background studies". In: *Phys. Rev. D* 103 (5 Mar. 2021), p. 052002. DOI: 10.1103/PhysRevD.103.052002. URL: https://link.aps.org/doi/10.1103/PhysRevD.103.052002.

[39] S. Ajimura et al. "Technical Design Report (TDR): Searching for a Sterile Neutrino at J-PARC MLF (E56, JSNS2)". In: (May 2017). arXiv: 1705.08629 [physics.ins-det].

[40] Pedro A.N. Machado, Ornella Palamara, and David W. Schmitz. "The Short-Baseline Neutrino Program at Fermilab". In: *Annual Review of Nuclear and Particle Science* 69.1 (2019), pp. 363–387. DOI: 10.1146/annurev-nucl-101917-020949. eprint: https://doi.org/10.1146/annurev-nucl-101917-020949. URL: https://doi.org/10.1146/annurev-nucl-101917-020949.

[41] M.P. Decowski. "KamLAND's precision neutrino oscillation measurements". In: *Nuclear Physics B* 908 (2016). Neutrino Oscillations: Celebrating the Nobel Prize in Physics 2015, pp. 52–61. ISSN: 0550-3213. DOI: https://doi.org/10.1016/j.nuclphysb.2016.04.014. URL: https://www.sciencedirect.com/science/article/pii/S0550321316300529.

[42] B. Aharmim, S. N. Ahmed, A. E. Anthony, et al. "Combined analysis of all three phases of solar neutrino data from the Sudbury Neutrino Observatory". In: *Phys. Rev. C* 88 (2 Aug. 2013), p. 025501. DOI: 10.1103/PhysRevC.88.025501. URL: https://link.aps.org/doi/10.1103/PhysRevC.88.025501.

[43] F. Ardellier et al. "Double Chooz: A Search for the neutrino mixing angle theta(13)". In: (June 2006). arXiv: hep-ex/0606025.

[44] Xinheng Guo et al. "A Precision measurement of the neutrino mixing angle θ_{13} using reactor antineutrinos at Daya-Bay". In: (Jan. 2007). arXiv: hep-ex/0701029.

[45] J. K. Ahn et al. "RENO: An Experiment for Neutrino Oscillation Parameter θ_{13} Using Reactor Neutrinos at Yonggwang". In: (Mar. 2010). arXiv: 1003.1391 [hep-ex].

[46] K. Abe, R. Akutsu, A. Ali, et al. "Constraint on the matter–antimatter symmetry-violating phase in neutrino oscillations". In: *Nature* 580.7803 (Apr. 2020), pp. 339–344. ISSN: 1476-4687. DOI: 10.1038/s41586-020-2177-0. URL: https://doi.org/10.1038/s41586-020-2177-0.

[47] Maria Concepcion Gonzalez-Garcia, Michele Maltoni, and Thomas Schwetz. "NuFIT: Three-Flavour Global Analyses of Neutrino Oscillation Experiments". In: *Universe* 7.12 (2021). ISSN: 2218-1997. DOI: 10.3390/universe7120459. URL: https://www.mdpi.com/2218-1997/7/12/459.

[48] Blair Jamieson. "Future Neutrino Experiments". In: *20th Conference on Flavor Physics and CP Violation*. July 2022. arXiv: 2207.05044 [hep-ex].

[49] Lino Miramonti. "Neutrino Physics and Astrophysics with the JUNO Detector". In: *Universe* 4.11 (2018). ISSN: 2218-1997. DOI: 10.3390/universe4110126. URL: https://www.mdpi.com/2218-1997/4/11/126.

[50] K. Joo. "New results from RENO prospects with RENO-50". In: *Journal of Physics: Conference Series* 888 (Sept. 2017), p. 012012. DOI: 10.1088/1742-6596/888/1/012012.

[51] Babak Abi et al. "Deep Underground Neutrino Experiment (DUNE), Far Detector Technical Design Report, Volume II: DUNE Physics". In: (Feb. 2020). arXiv: 2002.03005 [hep-ex].

[52] M. G. Aartsen et al. "PINGU: A Vision for Neutrino and Particle Physics at the South Pole". In: *J. Phys. G* 44.5 (2017), p. 054006. DOI: 10.1088/1361-6471/44/5/054006. arXiv: 1607.02671 [hep-ex].

[53] Piotr Kalaczyński. "KM3NeT/ORCA: status and perspectives for neutrino oscillation and mass hierarchy measurements". In: *PoS* ICHEP2020 (2021), p. 149. DOI: 10.22323/1.390.0149. arXiv: 2107.10593 [hep-ex].

[54] "JUNO physics and detector". In: *Progress in Particle and Nuclear Physics* 123 (2022), p. 103927. ISSN: 0146-6410. DOI: https://doi.org/10.1016/j.ppnp.2021.103927. URL: https://www.sciencedirect.com/science/article/pii/S0146641021000880.

[55] Ko Abe et al. "Proposal for an Extended Run of T2K to 20 × 10^{21} POT". In: (Sept. 2016). arXiv: 1609.04111 [hep-ex].

[56] K. Abe, N. Akhlaq, R. Akutsu, et al. "Improved constraints on neutrino mixing from the T2K experiment with 3.13 × 10^{21} protons on target". In: *Phys. Rev. D* 103 (11 June 2021), p. 112008. DOI: 10.1103/PhysRevD.103.112008. URL: https://link.aps.org/doi/10.1103/PhysRevD.103.112008.

[57] Sergei Nagaitsev and Valeri Lebedev. "A Cost-Effective Upgrade Path for the Fermilab Accelerator Complex". In: (Nov. 2021). arXiv: 2111.06932 [physics.acc-ph].

[58] A. Abed Abud et al. "Snowmass Neutrino Frontier: DUNE Physics Summary". In: (Mar. 2022). arXiv: 2203.06100 [hep-ex].

[59] H. -Th. Janka. "Neutrino Emission from Supernovae". In: (Feb. 2017). DOI: 10.1007/978-3-319-21846-5_4. arXiv: 1702.08713 [astro-ph.HE].

[60] B. Abi, R. Acciarri, M. A. Acero, et al. "Prospects for beyond the Standard Model physics searches at the Deep Underground Neutrino Experiment". In: *The European Physical Journal C* 81.4 (Apr. 2021), p. 322. ISSN: 1434-6052. DOI: 10.1140/epjc/s10052-021-09007-w. URL: https://doi.org/10.1140/epjc/s10052-021-09007-w.

[61] Kaustubh Agashe, Yanou Cui, Lina Necib, et al. "(In)direct detection of boosted dark matter". In: *Journal of Cosmology and Astroparticle Physics* 2014.10 (Oct. 2014), p. 062. DOI: 10.1088/1475-7516/2014/10/062. URL: https://dx.doi.org/10.1088/1475-7516/2014/10/062.

[62] Animesh Chatterjee, Albert De Roeck, Doojin Kim, et al. "Searching for boosted dark matter at ProtoDUNE". In: *Phys. Rev. D* 98 (7 Oct. 2018), p. 075027. DOI: 10.1103/PhysRevD.98.075027. URL: https://link.aps.org/doi/10.1103/PhysRevD.98.075027.

[63] R. Acciarri et al. "Long-Baseline Neutrino Facility (LBNF) and Deep Underground Neutrino Experiment (DUNE): Conceptual Design Report, Volume 2: The Physics Program for DUNE at LBNF". In: (Dec. 2015). arXiv: 1512.06148 [physics.ins-det].

[64] B. Abi, R. Acciarri, Mario A. Acero, et al. *Deep Underground Neutrino Experiment (DUNE), Far Detector Technical Design Report, Volume IV: Far Detector Single-phase Technology*. 2020. DOI: 10.48550/ARXIV.2002.03010. URL: https://arxiv.org/abs/2002.03010.

[65] Sabrina Sacerdoti. "A LArTPC with Vertical Drift for the DUNE Far Detector". In: *PoS* NuFact2021 (2022), p. 173. DOI: 10.22323/1.402.0173.

[66] Adam Abed Abud et al. "Deep Underground Neutrino Experiment (DUNE) Near Detector Conceptual Design Report". In: *Instruments* 5.4 (2021), p. 31. DOI: 10.3390/instruments5040031. arXiv: 2103.13910 [physics.ins-det].

[67] A. Abed Abud, B. Abi, R. Acciarri, et al. *Deep Underground Neutrino Experiment (DUNE) Near Detector Conceptual Design Report*. 2021. DOI: 10.48550/ARXIV.2103.13910. URL: https://arxiv.org/abs/2103.13910.

[68] G.Adamov et Al. *A proposal to enhance the DUNE Near-Detector Complex*. May 2021.

[69] M Adinolfi, F Ambrosino, A Antonelli, et al. "The KLOE electromagnetic calorimeter". In: *Nuclear Instruments and Methods in Physics Research Section A: Accelerators, Spectrometers, Detectors and Associated Equipment* 482.1 (2002), pp. 364–386. ISSN: 0168-9002. DOI: https://doi.org/10.1016/S0168-9002(01)01502-9. URL: https://www.sciencedirect.com/science/article/pii/S0168900201015029.

[70] V. Pia. "Study of the calorimetric performance of a liquid Argon detector based on a novel optical imaging concept". PhD thesis. 2023.

[71] Ettore Segreto. "Properties of liquid argon scintillation light emission". In: *Phys. Rev. D* 103 (4 Feb. 2021), p. 043001. DOI: 10.1103/PhysRevD.103.043001. URL: https://link.aps.org/doi/10.1103/PhysRevD.103.043001.

[72] T. Heindl, T. Dandl, M. Hofmann, et al. "The scintillation of liquid argon". In: *Europhysics Letters* 91.6 (Oct. 2010), p. 62002. DOI: 10.1209/0295-5075/91/62002. URL: https://dx.doi.org/10.1209/0295-5075/91/62002.

[73] Ori Cheshnovsky, Baruch Raz, and Joshua Jortner. "Emission Spectra of Deep Impurity States in Solid and Liquid Rare Gas Alloys". In: *Journal of Chemical Physics* 57 (1972), pp. 4628–4632.

[74] B J P Jones, C S Chiu, J M Conrad, et al. "A measurement of the absorption of liquid argon scintillation light by dissolved nitrogen at the part-per-million level". In: *Journal of Instrumentation* 8.07 (July 2013), P07011. DOI: 10.1088/1748-0221/8/07/P07011. URL: https://dx.doi.org/10.1088/1748-0221/8/07/P07011.

[75] M. Babicz, S. Bordoni, A. Fava, et al. "A measurement of the group velocity of scintillation light in liquid argon". In: *Journal of Instrumentation* 15.09 (Sept. 2020), P09009. DOI: 10.1088/1748-0221/15/09/P09009. URL: https://dx.doi.org/10.1088/1748-0221/15/09/P09009.

[76] A. Neumeier, T. Dandl, T. Heindl, et al. "Intense vacuum ultraviolet and infrared scintillation of liquid Ar-Xe mixtures". In: *Europhysics Letters* 109.1 (Jan. 2015), p. 12001. DOI: 10.1209/0295-5075/109/12001. URL: https://dx.doi.org/10.1209/0295-5075/109/12001.

[77] V. M. Gehman, S. R. Seibert, K. Rielage, et al. "Fluorescence Efficiency and Visible Re-emission Spectrum of Tetraphenyl Butadiene Films at Extreme Ultraviolet Wavelengths". In: *Nucl. Instrum. Meth. A* 654 (2011), pp. 116–121. DOI: 10.1016/j.nima.2011.06.088. arXiv: 1104.3259 [astro-ph.IM].

[78] Hamamatsu Photonics. *MPPC S14160-3050HS*. URL: https://www.hamamatsu.com/jp/en/product/optical-sensors/mppc/mppc_mppc-array/S14160-3050HS.html (visited on 01/11/2022).

[79] R. H. Dicke. "Scatter-Hole Cameras for X-Rays and Gamma Rays". In: 153 (Aug. 1968), p. L101. DOI: 10.1086/180230.

[80] J. G. Ables. "Fourier transform photography: a new method for X-ray astronomy". In: 1 (Dec. 1968), p. 172. DOI: 10.1017/S1323358000011292.

[81] E. Caroli et al. "Coded Aperture Imaging in X-Ray and Gamma-Ray Astronomy". In: 45.3-4 (Sept. 1987), pp. 349–403. DOI: 10.1007/BF00171998.

[82] G. K. Skinner. "Coding (and decoding) coded mask telescopes". In: *Experimental Astronomy* 6.4 (Dec. 1995), pp. 1–7. ISSN: 1572-9508. DOI: 10.1007/BF00419252. URL: https://doi.org/10.1007/BF00419252.

[83] J. Gunson and B. Polychronopoulos. In: *Monthly Notices Roy. Astron. Soc.* 177 (1976).

[84] Edward E Fenimore and Thomas M Cannon. "Coded aperture imaging with uniformly redundant arrays". In: *Applied optics* 17.3 (1978), pp. 337–347.

[85] Stephen Gottesman and E Fenimore. "New family of binary arrays for coded aperture imaging". In: *Applied optics* 28 (Oct. 1989), pp. 4344–52. DOI: 10.1364/AO.28.004344.

[86] Valerio Pia. *Study of a novel VUV-imaging system in liquid argon for neutrino oscillation experiments*. URL: http://amslaurea.unibo.it/18798/.

[87] R. Willingale, M.R. Sims, and M.J.L. Turner. "Advanced deconvolution techniques for coded aperture imaging". In: *Nuclear Instruments and Methods in Physics Research* 221.1 (1984). Proceedings of the International Workshop on X- and -Ray Imaging Techniques, pp. 60–66. ISSN: 0167-5087. DOI: https://doi.org/10.1016/0167-5087(84)90180-7. URL: https://www.sciencedirect.com/science/article/pii/0167508784901807.

[88] Mark Rayner Sims. "A wide field camera for x-ray astronomy". PhD thesis. University of Leicester, UK, Jan. 1981.

[89] E. E. Fenimore. "Time-resolved and energy-resolved coded aperture images with URAtagging". In: *Appl. Opt.* 26.14 (July 1987), pp. 2760–2769. DOI: 10.1364/AO.26.002760. URL: https://opg.optica.org/ao/abstract.cfm?URI=ao-26-14-2760.

[90] G.K. Skinner and M.R. Nottingham. "Analysis of data from coded-mask telescopes by maximum likelihood". In: *Nuclear Instruments and Methods in Physics Research Section A: Accelerators, Spectrometers, Detectors and Associated Equipment* 333.2 (1993), pp. 540–547. ISSN: 0168-9002. DOI: https://doi.org/10.1016/0168-9002(93)91205-2. URL: https://www.sciencedirect.com/science/article/pii/0168900293912052.

[91] Truman P. Kohman. "Coded-aperture X- or gamma-ray telescope with least-squares image reconstruction. I - Design considerations. II - Computer simulation". In: *Review of Scientific Instruments* 60 (Nov. 1989), pp. 3396–3420. DOI: 10.1063/1.1140536.

[92] Ludwig Strauss and George Kontaxakis. "Maximum Likelihood Algorithms for Image Reconstruction in Positron Emission Tomography". In: *Radionuclides Oncol* (June 1998).

[93] Y. Vardi, Lawrence Shepp, and Linda Kaufman. "A Statistical Model for Positron Emission Tomography". In: *JASA. Journal of the American Statistical Association* 80 (Mar. 1985). DOI: 10.2307/2288030.

[94] Willard I Zangwill. *Nonlinear programming: a unified approach*. Vol. 52. Prentice-Hall Englewood Cliffs, NJ, 1969.

[95] D.W. Wilson and B.M.W. Tsui. "Noise properties of filtered-backprojection and ML-EM reconstructed emission tomographic images". In: *IEEE Transactions on Nuclear Science* 40.4 (1993), pp. 1198–1203. DOI: 10.1109/23.256736.

[96] L. A. Shepp et al. "Maximum Likelihood PET with Real Data". In: *IEEE Transactions on Nuclear Science* 31.2 (1984), pp. 910–913. DOI: 10.1109/TNS.1984.4333398.

[97] C.-T. Chen et al. "Sensor fusion in image reconstruction". In: *IEEE Transactions on Nuclear Science* 38.2 (1991), pp. 687–692. DOI: 10.1109/23.289375.

[98] M. Kelbert, I. Sazonov, and A.G. Wright. "Exact expression for the variance of the photon emission process in scintillation counters". In: *Nuclear Instruments and Methods in Physics Research Section A: Accelerators, Spectrometers, Detectors and Associated Equipment* 564.1 (2006), pp. 185–189. ISSN: 0168-9002. DOI: https://doi.org/10.1016/j.nima.2006.04.049. URL: https://www.sciencedirect.com/science/article/pii/S0168900206006930.

[99] A. Iriarte et al. "System models for PET statistical iterative reconstruction: A review". In: *Computerized Medical Imaging and Graphics* 48 (2016), pp. 30–48. ISSN: 0895-6111. DOI: https://doi.org/10.1016/j.compmedimag.2015.12.003. URL: https://www.sciencedirect.com/science/article/pii/S0895611115001901.

[100] Stefan Gundacker and Arjan Heering. "The silicon photomultiplier: fundamentals and applications of a modern solid-state photon detector". In: *Physics in Medicine Biology* 65.17 (Aug. 2020), 17TR01. DOI: 10.1088/1361-6560/ab7b2d. URL: https://dx.doi.org/10.1088/1361-6560/ab7b2d.

[101] P. Nakarmi et al. "Reflectivity and PDE of VUV4 Hamamatsu SiPMs in liquid xenon". In: *Journal of Instrumentation* 15.01 (Jan. 2020), P01019. DOI: 10.1088/1748-0221/15/01/P01019. URL: https://dx.doi.org/10.1088/1748-0221/15/01/P01019.

[102] Richard A. Levine and George Casella. "Implementations of the Monte Carlo EM Algorithm". In: *Journal of Computational and Graphical Statistics* 10.3 (2001), pp. 422–439. ISSN: 10618600. URL: http://www.jstor.org/stable/1391097 (visited on 12/04/2022).

[103] Murray Aitkin and Irit Aitkin. "A hybrid EM/Gauss-Newton algorithm for maximum likelihood in mixture distributions". In: *Statistics and Computing* 6.2 (June 1996), pp. 127–130. ISSN: 1573-1375. DOI: 10.1007/BF00162523. URL: https://doi.org/10.1007/BF00162523.

[104] Eugene Veklerov and Jorge Llacer. "Stopping Rule for the MLE Algorithm Based on Statistical Hypothesis Testing". In: *IEEE Transactions on Medical Imaging* 6.4 (1987), pp. 313–319. DOI: 10.1109/TMI.1987.4307849.

[105] F. Ben Bouallègue, J. F. Crouzet, and D. Mariano-Goulart. "A heuristic statistical stopping rule for iterative reconstruction in emission tomography". In: *Annals of Nuclear Medicine* 27.1 (Jan. 2013), pp. 84–95. ISSN: 1864-6433. DOI: 10.1007/s12149-012-0657-5. URL: https://doi.org/10.1007/s12149-012-0657-5.

[106] S. Agostinelli et al. "Geant4—a simulation toolkit". In: *Nuclear Instruments and Methods in Physics Research Section A: Accelerators, Spectrometers, Detectors and Associated Equipment* 506.3 (2003), pp. 250–303. ISSN: 0168-9002. DOI: https://doi.org/10.1016/S0168-9002(03)01368-8. URL: https://www.sciencedirect.com/science/article/pii/S0168900203013688.

[107] Rene Brun and Fons Rademakers. "ROOT — An object oriented data analysis framework". In: *Nuclear Instruments and Methods in Physics Research Section A: Accelerators, Spectrometers, Detectors and Associated Equipment* 389.1 (1997). New Computing Techniques in Physics Research V, pp. 81–86. ISSN: 0168-9002. DOI: https://doi.org/10.1016/S0168-9002(97)00048-X. URL: https://www.sciencedirect.com/science/article/pii/S016890029700048X.

[108] Brettviren. *Brettviren/gegede: General geometry description*. URL: https://github.com/brettviren/gegede.

[109] C. Andreopoulos et al. "The GENIE neutrino Monte Carlo generator". In: *Nuclear Instruments and Methods in Physics Research Section A: Accelerators, Spectrometers, Detectors and Associated Equipment* 614.1 (Feb. 2010), pp. 87–104. DOI: 10.1016/j.nima.2009.12.009. URL: https://doi.org/10.1016%5C%2Fj.nima.2009.12.009.

[110] Clark D. McGrew. *edep-sim*. https://github.com/ClarkMcGrew/edep-sim, Last accessed on 2023-01-27.

[111] R. Kugathasan. "Integrated front-end electronics for single photon time-stamping in cryogenic dark matter detectors". In: *Journal of Instrumentation* 15.05 (May 2020), p. C05019. DOI: 10.1088/1748-0221/15/05/C05019. URL: https://dx.doi.org/10.1088/1748-0221/15/05/C05019.

[112] R.C. Gonzalez and R.E. Woods. *Digital Image Processing*. Prentice Hall, 2008. ISBN: 9780131687288. URL: https://books.google.it/books?id=8uGOnjRGEzoC.

[113] Andrzej Maćkiewicz and Waldemar Ratajczak. "Principal components analysis (PCA)". In: *Computers Geosciences* 19.3 (1993), pp. 303–342. ISSN: 0098-3004. DOI: https://doi.org/10.1016/0098-3004(93)90090-R. URL: https://www.sciencedirect.com/science/article/pii/009830049390090R.

[114] J. J. Back et al. "Implementation of a local principal curves algorithm for neutrino interaction reconstruction in a liquid argon volume". In: *The European Physical Journal C* 74.3 (Mar. 2014), p. 2832. ISSN: 1434-6052. DOI: 10.1140/epjc/s10052-014-2832-4. URL: https://doi.org/10.1140/epjc/s10052-014-2832-4.